Design, Modeling and Control of Bidirectional Resonant Converter for Vehicle-to-Grid (V2G) Applications

Zaka Ullah Zahid

Dissertation submitted to the Faculty of the

Virginia Polytechnic Institute and State University

in partial fulfillment of the requirements for the degree of

Doctor of Philosophy

In

Electrical Engineering

Jih-Sheng (Jason) Lai, Chairman

Mantu Hudait

Kathleen Meehan

Douglas J. Nelson

William Baumann

September 18, 2015

Blacksburg, VA

Keywords: Battery charger, DC-DC converter, Resonant converter, Bidirectional power flow, Design methodology, Modeling, Controller design

Design, Modeling and Control of Bidirectional Resonant Converter for Vehicle-to-Grid (V2G) Applications

Zaka Ullah Zahid

ABSTRACT

Electric vehicles (EVs) and plug-in hybrid electric vehicles (PHEVs) are gaining popularity because they are more environmentally friendly, less noisy and more efficient. These vehicles have batteries can be charged by on-board battery chargers that can be conductive or inductive. In conductive chargers, the charger is physically connected to the grid by a connector. With the inductive chargers, energy can be transferred wirelessly over a large air-gap through inductive coupling, eliminating the physical connection between the charger and the grid. A typical on-board battery charger consists of a boost power factor correction (PFC) converter followed by a dc-dc converter. This dissertation focuses on the design, modeling and control of a bidirectional dc-dc converter for conductive battery charging application.

In this dissertation, a detailed design procedure is presented for a bidirectional *CLLLC*-type resonant converter for a battery charging application. This converter is similar to an *LLC*-type resonant converter with an extra inductor and capacitor in the secondary side. Soft-switching can be ensured in all switches without additional snubber or clamp circuitry. Because of soft-switching in all switches, very high-frequency operation is possible, thus the size of the magnetics and the filter capacitors can be made small. To further reduce the size and cost of the converter, a *CLLC*-type resonant network with fewer magnetics is derived from the original *CLLLC*-type resonant network. First, an equivalent model for the bidirectional converter is

derived for the steady-state analysis. Then, the design methodology is presented for the *CLLLC*-type resonant converter. Design of this converter includes determining the transformer turns ratio, design of the magnetizing inductance based on ZVS condition, design of the resonant inductances and capacitances. Then, the *CLLC*-type resonant network is derived from the *CLLLC*-type resonant network. To validate the proposed design procedure, a 3.5 kW converter was designed following the guidelines in the proposed methodology. A prototype was built and tested in the lab. Experimental results verified the design procedure presented.

The dynamics analysis of any converter is necessary to design the control loop. The bandwidth, phase margin and gain margin of the control loops should be properly designed to guarantee a robust system. The dynamic analysis of the resonant converters have not been extensively studied, with the previous work mainly concentrated on the steady-state models. In this dissertation, the continuous-time large-signal model, the steady-state operating point, and the small-signal model are derived in an analytical closed-form. This model includes both the frequency and the phase-shift control. Simulation and experimental verification of the derived models are presented to validate the presented analysis.

A detailed controller design methodology is proposed in this dissertation for the bidirectional *CLLLC*-type resonant converter for battery charging application. The dynamic characteristics of this converter change significantly as the battery charges or discharges. And, at some operating points, there is a high-Q resonant peaking in the open-loop bode-plot for any transfer functions in this converter. So, if the controller is not properly designed, the closed-loop system might become unstable at some operating points. In this paper, a controller design methodology is proposed that will guarantee a stable operation during the entire operating frequency range in both battery charging mode (BCM) and regeneration mode (RM). To validate the proposed

controller design methodology, the output current and voltage loop controllers are designed for a 3.5 kW converter. The step response showed a stable system with good transient performance thus validating the proposed controller design methodology.

To my parents

To my brothers and sisters

To my wife

To my daughter

This dissertation is dedicated to the memory of my elder brother.

Acknowledgments

I would like to express my sincere thanks and deep gratitude to my advisor Dr. Jih-Sheng Lai for being my advisor and mentor. Throughout the years at Future Energy Electronics Center (FEEC), Dr. Lai has been my source of knowledge and the true guide through the very versatile engineering problems we faced. His passion and esteem of work have been, and always will be, inspiring me. Under Dr. Lai's supervision, I learned the true qualities of the engineer. His wise advices will always be a guide through my professional career.

I would like to thank my committee members: Dr. Mantu Hudait, Dr. Kathleen Meehan, Dr. Douglas Nelson and Dr. William Baumann for their support, recommendations and guidance.

I would like to extend my thanks to the FEEC family for being amazing colleagues, great supporters, and for being tremendously helpful and willing to cooperate. I will always remember the wonderful times I spent with them in the FEEC, one of the best memories in my life. Special thanks to my friend and colleague, Dr. Zakariya Dalala for all the help and support throughout the past years. I wouldn't be able to complete this work without his help.

Being here, at this moment, I can find no words to express my deepest gratitude to my parents. They have been the candles that lit my way throughout my life, inspired me with passion and courage and always been endless source of love. They put their dream on me, and here I'm, making it true for them. Blessed, I'm.

Finally, I can't be here without thanking my sincere and passionate wife for her continuous support, help and everlasting love. The one who handed me during my downs, and pushed me forward during my ups. Every bit of success I had during my Ph.D. study wouldn't be

colorful without her being next to me. Her encouragement, confidence and patience are true treasure of mine.

I will not forget my little and amazing daughter. You added the joy to my life and just looking to you, the hardships become enjoyable journey.

Table of Contents

List of Figures

List of Tables

Chapter 1 Introduction

1.1 Overview

The interest in electric vehicles has increased rapidly over the past few years. International energy outlook report 2012 reported that more than 100,000 hybrid and all electric vehicles sold globally, and sales figures are approximately doubling each year [1]. And, according to the international energy outlook report 2015 [2], the alternative vehicle technologies are replacing the conventional vehicles. These alternative vehicle technologies, that include hybrid electric vehicles (HEVs), Plug-in HEVs (PHEVs), and Electric Vehicles (EVs), have gained popularity because of their advantages, such as more environmentally friendly, less noisy and more efficient [3]. Many automobile manufacturers like Nissan [4], Tesla [5], Chevrolet [6], BMW [7], VW [8], Volvo [8] and Mercedes [9] have at this point developed and commercialized their first modern electric models, proving that the electric drive is technically viable, environmentally friendly and affordable. The system architecture of HEV/EV is shown in Fig.1.1 [10].

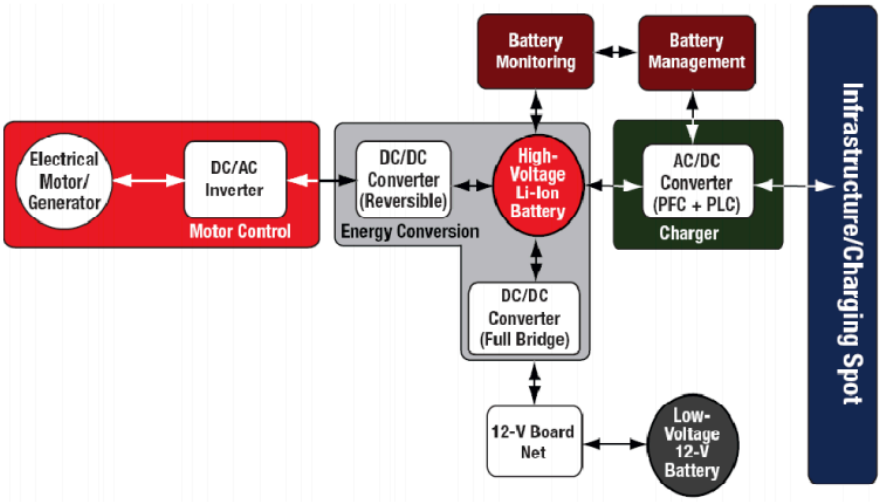

Fig. 1.1. System architecture of HEV and EV

These vehicles have battery packs that can be charged by the battery chargers. These battery chargers convert the ac power from the grid to the dc power, and charge the batteries inside these vehicles. Battery chargers can be unidirectional capable of transferring power from the grid to the battery only. In vehicle-to-grid (V2G) applications, these battery chargers are bidirectional, capable of transferring power back to the grid. Vehicles with V2G capability can serve as a distributed energy resource providing power to the utility loads regulates the voltage and frequency and help the utility load leveling [11]. These vehicles can absorb excessive energy produced by the renewable energy sources like wind and photovoltaic [12, 13].

1.2 Battery Charging Profile and Charger Classification:

There are many types of batteries such as Lead-Acid, Nickel and Cadmium, Lithium ion/polymer, Sodium and Nickel Chloride, Nickel and Zinc. Each battery has its own charging profile. Fig.1.2 shows the typical charging profile of Li-ion battery cell [14]. The constant current mode is followed by the constant voltage mode. During constant current charging, the current is regulated at a constant value until the battery cell voltage reaches a certain reference

voltage. Then, the charging is switched to constant voltage charging, and the battery is charged with a trickle current applied by a constant voltage output of the charger.

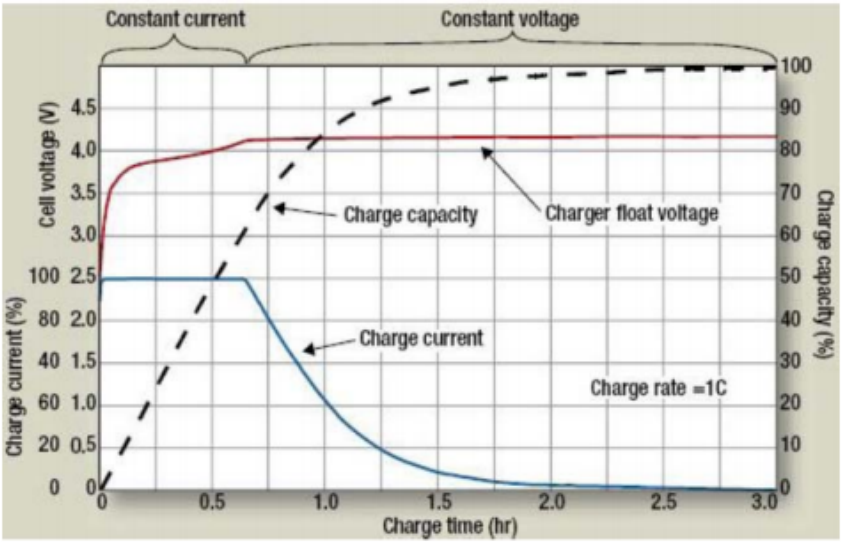

Fig. 1.2. Typical charging profile of Li-Ion cell

Since the inception of the first EVs, there have been many different charging systems proposed. Due to many different configurations of the chargers, they can be classified into different types based on some common design and application features. Table1.1 [15] lists six different methods of classifying chargers.

Table 1.1 Battery charger classification

Classification Type	**Options**
Topology	Dedicated, Integrated
Location	On-board, Off-board
Connection type	Conductive, Inductive, Mechanical
Electrical waveform	AC, DC

Direction of power flow	Unidirectional, Bidirectional
Power level	Level 1, Level 2, Level 3

1.2.1 Types of Battery Charger based on Topology

Battery chargers can be classified based on the circuit topologies [16]. A charger can be a dedicated circuit solely operates to charge the battery. Or, it can be a traction inverter drive that can act as an inverter when the vehicle is moving, and can serve as the charger when the vehicle is not moving. This option is commonly known as integral/integrated chargers. Fig. 1.3 shows the dedicated battery charger, and Fig. 1.4 shows the integrated battery charger.

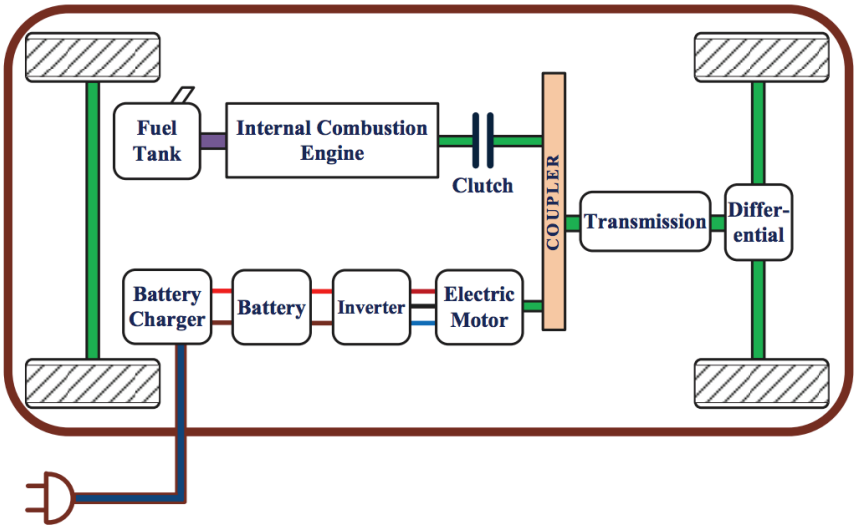

Fig. 1.3. Block diagram of the PHEV with a dedicated battery charger and an inverer.

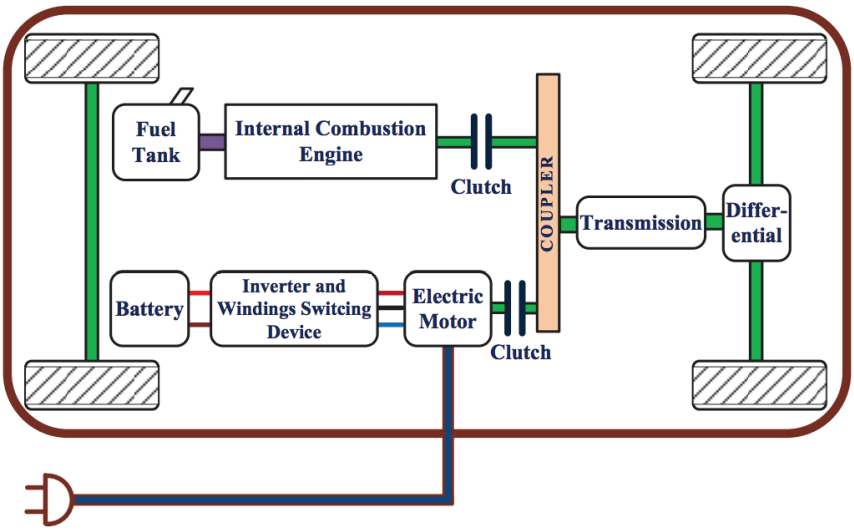

Fig. 1.4. Block diagram of the PHEV with an integrated battery charger and an inverter.

1.2.2 Types of Battery Charger based on Location of Charger

A second classification is based on the location of the charger. A vehicle can carrying the charger on-board, thus the charger is always available for the charging purposes. A vehicle with an on-board battery charger can be charged anywhere from grid. The on-board battery charger consists of a power factor correction circuit followed by a dc-dc converter. With off-board chargers, the vehicles do not carry the charger. These chargers can very high-power chargers capable of charging the vehicle batteries much faster. However, such vehicles cannot be charged everywhere. They can be charged only at the off-board vehicle charging locations. Tesla Motors has both on-board (with AC input voltage) and off-board (with DC input voltage) charging capability. Fig. 1.5 shows three different types of battery chargers in Tesla motors.

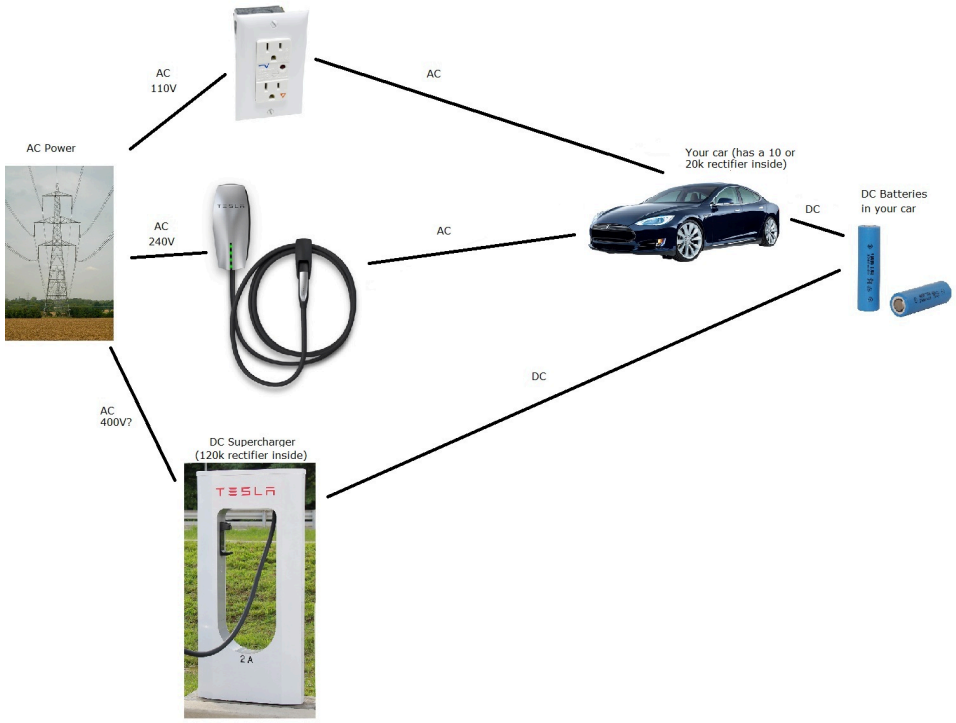

Fig. 1.5. Battery chargers in Tesla Motors Model S [5].

1.2.3 Types of Battery Charger based on Connection Type

The third classification is based on the connection method [8]. Based on connection methods, the battery chargers can be conductive, inductive or mechanical. In conductive battery chargers, the charger is physically connected to the grid by a connector, which may be inconvenient and can present a safety hazard [9, 10]. Fig. 1.6 shows a J1772 connector connected to a Nissan Leaf.

With the contactless chargers, also known as inductive charger, the energy can be transferred wirelessly over a large air-gap through inductive coupling, eliminating the problems associated with contact-based chargers. Inductive chargers are safer and convenient, and are being utilized in applications like automobiles [6-8], aerospace [11], robotics [12], under-water applications [13] and medical implants [14]. Fig. 1.7 shows a Nissan Leaf with Evatran's Plugless wireless charger.

Fig. 1.6. Nissan Leaf charged by a conductive battery charger [4].

Fig. 1.7. Nissan Leaf EV charged by a wireless battery charger [4].

In the mechanical charging, the depleted battery packs are replaced with a full one in battery swap stations. Only Tesla Motors Model S is designed to allow a fast battery swap, exchanging your battery for a fully charged battery in less than half the time it takes to refill a gas tank. Fig 1.8 shows how a fully charged battery at a Tesla Station replaces a depleted battery.

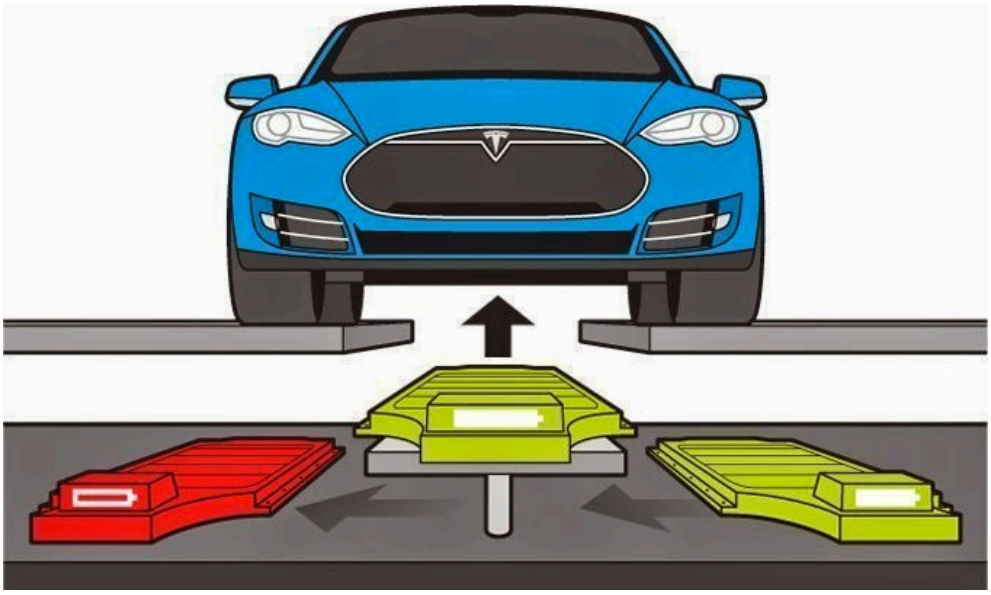

Fig. 1.8. Replacing a depleted battery with a fully charged battery in Tesla Model S EV [5].

1.2.4 Types of Battery Charger based on Electrical Waveforms

The fourth classification is based on the electrical waveform at the connection port. This waveform can be either a dc or an ac[15]. Previously, the PHEVs and EVs in the market used to employ an ac connection type. However, in the now there are dc sources also available. Fig. 1.5 shows the battery chargers with both ac and dc inputs in Tesla's Model S EV.

1.2.5 Types of Battery Charger based on Direction of Power Flow

Fifth, the battery charger can be unidirectional or bidirectional. Unidirectional battery chargers can transfer energy from the grid to the battery only. While, the bidirectional battery chargers can transfer energy between the grid and the batteries in either direction.

1.2.6 Types of Battery Charger based on Power Level

The last classification is based on the charging level of the battery charger. There are three charging levels have been defined for EVs and PHEVs [17]. Table 1.2 shows the voltage and current at different levels. Level 1 and level 2 charging are assumed to be the normal charging levels which will take place where the vehicle will sit for a substantial amount of time such as

the home or office [18]. However, the drawback of charging a vehicle with these normal charging levels is that it can take 4 to 20 hours depending on available power, battery size and SOC of the battery [4] and this is not a viable option when long travel distances are considered. The solution to this lengthy charging time issue is the level 3 fast charging. Level 3 charging makes battery-powered vehicles more competitive against conventional ICE vehicles by charging the battery in less than 30 minutes [19]. Typically, Level 3 charging is accomplished via an off-board charger by means of converting three phase 480-V AC to a regulated DC.

Table 1.2 Battery charging levels

	AC Voltage (V)	Max. Current (A)	Max. Power (kW)
Level 1	120	16	1.92
Level 2	240	80	19.2
Level 3	300-600	400	240

1.3 Charger System

The charging time and lifetime of the battery have a strong dependency on the characteristics of the battery charger [20-22]. Several manufacturers are working worldwide on the development of various types of battery modules for electric and hybrid vehicles. However, the performance of battery modules depends not only on the design of modules, but also on how the modules are used and charged. In this sense, battery chargers play a critical role in the evolution of this technology.

The conventional battery charger system is shown in Fig. 1.9 [23]. Because batteries have a finite energy capacity, connecting to the power grid must recharge PHEVs and BEVs on a periodic basis, typically. The charging system for these vehicles consists of an AC/DC rectifier to generate a DC voltage from the AC line, followed by a DC/DC converter to generate the DC voltage required by the battery pack. The battery pack must also be carefully monitored during

operation and charging in order to maximize energy usage and prolong battery life. The focus of this dissertation is to design and implement the bidirectional DC-DC converter that charges the high-voltage battery. The DC bus voltage is usually fixed, and the battery voltage is range of voltages.

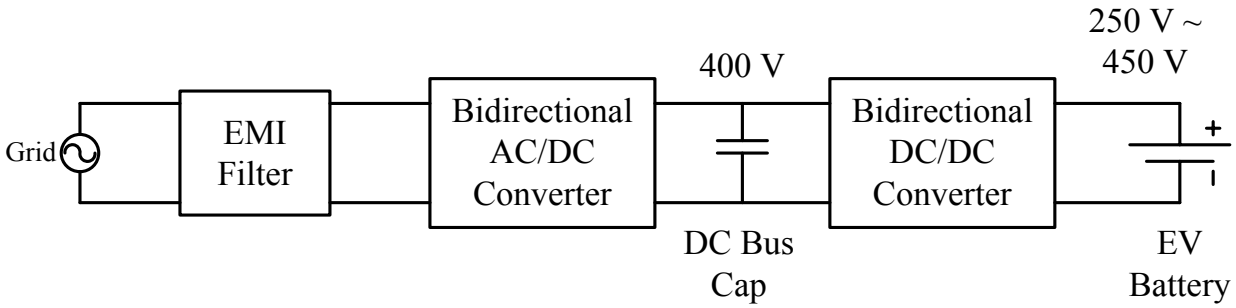

Fig. 1.9. Block diagram of bidirectional battery charger.

1.4 Charger System Requirements and Objectives of this Research

In EV applications, the propulsion battery is required to undergo a continuous sequence of deep discharges followed by recharge to maximum capacity. The prime requirement is therefore a system that provides a rapid and efficient charge, using as simple equipment as possible and avoiding damage to the battery. The entire charging process should be arranged in two phases. The first charging phase is at constant current and with the battery voltage progressively rises. As soon as the battery voltage reaches the trickle level, the constant-voltage charging method should be applied, with the charging current progressively falling down to the maintenance level.

There are significant challenges associated with the design of the EV battery chargers, such as high power density, high efficiency, low cost, isolation and voltage adaption while complying with harsh environment automotive. Increasing the switching frequency can decrease the cost and size of passive elements. However, the switching losses (turn-on and turn-off losses) increase with the increase in switching frequency resulting in higher losses and lower power-

stage efficiency. Therefore, soft switching methods and resonant circuits are widely used to increase the switching frequency [24] because these converters have much lower switching losses. Operating from a high input voltage requires a soft transition topology to minimize the switching losses, and reduce the high frequency EMI caused by a high dv/dt. Another challenge of such design is associated with the reverse recovery losses and the noise caused by the high di/dt and dv/dt in the output rectifiers. And also it is necessary to choose a topology that is also capable of controlling high output current.

In addition, galvanic isolation is required to disconnect grid from vehicle electrically. Galvanic isolation can be achieved by means of using a high frequency (HF) transformer integrated into DC-DC converter.

1.5 Conventional Isolated DC-DC Converters

Vehicles with V2G capability require a bidirectional battery charger that consists of a bidirectional ac-dc converter followed by a bidirectional dc-dc converter. The dc-dc converters manage the power flow between the dc bus and the battery. A number of bidirectional dc-dc converters can be found in the literature [13, 25-34]. The main focus in these converters is on achieving soft-switching in the power switches for a wide range of load variation to get rid of the EMI, and to enable very high-frequency operation so that the size, and thus the cost, of the magnetics and the output filter is minimized. Both non-isolated [25-27] and isolated [28-34] converters are proposed. The advantages with the non-isolated converters are fewer numbers of components and high power-stage efficiency. However, in some applications, including EV battery chargers, galvanic isolation is required for safety between the primary-side and the secondary side [30].

1.5.1 PWM Converters for Wide Output Load Variation

In the PWM converters, the phase-shifted full-bridge (PSFB) converter is the most widely used topology for a wide input and a wide output voltage range conditions [35, 36]. This converter can operate at a constant switching frequency for a very wide output load variation. However, this topology suffers from a number of issues for a wide range of load variation. These issues are;

1) The ZVS range in the primary-side switches depends on the primary-side transformer leakage inductance. To achieve ZVS for all load and line conditions, large leakage inductance is required [37, 38]. This, however, results in duty cycle loss and it increases the reactive energy in the circuit for certain load conditions that decreases converter efficiency [39].
2) Because of the energy stored in the transformer secondary-side leakage inductance, there is severe parasitic ringing in the secondary side switches. To damp or clamp this ringing, RCD snubbers, lossless snubbers or active clamp circuits are used [40]. These extra circuitries allow the reduction of the voltage spikes across the secondary switches. However, they increase the size, cost and circuit complexity. Even with these snubber or clamp circuits, the voltage stress on the secondary side switches is higher than the output voltage, making this topology unsuitable for high output voltage applications [40].

1.5.2 Resonant Converters for Wide Output Load Variation

Resonant converters are becoming a desirable topology for high-power dc-dc applications [41-49]. In some applications; the resonant converters are the natural choice as the reactive effects are noticeable and unavoidable [41-45] while in other applications [46-49], these converters are used because they offer a number of advantages over the non-resonant type

topologies, including soft-switching in all switches, very high-frequency operation, low EMI, simple control, high efficiency and fewer component counts. It eliminates the need of clamp or snubber circuitry.

One of the most popular resonant topology for a wide input and wide output voltage range is the *LLC* converter [31, 50]. Because of soft-switching in all switches, this converter can operate at a very high switching frequency. Transformer leakage inductance is part of the power stage. With the operating switching frequency control, this converter has very high power-stage efficiency for a very wide range of output load. However, this topology is suitable for a unidirectional power transfer. In the regeneration mode, the magnetizing inductance is in parallel with the bridge voltage, and it is no longer part of resonant network, converting the topology into a series resonant converter (SRC). The efficiency of SRC drops considerably as the operating switching frequency drifts away from the series resonant frequency, making it unsuitable for a very wide input and output voltage range applications.

1.6 Topology Selection for EV Battery Charger

A symmetric unity gain bidirectional *LLC* converter was proposed in [49]. This topology has all the advantages of that *LLC* converter, and is capable of transferring power in either direction. However, the converter in [49] was designed for a unity gain condition only, for which the resonant network components are symmetrical on both sides. At unity gain, the converter operates at the primary-side series resonant frequency, and the voltage gain curves are always monotonically decreasing. In the battery charging applications, the battery voltage varies significantly during the whole charging process, and the bidirectional converter experiences a very wide input and a very wide output voltage range. And, since the voltage gain of the converter is not unity at all operating points, the resonant network is no longer symmetrical. And,

multiple peaks can appear in the voltage gain curves under certain load and line conditions. Hence for a battery charging applications, the design methodology proposed in [49] is not enough. A new design methodology is needed that takes in to account the wide input and wide output voltage range, and which can ensure that the voltage gain curves are always monotonically decreasing for all load and line conditions.

This thesis works on the power-stage, presenting a *CLLLC*-type resonant converter for battery charging applications, which guarantees ZVS under any load conditions, and then gets it further improved by proposing a *CLLC*-type resonant converter with one less inductor. This resonant converter can achieve ZVS operation in the entire load range by using the magnetizing inductance of the transformer. In addition, the converter can operate with wide input and output voltage variations without penalizing the efficiency. Therefore, the converter is suitable for applications in which high efficiency and high power density are required such as EV battery charger.

1.7 Research Scope and Objectives

The scope of the research is,

- To propose a design methodology for a bidirectional dc-dc resonant converter for wide input and wide output voltage range,
- To derive the large-signal model, the steady-state model and the small-signal model of the converter power-stage,
- And, to propose the controller design methodology that will guarantee a stable closed-loop operation of the converter under all load and line conditions.

And, the objectives of this research are,

- To design a dc-dc converter that is capable of transferring power in both directions
- The converter should have very high power-stage efficiency in both directions of energy flow,
- All the switches in the converter should have soft-switching under all load and line conditions so that very high-frequency operation is possible,
- The converter should be able to operate in both constant current mode and constant voltage mode,
- The converter is able to start softly in both directions of energy flow.

1.8 Thesis Outline

This thesis is divided into five chapters. They are organized as follows. The first chapter is background of the battery charger. Since the DC-DC converter is the key element in the battery charger system, and this thesis mainly deals with the DC-DC converter for an EV battery charger. In the second chapter, the design methodology for the converter power-stage is proposed for both the *CLLLC*-type and *CLLC*-type resonant converters for battery charging applications. The steady-state operation of the converter is explained in detail. A 3.5 kW hardware prototype for the battery charger has been designed, fabricated and tested to verify the proposed design methodology. Experimental results are also presented in this chapter.

The steady-state model, the large-signal model and the small signal model for the resonant converter are presented in the third chapter. Experimental result verified the derived models. In the fourth chapter, a controller design methodology is proposed that will guarantee a stable closed-loop operation at all load and line conditions. In the last chapter, summary of the dissertation and future work is presented.

Chapter 2 Design of Power Stage

2.1 Fundamental Analysis

2.1.1 Converter Power Stage

Fig. 2.1 shows the circuit topology for the resonant converter capable of transferring power in both directions. In the battery charging mode (*BCM*), the power is transferred from the dc bus to the battery, while in the regeneration mode (*RM*), the power is transferred from the battery to the dc bus. This converter has a symmetric structure in both directions. This converter is similar to an *LLC* resonant converter with extra inductor and capacitor in the secondary side. Switches in the primary-side form a high-frequency full-bridge inverter converting the input dc voltage into a quasi-square wave ac while the switches in the secondary-side serve as a rectifier converting the high-frequency ac into a dc output voltage. The resonant network consisting of resonant inductances (L_1 and L_2), transformer magnetizing inductance (L_m) and the two resonant capacitors (C_1 and C_2) separates the inverting and rectifying switches. The transformer provides the galvanic isolation between the primary-side and the secondary side. The magnetizing

inductance and the leakage inductances of the transformer are part of the power stage. The resonant capacitors are not only part of the resonant network but they also block any dc voltage offset in the generated quasi-square voltage generated by the inverting bridge.

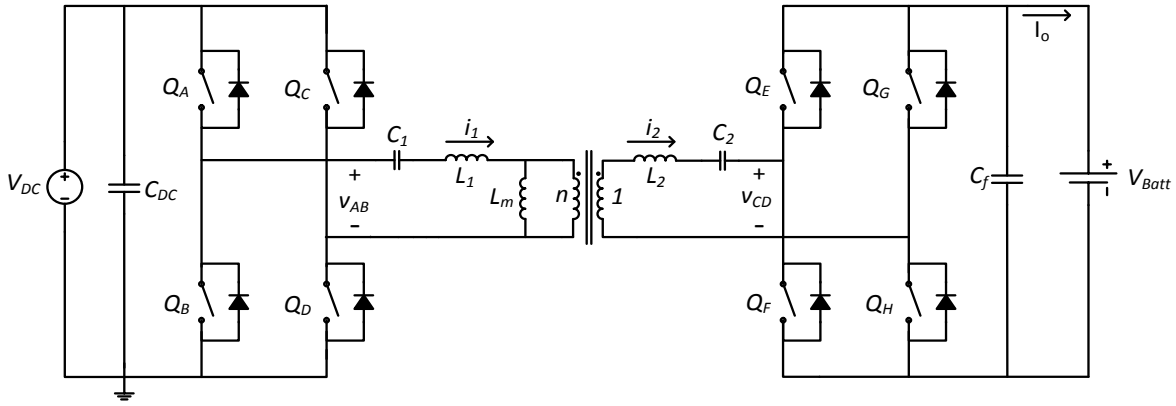

Fig. 2.1. Circuit topology for the bidirectional resonant converter.

2.1.2 The Steady-State Model

Without a thorough theoretical analysis of the resonant converter, it is quite difficult to achieve good designs of the converter. The steady-state model for the converter operating in the *BCM* is derived here. The model for the converter operating in the *RM* can be derived in a similar fashion. The equivalent model of the resonant converter operating in the *BCM* is shown in Fig. 2.2.

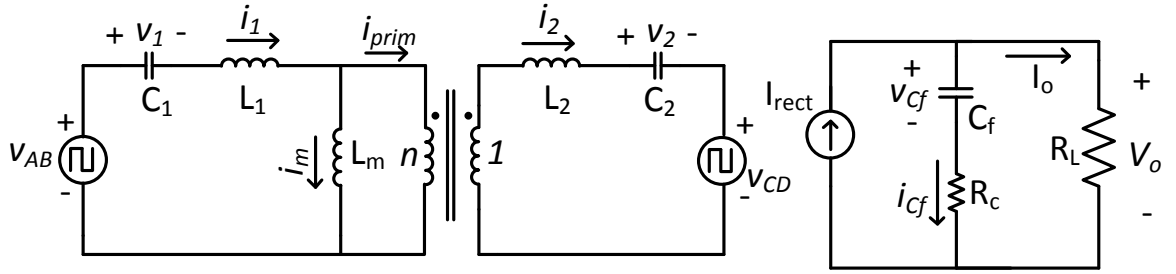

Fig. 2.2. Equivalent circuit diagram for the resonant converter operating in the battery charger mode.

where,

$$v_{AB} = \sum_{n=1}^{\infty} \frac{4\, v_{DC}}{n\, \pi} \cdot \sin(n\, \omega_s t) \tag{2.1}$$

$$v_{CD} = sign(i_2) \cdot\ v_o \tag{2.2}$$

$$i_{rect} = \ |i_2| \tag{2.3}$$

$$I_o = \frac{2}{\pi} \cdot\ \|i_2\| \tag{2.4}$$

The first harmonic approximated (FHA) model can be derived from the equivalent circuit in Fig. 2.2. Since, the resonant network in Fig. 2.2 is tuned to the fundamental frequency. And, the current i_1 is almost sinusoidal. It can be assumed that the voltage, v_{AB}, is sinusoid. And, that the power is transferred by the fundamental component only. The FHA model is shown in Fig. 2.3.

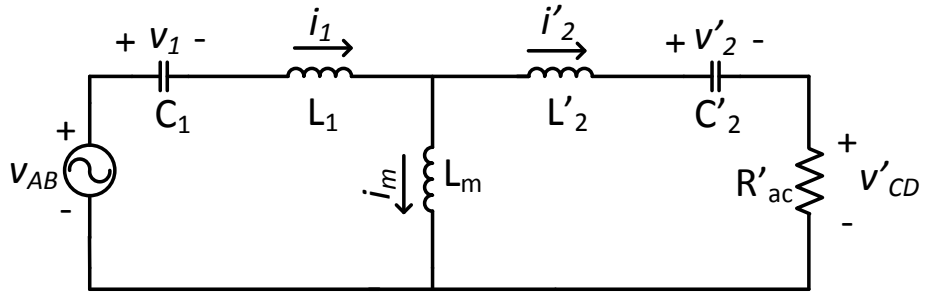

Fig. 2.3. FHA model for the resonant converter operating in the battery charging mode.

Where,

If n is the transformer turns ratio, then,

$$v_{AB} = \frac{4\, v_{DC}}{\pi} \cdot \sin(\omega_s t) \tag{2.5}$$

$$L_2' = \ n^2 \cdot L_2 \tag{2.6}$$

$$C_2' = \frac{1}{n^2} \cdot C_2 \tag{2.7}$$

$$R_{ac}' = \ n^2 \cdot \frac{8}{\pi^2}\, R_L \tag{2.8}$$

The output voltage and output current can be calculated using the following equations,

$$I_o = \frac{2n}{\pi} \cdot \|i'_2\| \tag{2.9}$$

$$V_o = I_o \cdot R_L \tag{2.10}$$

With the phase-shift control, the ZVS range depends on the series leakage inductance. Large leakage inductance is required to ensure ZVS for a very wide range of output load variation. In this topology, the series inductance is part of the resonant network, and thus can be not be made large to ensure ZVS for wide variation of output load. So, in this converter with a phase-shift control, the ZVS cannot be ensured at all load and line conditions. To overcome this problem, variable frequency approach is adapted here. With this approach, ZVS can be maintained at all load and line conditions as long as the primary-side current lags behind the primary-side bridge voltage.

2.1.3 Steady-State Operation of the Converter

The output voltage versus operating switching frequency curves and the output current versus the operating switching frequency curves for the bidirectional converter can be plotted using (2.9) and (2.10). Fig. 2.4 shows the voltage gain curves for the converter under different load conditions with transformer turns ratio equal to 1.

The gain of the converter is unity at primary side series resonant frequency, f_{ser}. The gain of the converter is more than unity for frequencies lower than f_{ser}, and the gain is less than unity for frequencies greater than f_{ser}. These gain curves can be divided into three regions, namely, Region 1, 2 and 3.

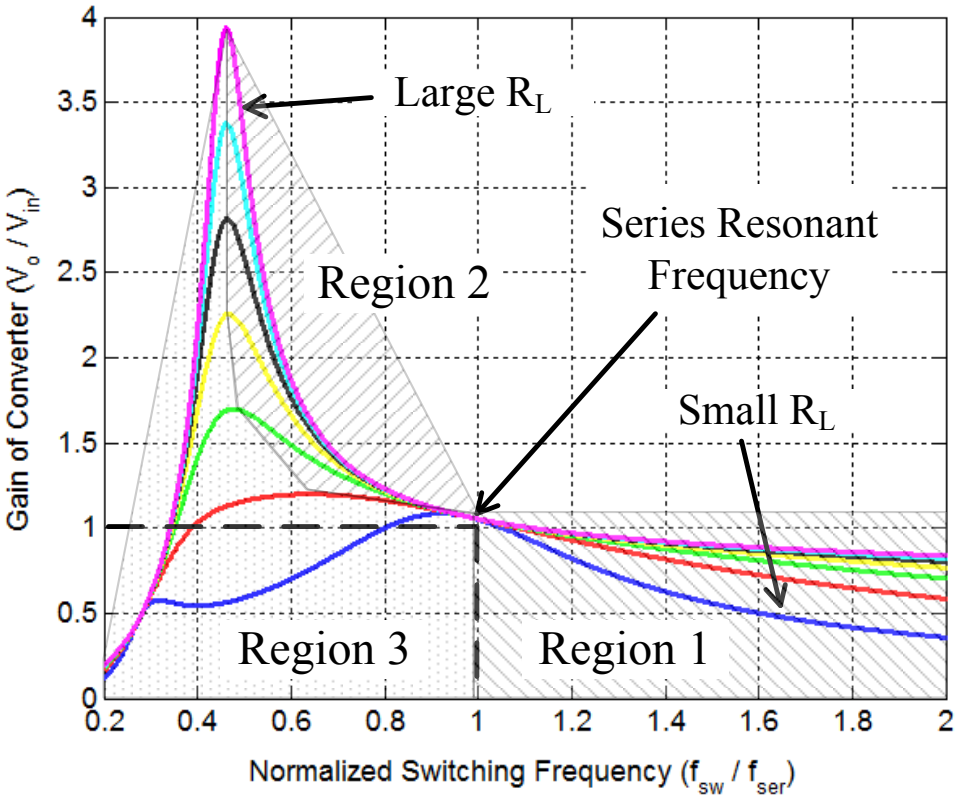

Fig. 2.4. The voltage gain versus operating switching frequency curves under different load conditions.

2.1.3a Operation of Converter in Region 1

This region consists of the frequencies higher than the f_{ser}. In this region, the primary side switches turn on at zero voltage condition whereas the secondary side switches turn on and turn off at zero currents. The gain of the converter in this region is always less than unity under any output load conditions. The voltages and the currents for converter operating in this region are shown in Fig. 2.5. Fig. 2.14 shows the voltages and the currents for converter operating at f_{ser}.

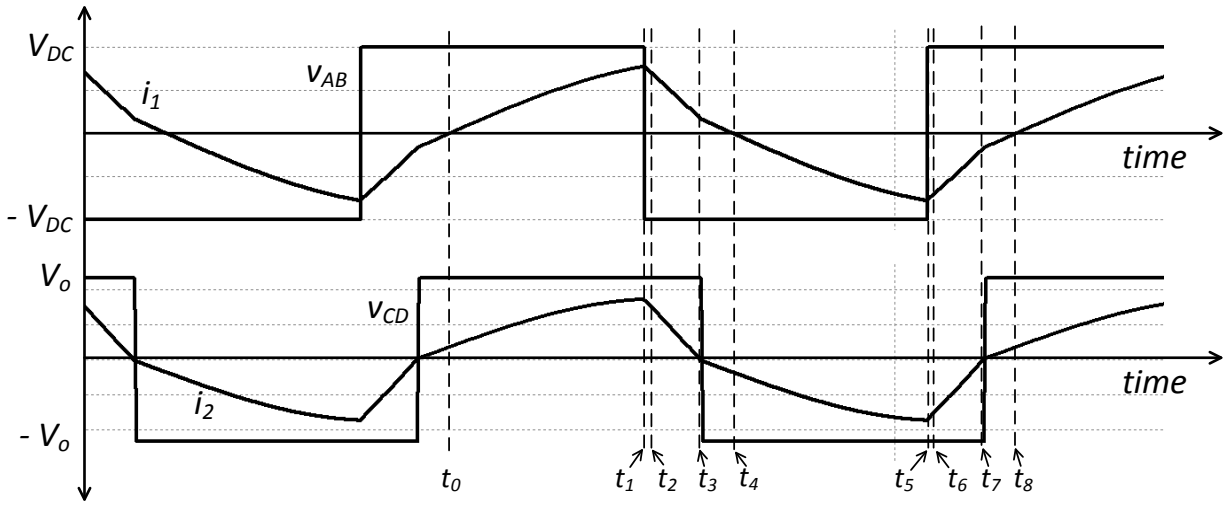

Fig. 2.5. The voltages and the currents for converter operating in Region 1.

Mode 1 *($t_0 \sim t_1$)*:

In this mode, the gating signals for the switches Q_A and Q_D is high. So, these switches are turned on. The bridge voltage, v_{AB}, is equal to the input dc voltage. The voltage across the output capacitors of the switches Q_B and Q_C is equal to the input dc voltage. The current in the secondary side, i_2, is positive and the anti-parallel diodes of the switches Q_E and Q_H conduct. The voltage at the secondary side bridge, v_{CD}, is equal to the output voltage, v_o. The voltage across the output capacitors of the switches Q_F and Q_G is equal to the output voltage, v_o. In this mode, the energy is transferred from the input to the output. Fig. 2.6 shows the operation of the converter in this mode.

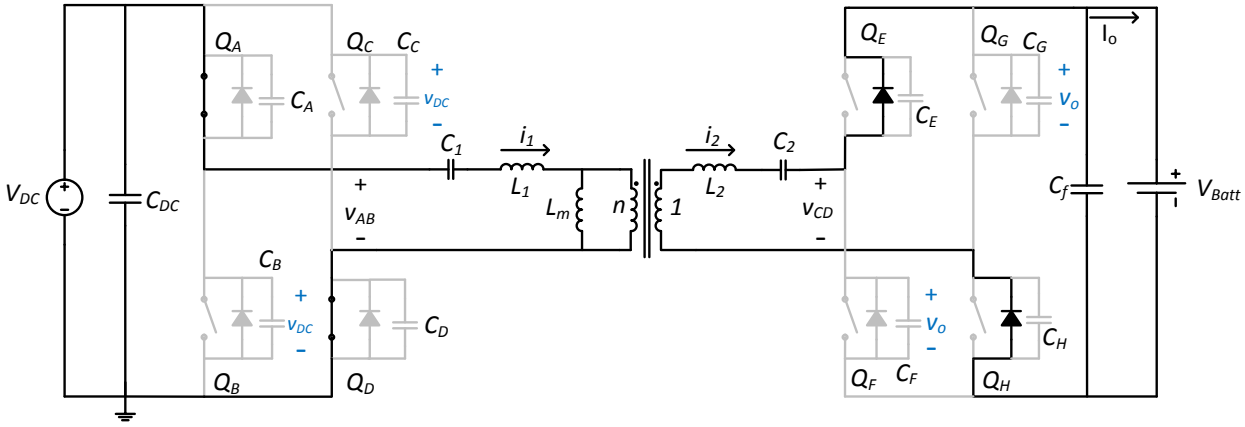

Fig. 2.6. Power-stage operation during Mode 1.

Mode 2 ($t_1 \sim t_2$):

This is the dead-time interval. In this mode, the gating signals for all the switches $Q_A \sim Q_D$ are low. So, these switches are turned off. During this interval, the current i_1 discharges the output capacitors of switches Q_B and Q_C and charges the output capacitors of switches Q_A and Q_D. The bridge voltage, v_{AB}, is equal to the input dc voltage. The current in the secondary side, i_2, is still positive and the anti-parallel diodes of the switches Q_E and Q_H conduct. The voltage at the secondary side bridge, v_{CD}, is equal to output voltage, v_o. The voltage across the output capacitors of switches Q_F and Q_G is equal to the output voltage, v_o. In this mode, no energy is transferred from the input to the output. Fig. 2.7 shows the operation of the converter in this mode.

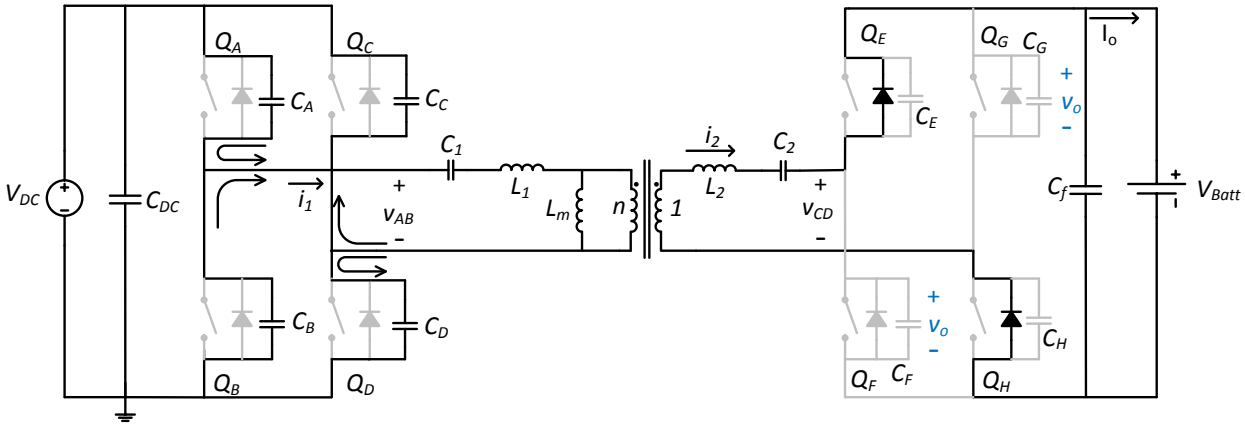

Fig. 2.7. Power-stage operation during Mode 2.

Mode 3 ($t_2 \sim t_3$):

In this mode, the gating signals for the switches Q_B and Q_C is high. So, these switches are turned on. In mode 2, the output capacitors for these switches were completely discharged. So, these switches turned on at zero voltage. The current i_1 is negative, and thus the anti-parallel diodes of these switches conduct. The bridge voltage, v_{AB}, is equal to the negative input dc voltage. The voltage across the output capacitors of the switches Q_A and Q_D is equal to the input

dc voltage. The current in the secondary side, i_2, is still positive and the anti-parallel diodes of the switches Q_E and Q_H conduct. The voltage at the secondary side bridge, v_{CD}, is equal to the output voltage, v_o. The voltage across the output capacitors of the switches Q_F and Q_G is equal to the output voltage, v_o. In this mode, no energy is transferred from the input to the output. Fig. 2.8 shows the operation of the converter in this mode.

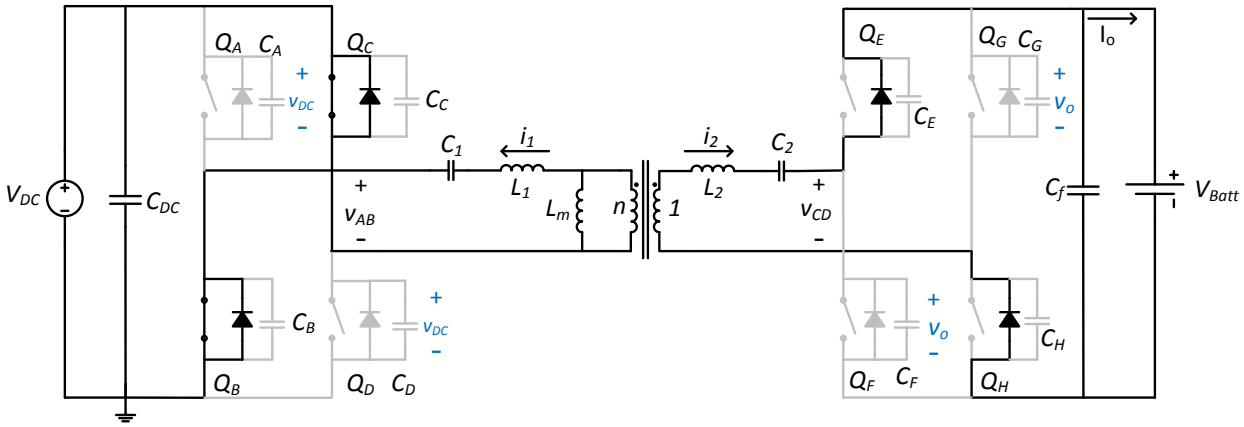

Fig. 2.8. Power-stage operation during Mode 3.

Mode 4 ($t_3 \sim t_4$):

The operation of the converter in this mode is similar to the operation of the converter in mode 3. The slope of current i_2 in mode 3 was negative and the magnitude of the current was decreasing. In this mode, this current becomes negative and the anti-parallel diodes of the switches Q_E and Q_H stop to conduct. The anti-parallel diodes of the switches Q_F and Q_G now conduct. In this mode, the energy is transferred from the input to the output. Fig. 2.9 shows the operation of the converter in this mode.

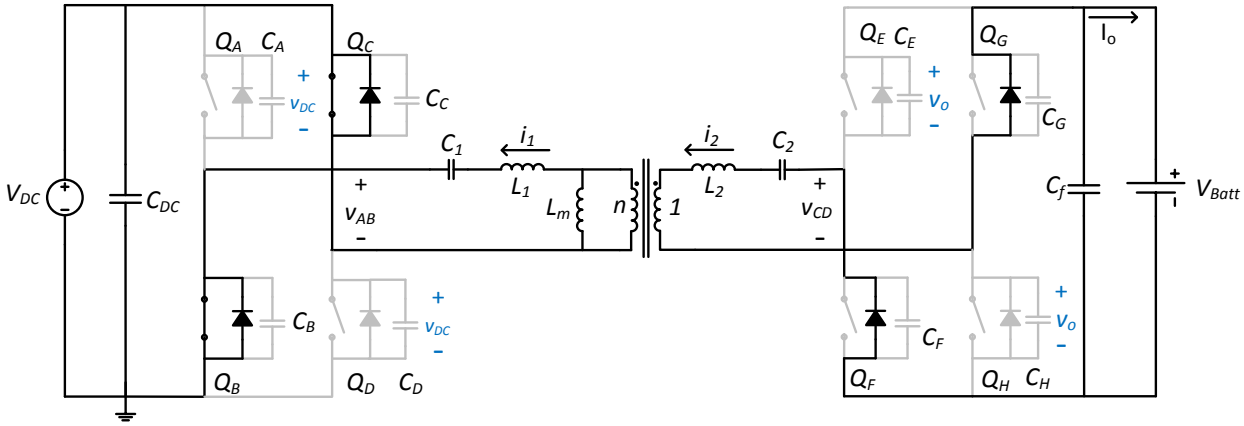

Fig. 2.9. Power-stage operation during Mode 4.

Mode 5 ($t_4 \sim t_5$):

The operation of the converter in this mode is the same as the operation of the converter in mode 1. The only difference is, the directions of the primary side current, i_1 and the secondary side current i_2 are reversed. The gating signals for the switches Q_B and Q_C are high and these switches are turned on. The bridge voltage, v_{AB}, is equal to the negative input dc voltage. The voltage across the output capacitors of the switches Q_A and Q_D is equal to the input dc voltage. The current in the secondary side, i_2, is negative and the anti-parallel diodes of the switches Q_F and Q_G conduct. The voltage at the secondary side bridge, v_{CD}, is equal to the negative output voltage, v_o. The voltage across the output capacitors of the switches Q_E and Q_H is equal to the output voltage, v_o. In this mode, the energy is transferred from the input to the output. Fig. 2.10 shows the operation of the converter in this mode.

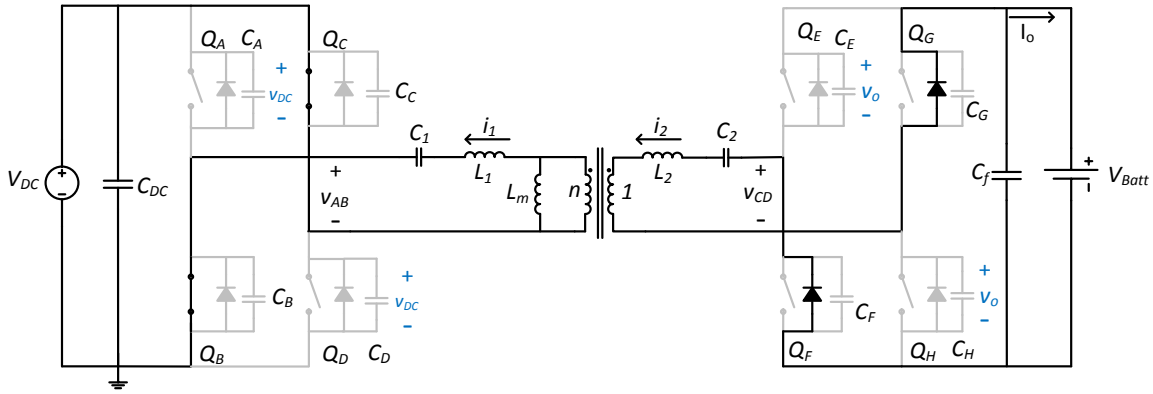

Fig. 2.10. Power-stage operation during Mode 5.

Mode 6 ($t_5 \sim t_6$):

This is the dead-time interval. In this mode, the gating signals for all the switches $Q_A \sim Q_D$ are low. So, these switches are turned off. During this interval, the current i_1 discharges the output capacitors of switches Q_A and Q_D and charges the output capacitors of switches Q_B and Q_C. The bridge voltage, v_{AB}, is equal to the negative input dc voltage. The current in the secondary side, i_2, is still negative and the anti-parallel diodes of the switches Q_F and Q_G conduct. The voltage at the secondary side bridge, v_{CD}, is equal to the negative output voltage, v_o. The voltage across the output capacitors of switches Q_E and Q_H is equal to the output voltage, v_o. In this mode, no energy is transferred from the input to the output. Fig. 2.11 shows the operation of the converter in this mode.

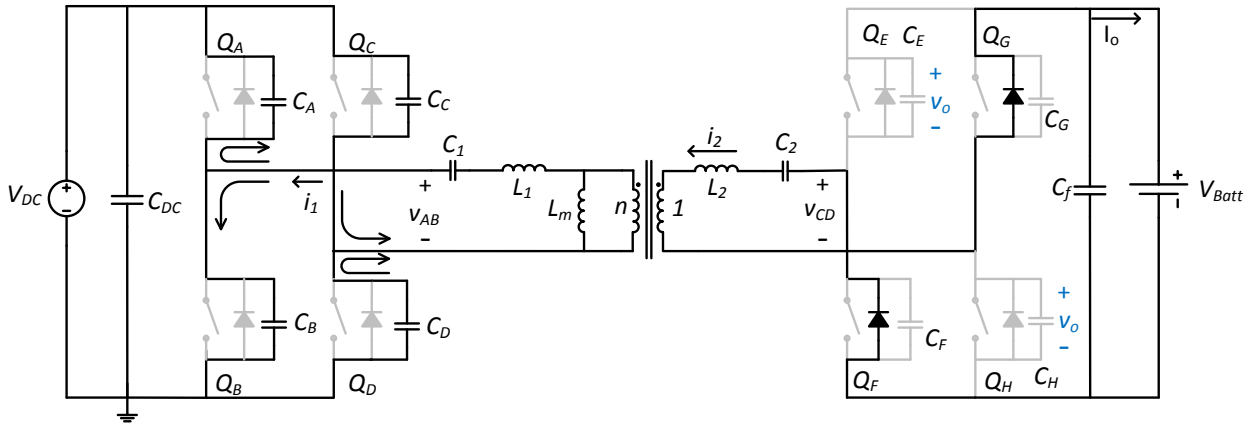

Fig. 2.11. Power-stage operation during Mode 6.

Mode 7 ($t_6 \sim t_7$):

In this mode, the gating signals for the switches Q_A and Q_D is high. So, these switches are turned on. In mode 6, the output capacitors for these switches were completely discharged. So, these switches turned on at zero voltage. The current i_1 is negative, and thus the anti-parallel diodes of these switches conduct. The bridge voltage, v_{AB}, is equal to the input dc voltage. The voltage across the output capacitors of the switches Q_B and Q_C is equal to the input dc voltage. The current in the secondary side, i_2, is still negative and the anti-parallel diodes of the switches

Q_F and Q_G conduct. The voltage at the secondary side bridge, v_{CD}, is equal to the negative output voltage, v_o. The voltage across the output capacitors of the switches Q_E and Q_H is equal to the output voltage, v_o. In this mode, no energy is transferred from the input to the output. Fig. 2.12 shows the operation of the converter in this mode.

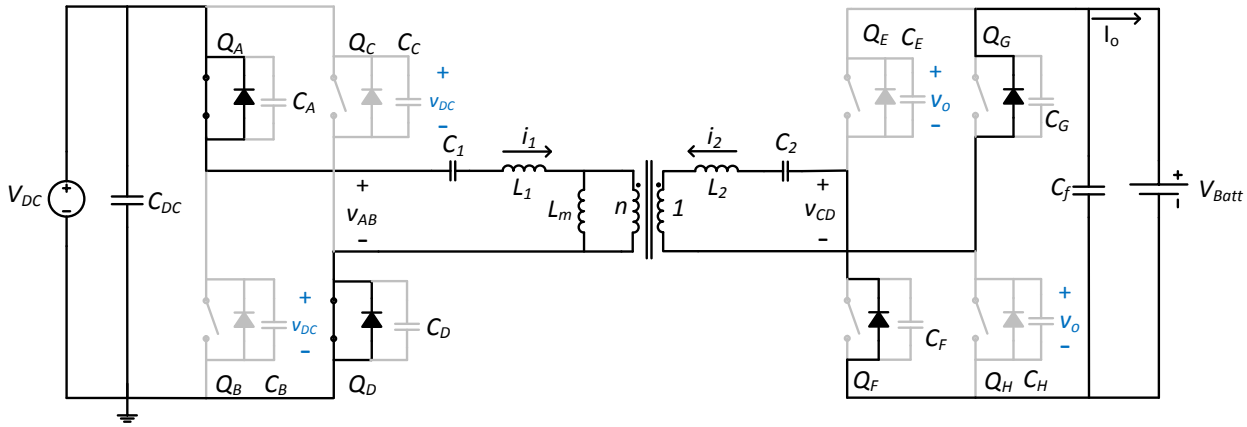

Fig. 2.12. Power-stage operation during Mode 7.

Mode 8 ($t_7 \sim t_8$):

The operation of the converter in this mode is similar to the operation of the converter in mode 7. The slope of current i_2 in mode 3 was positive and the magnitude of the current was decreasing. In this mode, this current becomes positive, and the anti-parallel diodes of the switches Q_F and Q_G stop to conduct. The anti-parallel diodes of the switches Q_E and Q_H now conduct. In this mode, the energy is transferred from the input to the output. Fig. 2.13 shows the operation of the converter in this mode.

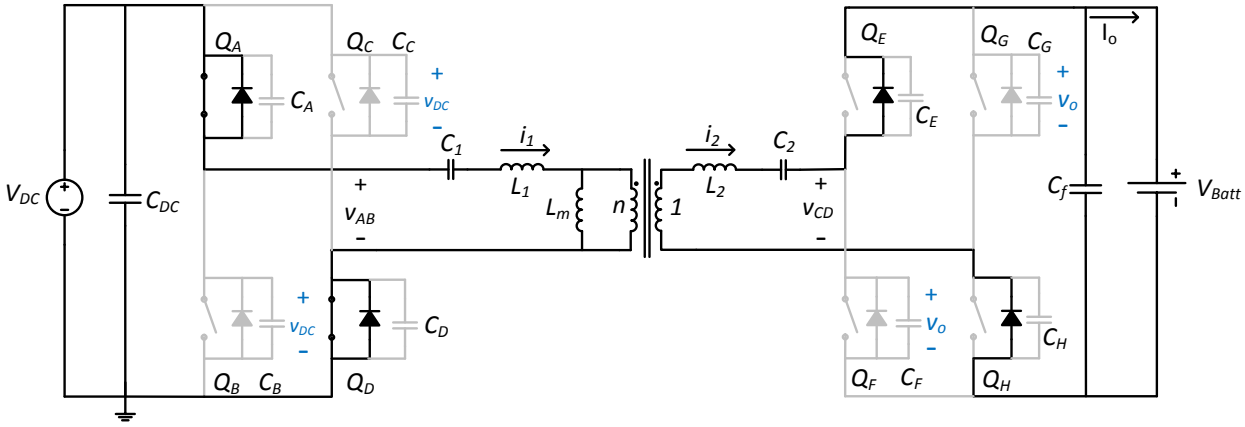

Fig. 2.13. Power-stage operation during Mode 8.

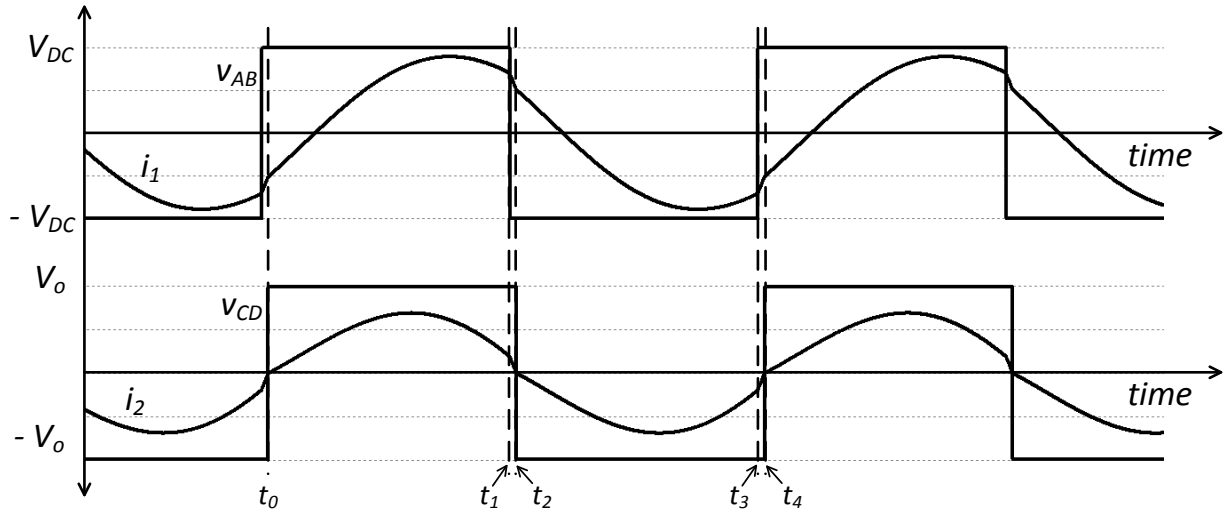

Fig. 2.14. The voltages and the currents for converter operating at primary side series resonant frequency.

2.1.3b Operation of Converter in Region 2

This region consists of gain curves with negative slope, and operating frequencies lower than the f_{ser}. In this region, the primary side switches turn on at zero voltage condition whereas the secondary-side switches turn on and turn off at zero currents. The secondary-side current is in discontinuous conduction mode. The gain of the converter in this region is always equal to or more than unity. The voltages and the currents for converter operating in this region are shown in Fig. 2.6.

The operation of the converter in this region is very similar to the operation of the converter in region 1. There are a couple of modes that are not present when the converter is operating in the Region 1. The converter operates in the discontinuous conduction mode (DCM).

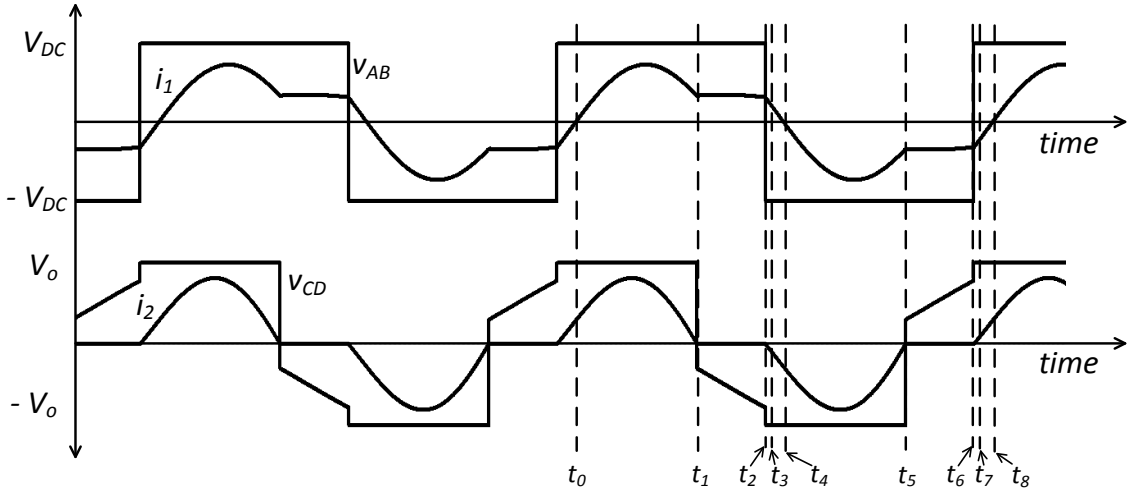

Fig. 2.15. The voltages and the currents for converter operating in Region 2.

Mode 1 ($t_0 \sim t_1$):

The operation of converter in this mode is similar to the operation in Mode 1 in Region 1.

Mode 9 ($t_1 \sim t_2$):

During this mode, the secondary-side operates in the DCM. The secondary-side current is zero. The output capacitance of the rectifying switches Q_F and Q_G discharge, and the output capacitance of switches Q_E and Q_H charge. No energy is transferred from primary-side to secondary-side during this mode. Fig. 2.16 shows the operation of the converter in this mode.

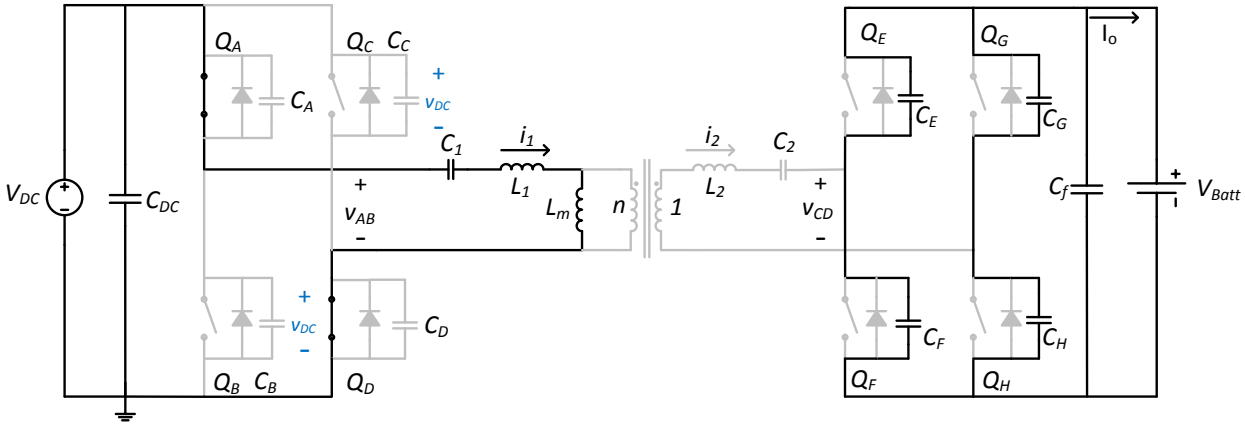

Fig. 2.16. Power-stage operation during Mode 9.

Mode 2 ($t_2 \sim t_3$):

The operation of converter in this mode is similar to the operation in Mode 2 in Region 1. The only difference is, the secondary-side current is equal to zero in this case.

Mode 4 ($t_3 \sim t_4$):

The operation of converter in this mode is similar to the operation in Mode 4 in Region 1.

Mode 5 ($t_4 \sim t_5$):

The operation of converter in this mode is similar to the operation in Mode 5 in Region 1.

Mode 10 ($t_5 \sim t_6$):

During this mode, the secondary-side operates in the DCM. The secondary-side current is zero. The output capacitance of the rectifying switches Q_E and Q_H discharge, and the output capacitance of switches Q_F and Q_G charge. No energy is transferred from primary-side to secondary-side during this mode. Fig. 2.17 shows the operation of the converter in this mode.

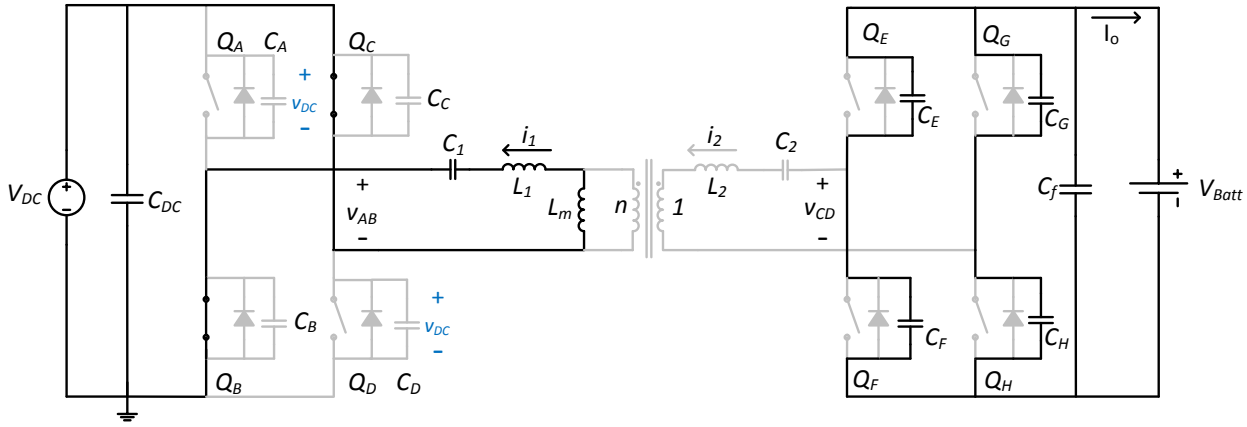

Fig. 2.17. Power-stage operation during Mode 10.

Mode 7 ($t_6 \sim t_7$):

The operation of converter in this mode is similar to the operation in Mode 7 in Region 1. The only difference is, the secondary-side current is zero in this mode.

Mode 8 ($t_7 \sim t_8$):

The operation of converter in this mode is similar to the operation in Mode 8 in Region 1.

2.1.3c Operation of Converter in Region 3

This region consists of operating frequencies lower than the f_{ser}. In this region, the gain of the converter can be more than 1 or less than 1. This is the ZCS region where the primary side switches turn off at zero currents. The converter is not operated in this region because the operating switching frequency is very low in this region. And, since there is no ZVS in the primary side switches, MOSFETs can no longer to be used in this converter

2.2 Design of Bidirectional Converter

The resonant network in the *CLLLC*-type converter has five elements (L_1, L_2, L_m, C_1 and C_2). There is a transformer for galvanic isolation. L_m is the magnetizing inductance of this transformer. The elements in the secondary side can be referred to the primary-side as shown in Fig. 2.18. If the transformer turns ratio in the original circuit is n_{CLLLC}. Then,

$$L_2' = {n_{CLLLC}}^2 \cdot L_2 \tag{2.13}$$

$$C_2' = \frac{1}{{n_{CLLLC}}^2} \cdot C_2 \tag{2.14}$$

$$R_{ac}' = {n_{CLLLC}}^2 \cdot \frac{8}{\pi^2} R_L \tag{2.15}$$

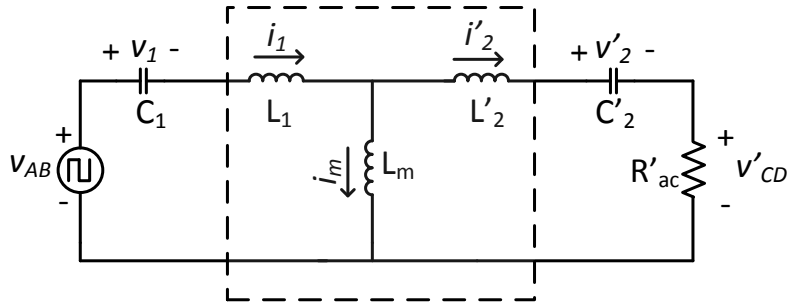

Fig. 2.18. Equivalent circuit after referring elements from the secondary side to the primary side.

2.2.1 Design of CLLLC Resonant Network

There are few points that need to be considered while designing the converter.

i) The operating frequency should be very high to reduce the size of the magnetics and the output filter capacitor. The voltage across the resonant capacitor is inversely proportional to the operating switching frequency. Higher switching frequency is desirable for a lower capacitor voltage stress. So, the converter should be designed such that the normal operating switching frequency range is high.

ii) The converter is designed to have ZVS in the primary side switches and soft commutation in the secondary side switches to maximize the efficiency and to make very high-frequency operation possible.

iii) To minimize the circulating reactive energy in the resonant tank, the phase angle, φ, between the input square voltage and input current should be small.

iv) The designed converter should meet the voltage gain requirements in both directions of energy flow.

v) The gain curves should be monotonically decreasing to enable linear control over the entire operating frequency range for both modes of operation where by then, linear control techniques can be adapted easily.

Design of the converter involves determining transformer turns ratio (n_{CLLLC}), design of magnetizing inductance (L_m), design of resonant inductances (L_1 and L'_2) and resonant capacitances (C_1 and C'_2). Once L'_2 and C'_2 are designed, L_2 and C_2 can be calculated using equations (2.13) and (2.14).

2.2.1a Design of Transformer Turns Ratio (n_{CLLLC})

In resonant converters, the efficiency of the power stage is maximum at the primary side series resonant frequency, f_{ser}. Thus, the converter should operate at this frequency under nominal operating conditions. If the primary switches and the secondary diodes are assumed to be ideal, then the transformer turns ratio can be calculated as,

$$n_{CLLLC} = \frac{N_1}{N_2} = \frac{V_{in}}{V_{o\_nom}} \tag{2.16}$$

2.2.1b Design of Magnetizing Inductance (L_m)

ZVS can be ensured in the primary-side switches by keeping the current through these switches negative on the instant they are turned on. The primary current should be able to charge and discharge the output capacitors of the primary side switches during the dead-time. The magnitude of this current depends on the magnetizing inductance and the duration of the dead-time. So, the ZVS in the primary side depends on the magnetizing inductance, the switch output capacitance, the operating switching frequency and the dead-time duration. The operation of this converter during the dead-time is similar to the operation of LLC resonant converter during dead-time [50]. So, the magnetizing inductance can be designed using the same expression as the full-bridge LLC resonant converter. This relationship is,

$$L_m \leq \frac{T.t_{dead}}{16C_{oss}} \tag{2.17}$$

Having a very small Magnetizing inductance will ensure ZVS in the primary side switches at all load and line conditions. However, L_m cannot be too low. As, it would make the magnetizing current very high, resulting in huge conduction losses, increased apparent power requirements for switches and increased peak voltage requirement for the primary side capacitor. Large magnetizing inductance will result in a small magnetizing current, but it limits the voltage gain of the converter. So, magnetizing inductance cannot be too large.

Dead-time between the switches also affect the ZVS range. Longer dead-time will help in achieving ZVS for wide input and output voltage range. And, with large dead-time, the magnetizing inductance can be made large to reduce the magnetizing current. However, longer dead-time will result in large primary RMS current as no energy is transferred during dead-time. All these factors should be kept in mind while designing the magnetizing inductance.

2.2.1c Design of Leakage Inductances (L_1 and L'_2)

To simplify the design process, it will be assumed that L'_2 is equal to L_1. The inductance ratio, L_n, is defined as,

$$L_n = \frac{L_m}{L_1} \tag{2.18}$$

The voltage gain and the operating switching frequency range of this converter depend on the inductance ratio, L_n. For a narrow operating frequency range, L_n should be small. However, small L_n will result in large leakage inductances, thus the size of magnetics can be large. For a large L_n, the gain of the converter is limited, and the operating frequency range is wide. Fig. 2.22 and Fig. 2.23 show the voltage gain curves under the same load conditions for different values of L_n.

2.2.1d Design of Resonant Capacitances (C_1 and C'_2)

The efficiency of the converter is maximum at the primary-side series resonant frequency, f_{ser}. Converter is operated at this frequency under nominal operating conditions. The choice of this frequency determines the operating frequency range of the converter. So, C_1 is designed based on the operating frequency range in the *BCM*. For a series resonant frequency of f_{res},

$$C_1 = \frac{1}{L_1(2\pi f_{res})^2} \tag{2.19}$$

The capacitance ratio, C_n, is defined as,

$$C_n = \frac{C'_2}{C_1} \tag{2.20}$$

C_n can be designed such that the voltage gain curves are monotonically decreasing, and they meet the voltage gain requirements in both *BCM* and *RM*. C'_2 determines the secondary side series resonant frequency, and the converter will operate at this frequency under nominal conditions in the *RM*. In other words, C'_2 determines the operating switching frequency of the converter in the *RM*. So, C_n cannot be too large, as this will make the converter operate at lower switching frequencies in the *RM*.

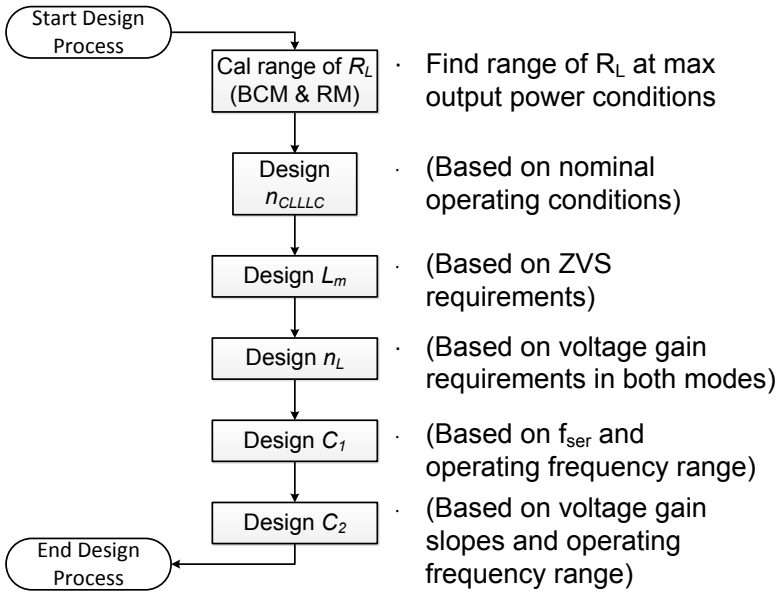

Fig. 2.19. Design flowchart for the proposed design methodology.

2.2.2 Deriving CLLC from CLLLC Network

In the *CLLLC*-type resonant network, there are three magnetic units (L_1, L_2 and L_m) and two capacitors (C_1 and C_2). To reduce the number of magnetics in the resonant network, a *CLLC*-type network, with only two magnetic units, can be derived from the *CLLLC*-type network. The T-network consisting of three inductances L_1, L_2 and L_m in the *CLLLC*-type resonant network is shown in Fig. 2.20. The equivalent circuit consisting of an inductor, L_r and a transformer with magnetizing inductance M is shown in Fig. 2.20(b).

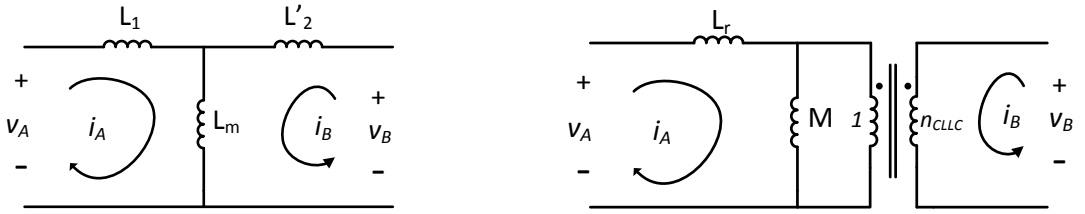

(a) L_1, L_2 and L_m in a *CLLLC* resonant network. (b) L_r, M and n_{CLLC} in a *CLLC* resonant network

Fig. 2.20. Deriving *CLLC* resonant network from *CLLLC* network.

The following equations show the terminal voltages in term of the loop currents for the T-network shown in Fig. 2.20(a).

$$v_A = (L_1 + L_m)\frac{d}{dt}i_A + L_m\frac{d}{dt}i_B \tag{2.21}$$

$$v_B = L_m\frac{d}{dt}i_A + (L_2' + L_m)\frac{d}{dt}i_B \tag{2.22}$$

The terminal voltages for the equivalent circuit in Fig. 2.9(b) in terms of loop currents are,

$$v_A = (L_r + M)\frac{d}{dt}i_A + n_{CLLC}\cdot M\frac{d}{dt}i_B \tag{2.23}$$

$$v_B = n_{CLLC}\cdot M\frac{d}{dt}i_A + {n_{CLLC}}^2\cdot M\frac{d}{dt}i_B \tag{2.24}$$

These four equations (2.21) - (2.24) can be solved for n_{CLLC}, L_r and M.

$$n_{CLLC} = \frac{(L_2' + L_m)}{L_m} \tag{2.25}$$

$$M = \frac{{L_m}^2}{(L_2' + L_m)} \tag{2.26}$$

$$L_r = \frac{(L_1 + L_m)\cdot(L_2' + L_m) - {L_m}^2}{(L_2' + L_m)} \tag{2.27}$$

So, the equivalent *CLLC* resonant converter becomes,

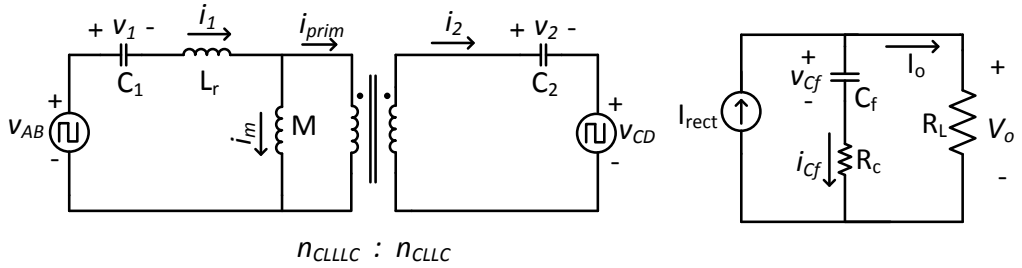

Fig. 2.21. Equivalent circuit diagram for converter in Fig. 2.1 with *CLLC* resonant network

The two resonant networks have same terminal voltages and loop currents. So, the gain curves and the voltage and current waveforms shown in Fig. 2.5, Fig. 2.14 and Fig. 2.15 are identical for both resonant networks.

2.3 Design Example

As a design example, a 3.5 kW bidirectional converter is to be designed with a dc bus voltage of 400 V and output battery voltage of 250 V ~ 450 V. So, the voltage gain requirement of the converter in the battery charging mode is 0.625 ~ 1.125. The voltage gain requirement in the regeneration mode is 0.89 ~ 1.60. The nominal battery voltage is 400 V. And, the primary side series resonant frequency is chosen to be 100 kHz.

For a nominal battery voltage of 400 V, the transformer turns ratio comes out to be 1. For a resonant frequency of 100 kHz, a dead-time of 200 nSec and switch output capacitance of 250 pF, the magnetizing inductance comes out to be,

$$L_m \leq \frac{\left(\frac{1}{100\times10^3}\right)\times(200\times10^{-9})}{16\times250\times10^{-12}} = 500\ \mu H$$

A magnetizing inductance of 500 µH or less will ensure ZVS in the primary-side switches. Fig. 2.22 shows the voltage gain curves for L_m equals to 300 µH and 200 µH. It can be seen that for larger L_m, the gain of the converter is limited, and there is bifurcation (multiple peaks) in the curves. The maximum voltage gain requirement for the converter is 1.6 in the *RM*, when the dc bus voltage is 400 V and battery voltage is 250 V. This voltage gain can be achieved for an L_m of 200 µH or less.

The next step is to design the resonant inductances, L_1 and L'_2. To design the inductance ratio, the voltage gain curves are plotted for different values of L_n in Fig. 2.22 and Fig. 2.23. For a value of L_m equals to 200 µH and L_n equals to 10, the converter is able to meet the maximum voltage gain requirement. However, the operating frequency range for the converter will be very wide. A small L_m and a small L_n can narrow down the operating frequency range, however it will

result in larger magnetics. So, there is a trade-off between the size of the converter and the operating switching frequency range.

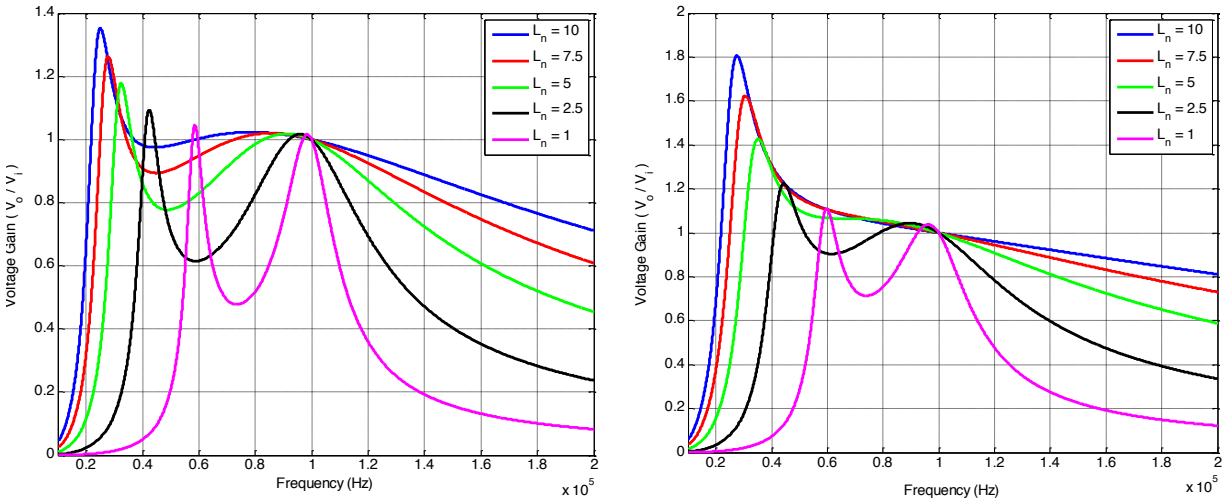

(a) L_m = 300 µH, f_{res} = 100 kHz and R_L = 80 Ω (b) L_m = 200 µH, f_{res} = 100 kHz and R_L = 80 Ω

Fig. 2.22. Voltage gain curves for different values of L_n when L_m = 300 µH and 200 µH.

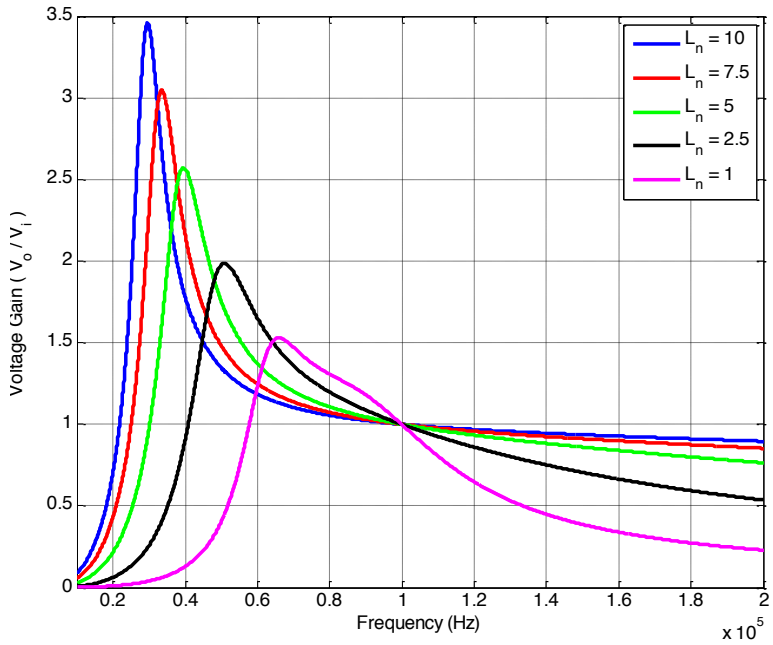

Fig. 2.23. Voltage gain curves for converter with L_m = 100 µH, f_{res} = 100 kHz and R_L = 80 Ω.

An L_m of 100 µH and an L_n equal to 5 can meet voltage gain requirements in both directions. And with these inductances, the operating switching frequency range is not very wide. So, the resonant inductances come out to be,

$$L_1 = L'_2 = 20\ \mu H$$

C_1 can be calculated from the resonant frequency and the resonant inductance. It comes out to be,

$$C_1 = \frac{1}{L_1(2\pi f_{res})^2} \approx 125\ nF$$

To make the gain curves monotonically decreasing and to meet the voltage gain requirement in both modes, C_n was chosen to be 1.6. So C_2 comes out to be,

$$C'_2 = 1.6 \times 125\ nF = 200\ nF$$

This value of C'_2 will make the secondary side series resonant frequency to be 80 kHz. Since, n_{CLLLC} is equal to 1. So, L_2 and C_2 are equal to L'_2 and C'_2 respectively. For *CLLC* resonant network, L_r, M and n_{CLLC} can be calculated using equations (2.25) – (2.27).

$$L_r = 36.67\ \mu H$$

$$M = 83.33\ \mu H$$

$$n_{CLLC} = 1.2$$

The voltage gain curves for the designed converter in the battery charging mode are shown in Fig. 2.24 while the voltage gain curves for the designed converter in the regeneration mode are shown in Fig. 2.25.

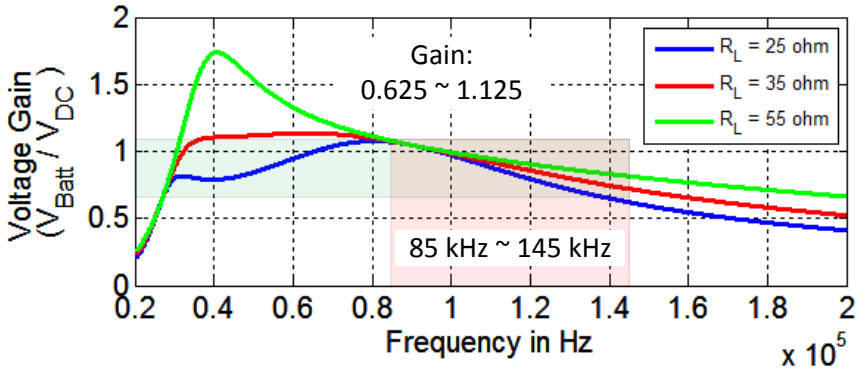

Fig. 2.24. Voltage gain curves for designed converter operating in Battery Charging Mode.

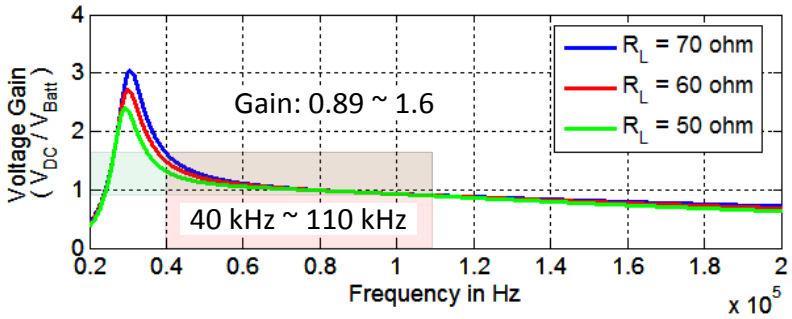

Fig. 2.25. Voltage gain curves for designed converter operating in Regeneration Mode.

These gain curves show that the designed converter meets the voltage gain requirement in both directions. These gain curves give information about the operating frequency range of the converter. The operating frequency range for converter operating in battery charging mode is 85 kHz ~ 145 kHz. And, the operating frequency range for the converter operating in the regeneration mode is 40 kHz ~ 110 kHz.

2.3.1 Experimental Results

To validate the converter design, a 3.5 kW bidirectional resonant converter was built in lab. Both resonant networks, *CLLLC* and *CLLC* are built. For a *CLLLC* configuration, the inductances in the resonant network consist of L_1, L_2 and L_m. And, for a *CLLC* configuration, the inductances are L_r and M. The values of these inductances are listed in Table 2.1. The resonant capacitance in the dc bus side consists of two capacitors each 68 nF, 5PT46L683, in parallel. And in the battery side, two capacitors each of 100 nF, 5PT46L104, are in parallel. Experiments

showed that the rectifying diodes having longer reverse recovery time affected the converter gain curves in the regeneration. Infineon IGBTs, IKW40N65F5, have better antiparallel diodes as compared to the body-diodes of MOSFETs. So, these IGBTs were selected as switches $Q_A \sim Q_D$. For switches $Q_E \sim Q_H$, Fairchild MOSFETs, FCH041N65F were selected.

For experiments, the programmable electronic load, BK Precision 8526 5000W, is used. In the *BCM*, the e-load is programmed as a battery load whose voltage is varied from 250V to 450V. In the *RM*, the e-load is programmed as a current source whose current is varied from 0.5A to 8.5A to emulate the ac-dc stage. The circuit parameters for the designed converter are listed in table 2.1. And, table 2.2 compares the magnetics in both *CLLLC*-type and *CLLC*-type resonant networks. Fig. 2.26 shows the 3.5 kW *CLLLC*-type converter build in the lab.

Table 2.1 Circuit parameters

V_{DC}	400 V
L_1	18.87 µH
L_2	19.16 µH
C_1	2 x 68 nF
C_2	2 x 100 nF
L_m	94.2 µH
n_{CLLLC}	1
L_r	34.8 µH
M	78.28 µH
n_{CLLC}	1.2
C_{DC}	30 µF
C_f	30 µF
V_{Batt} (e-load in *BCM*)	250 V ~ 450 V
i_{DC} (e-load in *RM*)	0.5 A ~ 8.5 A
$Q_A \sim Q_D$	IKW40N65F5
$Q_E \sim Q_H$	FCH041N65F

Table 2.2 Magnetics comparison for the CLLLC and CLLC-type resonant converter

	CLLLC-type resonant converter	CLLC-type resonant converter
Resonant inductor core	ETD 49/25/16 –	ETD 49/25/16 – 3C95

	3C95	
No. of turns in each resonant inductor	12	15
Air-gap in resonant inductor cores	1.85 mm	1.56 mm
Weight of each resonant inductor	250 g	250 g
Volume of each resonant inductor	100 cm^3	100 cm^3
Transformer core	EE 65/32/27 – 3C95	EE 65/32/27 – 3C95
No. of turns in transformer	18:18	15:18
Air-gap in transformer cores	1.84 mm	1.41 mm
Weight of transformer	800 g	800 g
Volume of transformer	215 cm^3	215 cm^3

It can be seen in table (2.1) that the total volume of the magnetics in the *CLLLC*-type resonant converter is 415 cm^3, whereas in the *CLLC*-type resonant network, it is 315 cm^3. And, the total weight of the magnetics in the *CLLLC*-type resonant converter is 1300 g, whereas in the *CLLC*-type resonant converter, it is only 1050 g. So, the volume and the weight of magnetics in the *CLLC*-type resonant converter are much lower as compared to the volume and the weight of the magnetics in the *CLLLC*-type resonant converters.

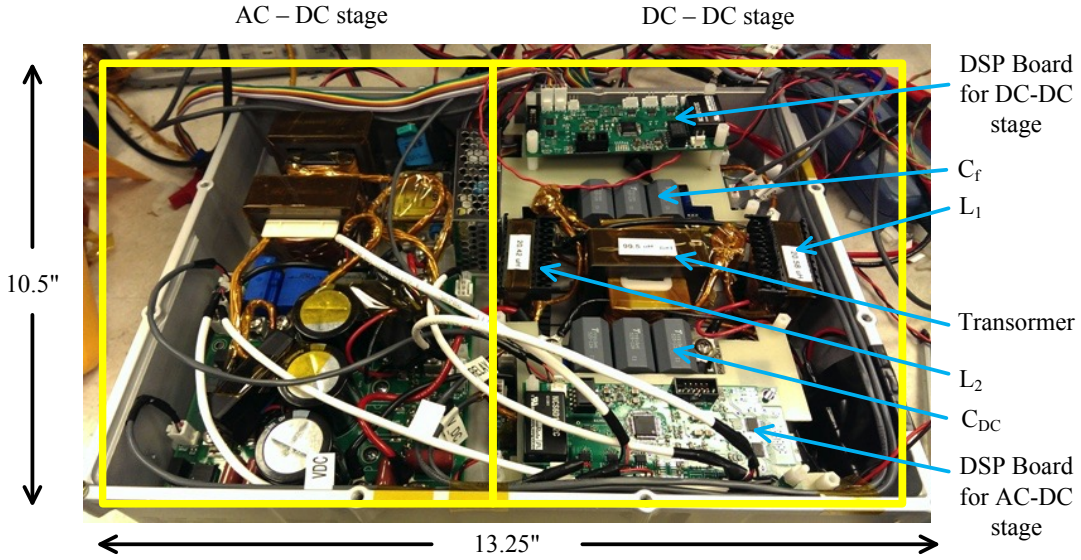

Fig. 2.26. 3.5 kW bidirectional battery charger build in lab.

2.3.2 Converter Start-up

One of the major issues with the resonant converters is the start-up surge current. In most of the resonant converters, the output filter capacitor short-circuits the magnetizing inductance at the start-up. So, the input impedance is very small resulting in a huge start-up current. In this topology, there is an inductor and a capacitor in the secondary side. The output capacitor does not short the resonant network making the input impedance always inductive. So, the converter never loses ZVS in the primary-side switches, even at the start-up. To limit the surge current, the operating switching frequency is kept slightly higher than the normal operating frequency range at the start-up.

In the *BCM*, the ac-dc stage charges the dc bus capacitor. Once the dc bus voltage reaches 380 V, the dc-dc stage is turned on. The e-load voltage takes some time to reach the rated voltage. During this time, the operating switching frequency is kept constant at 200 kHz to limit the surge current. Once the e-load voltage is 250 V, the converter can be operated normally with its output current-loop closed. Fig. 2.27 shows the converter start-up in the *BCM*. It can be seen that the start-up current is 23 A, which is slightly higher than the peak steady-state current of 20 A.

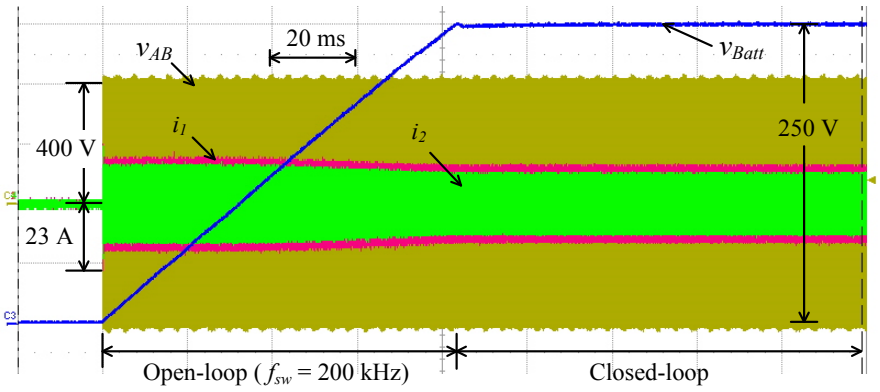

Fig. 2.27. Converter start-up in the *BCM*.

In the *RM*, the battery charges the dc bus at the start-up. Once the dc bus voltage reaches 380 V, the ac-dc stage is turned on. The start-up of the converter in the *RM* is shown in Fig. 2.28. At

the start of the start-up process, the converter is operated in an open-loop at a switching frequency of 200 kHz. Once the dc bus voltage reaches 250 V, the converter is operated in the closed-loop with the dc bus voltage reference ramped up very slowly to 400 V. It can be seen that the start-up current is not very high. It is 30A for a worst-case of battery voltage of 450 V. The converter output voltage can go very high at no-load condition. To limit the output voltage, a burst mode is implemented. This burst mode keeps the dc bus voltage at 420 V at no-load conditions.

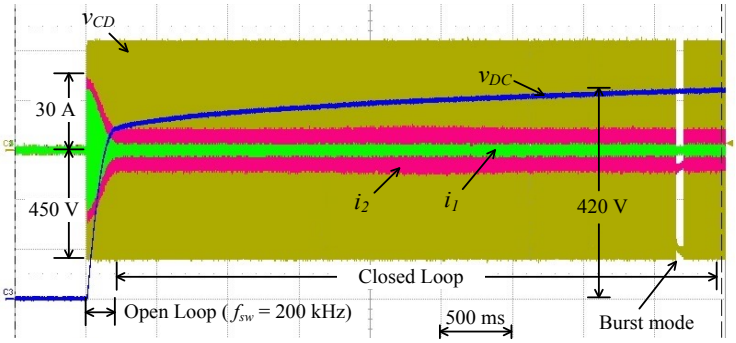

Fig. 2.28. Converter start-up in the *RM* at the worst-case of V_{batt} = 450 V.

2.3.3 Converter Operation in Battery Charging Mode

In the *BCM*, the switches $Q_A \sim Q_D$ act as a high-frequency inverter while the body-diodes of the switches $Q_E \sim Q_H$ act as a rectifier bridge charging the output battery. The output voltage, output current and input impedance phase versus the frequency for the designed converter are plotted in Fig. 2.29.

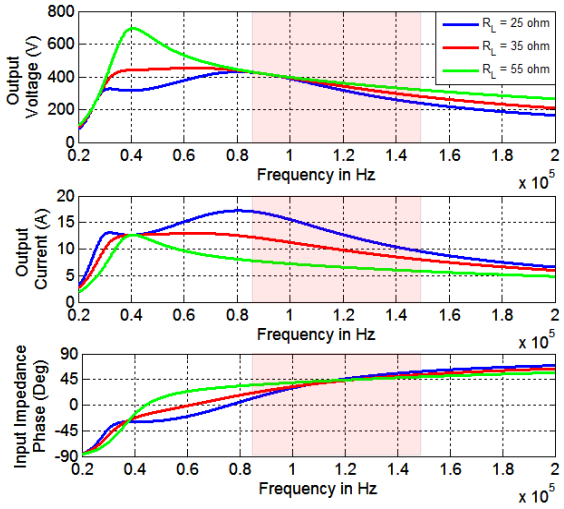

Fig. 2.29. Output voltage, output current and input impedance phase versus operating switching frequency for converter operating in the *BCM*.

The output charging current versus the battery voltage for the converter operating in the *BCM* is shown in Fig. 2.30. During the constant current mode, a constant current charges the output battery. The output current is limited to 10 A for the lower battery voltages. For higher battery voltages, the charging current is reduced to keep the output power at 3.5 kW.

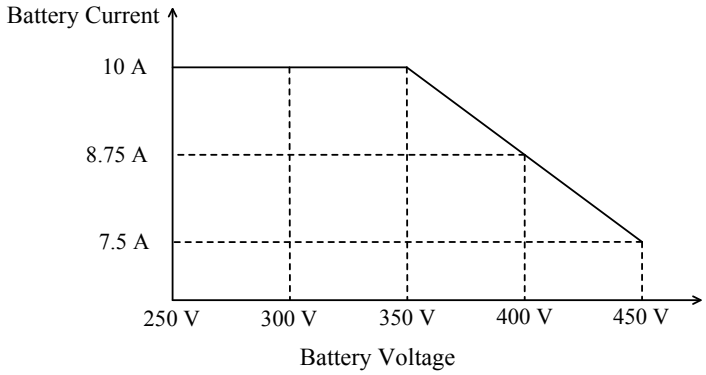

Fig. 2.30. Battery current versus the battery voltage for the converter operating in the *BCM*.

Fig. 2.31 shows the measured current and voltage waveforms for the converter operating in the *BCM* under different battery voltages.

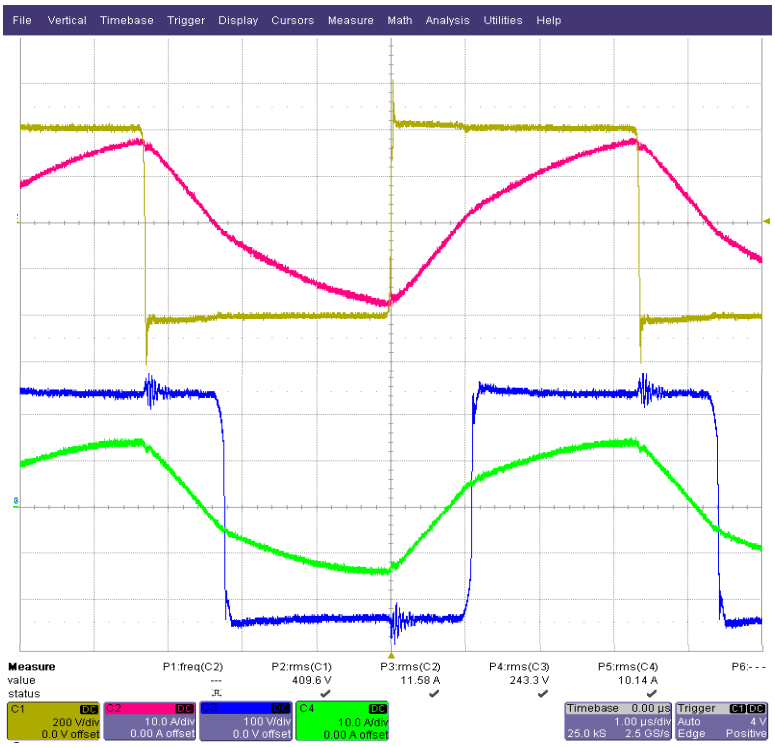

(a) V_{Batt} = 250 V and I_{Batt} = 10 A (Buck mode in Region 1)

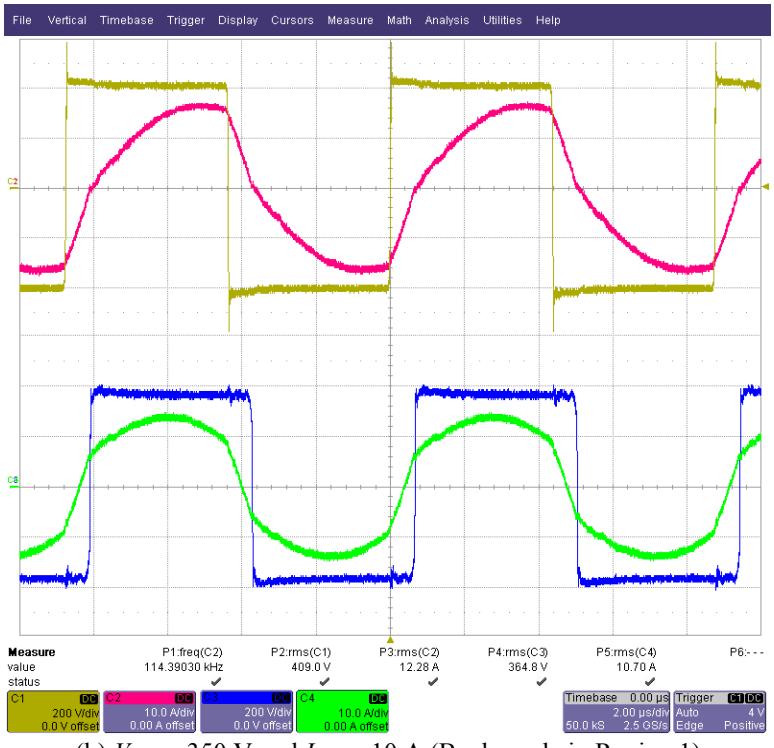

(b) V_{Batt} = 350 V and I_{Batt} = 10 A (Buck mode in Region 1)

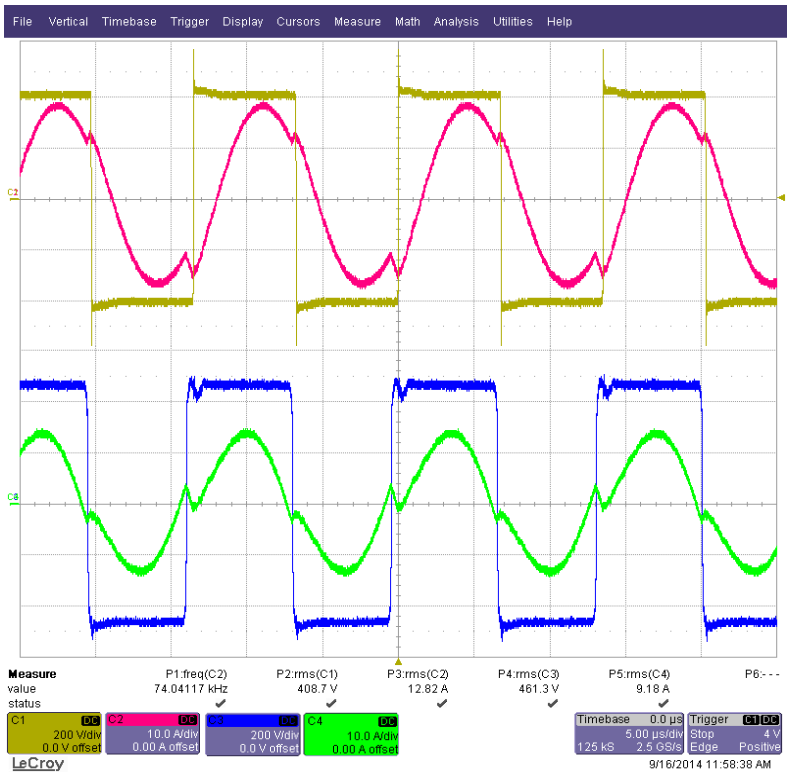

(c) V_{Batt} = 450 V and I_{Batt} = 7.5 A (Boost mode in Region 2)

Fig. 2.31. Voltages and currents for the converter operating in the *BCM* with V_{DC} = 400 V, Yellow = Primary-side bridge voltage, v_{AB}, Red = Primary-side current, i_1, Blue = Secondary side bridge voltage, v_{CD}, and Green = Secondary side current, i_2

It can be seen that for a lower battery voltage, the gain of the converter is less than 1. So, the converter operates in region 1, and switching frequency is higher than the f_{ser}. For a battery voltage of 450 V, the converter gain is more than 1, and the converter operates in Region 2 and the operating switching frequency is lower than the f_{ser}.

Fig. 2.32 shows the power-stage measured efficiency for the converter operating in the *BCM*. The solid line represents the efficiency of the converter power-stage with a *CLLLC*-type resonant network, while the dashed line represents the efficiency of the power stage with a *CLLC*-type resonant network. For lower battery voltages, the efficiency is lower as the converter operates at the frequencies much higher than the f_{ser}. The efficiency is maximum for the battery voltage of 400 V as the gain of the converter is unity, and the converter operates at the series resonant frequency. The peak power-stage efficiency for the converter is 97.7 %.

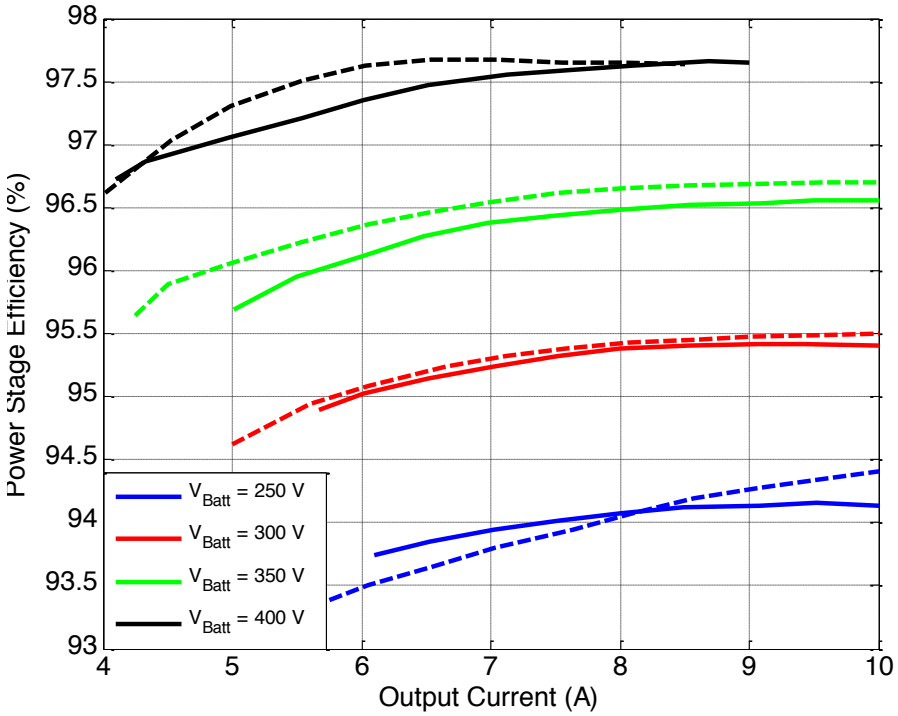

Fig. 2.32. Efficiency of the power stage for different battery voltages under different load conditions for converter operating in battery charging mode for both *CLLLC* and *CLLC* resonant converters.

2.3.4 Converter Operation in Regeneration Mode

In the *RM*, the switches $Q_E \sim Q_H$ act as a high frequency inverter while the anti-parallel diodes of the switches $Q_A \sim Q_D$ act as a rectifier bridge delivering power to dc bus. The output voltage, output current and input impedance phase versus frequency are plotted in Fig. 2.33.

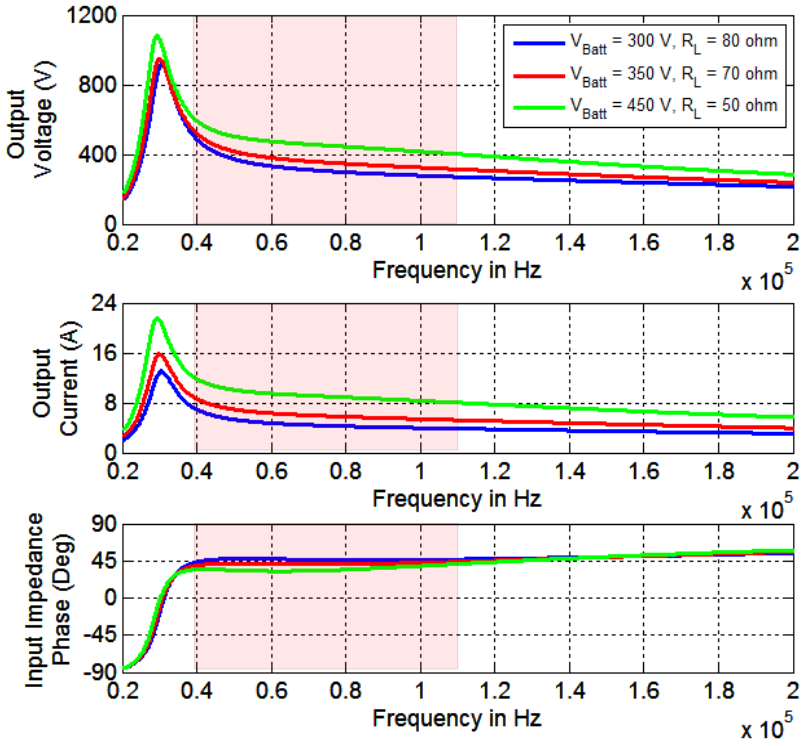

Fig. 2.33. Output voltage, output current and input impedance phase versus operating switching frequency for converter operating in *RM*.

In the *RM*, the converter keeps the dc bus voltage constant for a wide range of battery voltages. In this mode, the converter primary-side rms current, i_2, can get very high for higher output power conditions. So, to limit this current, the output power is reduced at lower battery voltages. Converter output power versus the battery voltage for the converter operating in the *RM* is shown in Fig. 2.34.

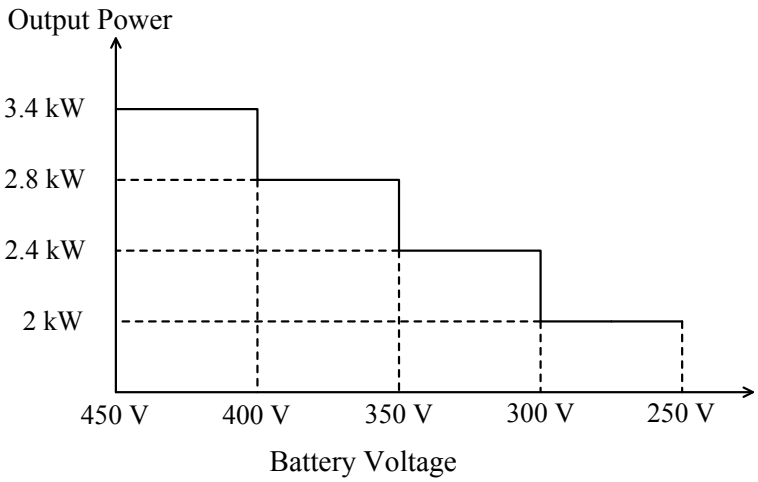

Fig. 2.34. Converter output power versus the battery voltage for the converter operating in the *RM*.

Fig. 2.35 shows the measured current and voltage waveforms for the converter operating in the *RM* under different load conditions.

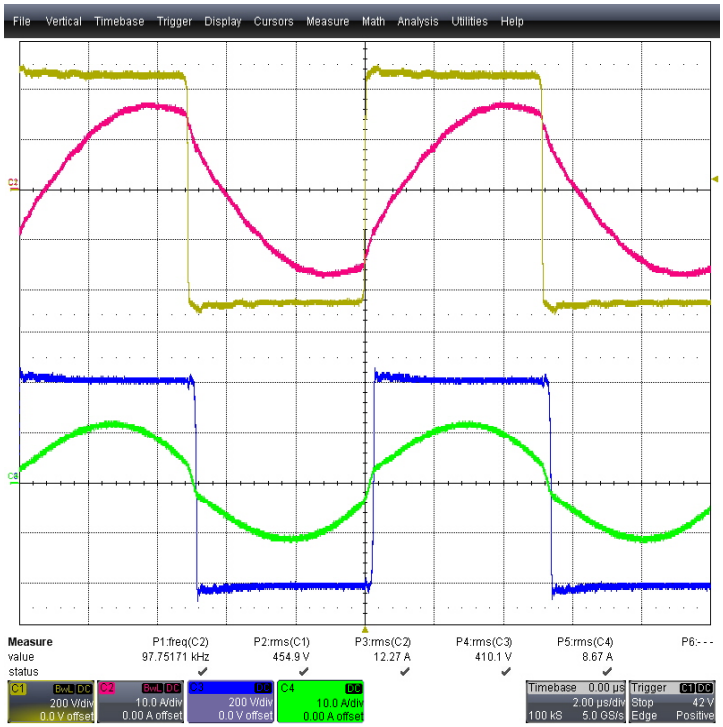

(a) V_{Batt} = 450 V and I_{DC} = 8.5 A (Buck mode in Region 1)

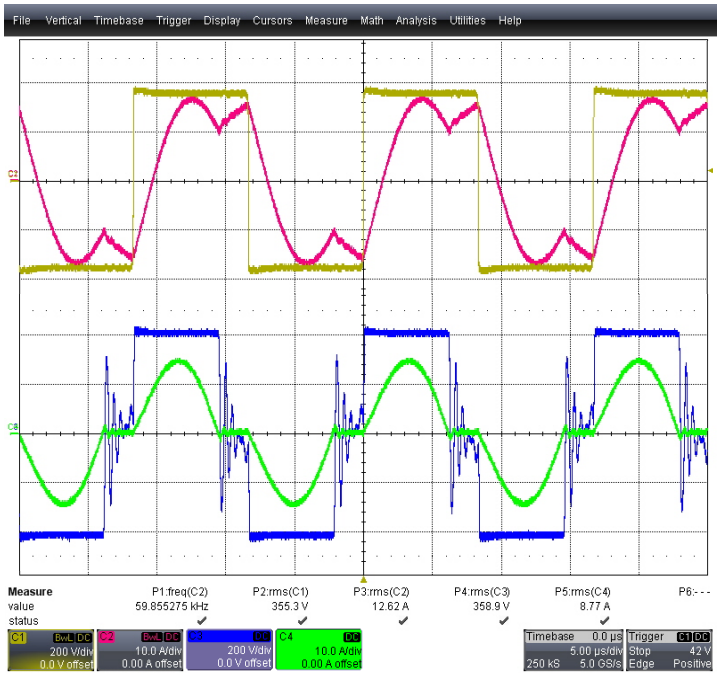

(b) V_{Batt} = 350 V and I_{DC} = 7 A (Boost mode in Region 2)

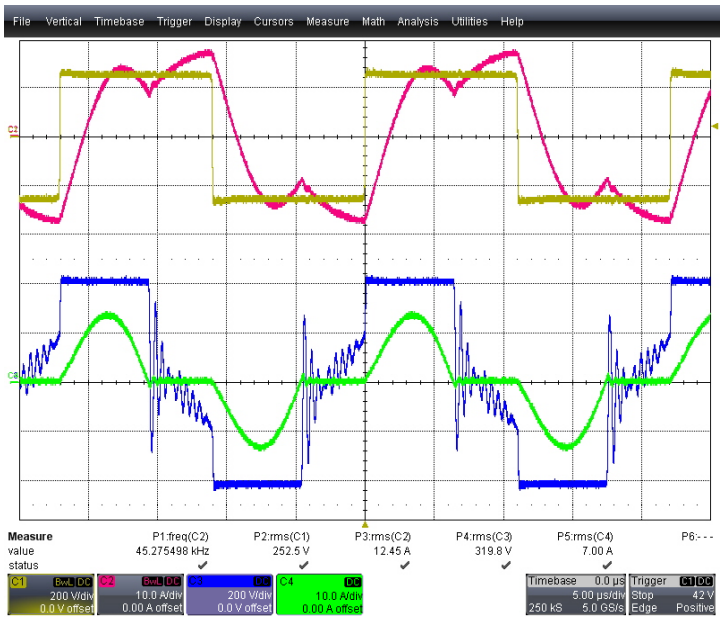

(c) V_{Batt} = 250 V and I_{DC} = 5 A (Boost mode in Region 2)

Fig. 2.35. Voltages and currents for converter operating in the *RM* with V_{DC} = 400 V, Yellow = Secondary side bridge voltage, v_{CD}, Red = Secondary side current, i_2, Blue = Primary-side bridge voltage, v_{AB}, and Green = Primary-side current, i_1

It can be seen that for higher battery voltages, the gain of the converter is less than 1. So, the converter operates in region 1, and switching frequency is higher than the f_{ser}. For lower battery voltages, the converter gain is more than 1, and the converter operates in region 2 and the operating switching frequency is lower than the f_{ser}.

Fig. 2.36 shows the power-stage measured efficiency for converter operating in the *RM*. It can be seen that the efficiency for a *CLLLC*-type configuration is higher than the *CLLC*-type configuration in the *RM*. The peak efficiency for the converter with the *CLLLC*-type configuration is 98.10 %. While, the peak efficiency in the *CLLC*-type configuration is 97.9 %.

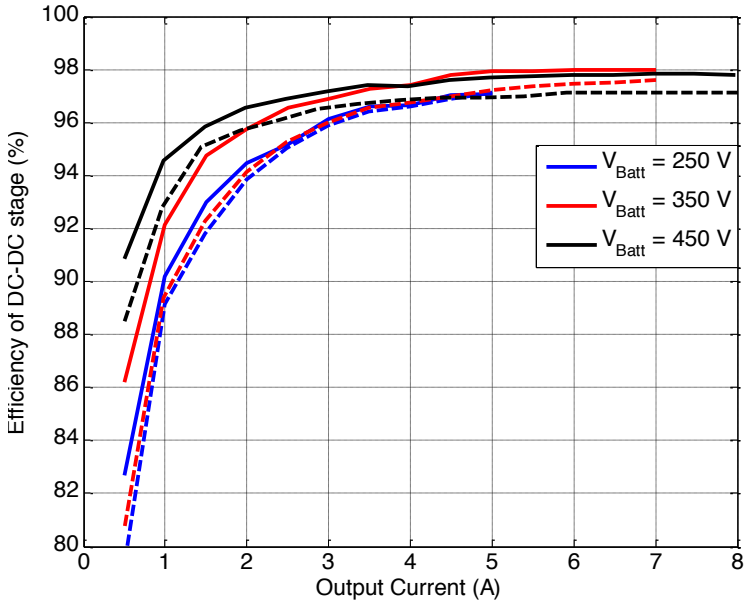

Fig. 2.36. Efficiency of power stage for different battery voltages under different load conditions for converter operating in regeneration mode for both *CLLLC* and *CLLC* resonant converter.

The losses in the power-stage can be divided into losses in the active switches, losses in the rectifying diodes and losses in the magnetics. Fig. 2.37 shows the loss breakdown for the converter operating in the *BCM* at 3.5 kW output load. The losses are slightly lower for the *CLLC* configuration resulting in higher efficiency. Fig. 2.38 shows the loss breakdown for the converter operating in the *RM* at 3.2 kW output load. The losses are slightly higher for *CLLC* configuration resulting in slightly lower efficiency.

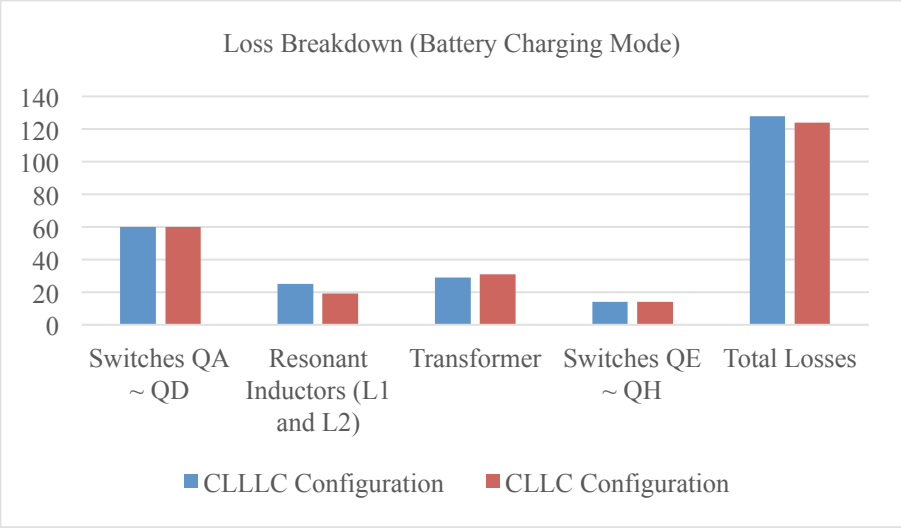

Fig. 2.37. Loss breakdown for converter operating in *BCM* at V_{Batt} = 350 V and I_o = 10A.

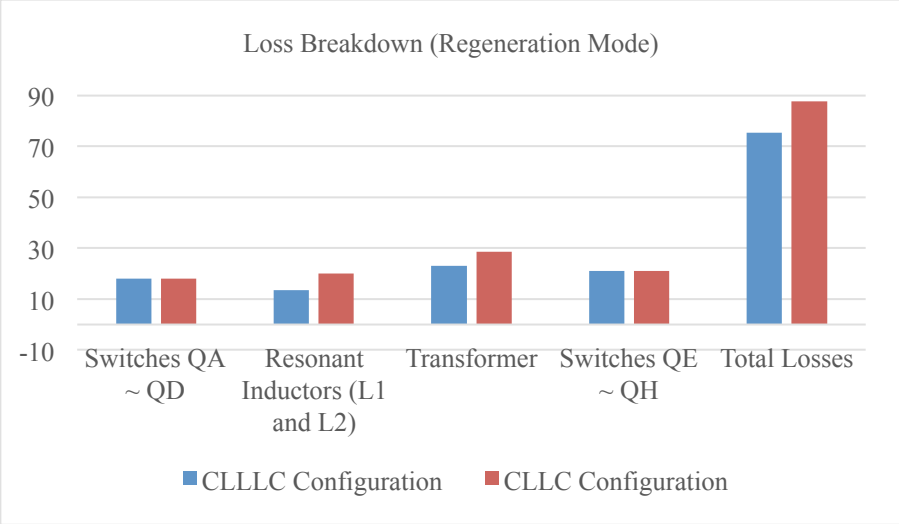

Fig. 2.38. Loss breakdown for converter operating in *RM* at V_{Batt} = 400 V, V_{DC} = 400 V and I_{DC} = 8A.

2.4 Conclusions

The *CLLLC*-type resonant converter is similar to an *LLC*-type resonant converter with an extra inductor and capacitor in the secondary-side. Soft-switching can be ensured in all the switches without additional circuitry. Because of soft-switching in all switches, very high-frequency operation is possible thus the size of the magnetics and the capacitors can be made small. In this paper, first an equivalent model for the *CLLLC*-type converter was derived for the steady-state analysis. This model was used to get the voltage and current gain curves for any load and line conditions. These gain curves verify the design of the power-stage, and give information about the operating frequency range of the converter. Then, the design methodology for a *CLLLC*-type configuration was presented in detail. Design of the converter includes determining the transformer turns ratio, determining the magnetizing inductance based on ZVS condition, and determining the resonant inductances and capacitances. Then, the *CLLC*-type resonant network was derived from the *CLLLC*-type network.

Major contributions of this chapter include:

- To propose a design methodology for a *CLLLC*-type bidirectional resonant converter for a battery charging applications. The charging process for a battery usually contains several stages, and the output voltage and the load power change significantly during the whole charging process. The design methodology proposed in this paper takes these processes into account. This design methodology will ensure that the voltage gain curves are always monotonically decreasing for all load and line conditions in both *BCM* and *RM* so that a linear controller can be designed to regulate the output current and voltage.
- The derivation of the *CLLC*-type resonant equivalent network from a *CLLLC*-type resonant network. Usually, in a resonant converter, the heaviest and bulky component is the inductor and/or a transformer. In this paper, a *CLLC*-type resonant network is derived from the *CLLLC*-type network. This resonant network has one less inductor. So, the weight and size of the converter can be reduced. The advantage is more significant for very high-power applications.

To validate the design procedure, a 3.5 kW converter was designed and built in lab following the guidelines in the proposed methodology as a design example. A *CLLC*-type network was derived from it. Experimental results verified both the designs. It was found that the *CLLC*-type network was more compact and lighter in weight as compared to the *CLLLC*-type network. The total volume and weight of the magnetics in *CLLLC*-type network were 415 cm^3 and 1300 g respectively, whereas in the *CLLC*-type network, the volume and the weight of the magnetics are 315 cm^3 and 1050 g respectively. Soft switching was ensured in the switches for a wide voltage range and a wide load range. As a result, the efficiency of the converter was high for both the *BCM* and the *RM*. Under different load conditions, the power-stage efficiency with a *CLLC* configuration is generally higher than the efficiency with a *CLLLC* configuration in the *BCM*. On

the other hand, the efficiency with a *CLLLC* configuration is generally higher than the efficiency with *CLLC* configuration in the *RM*. For a *CLLLC* configuration, the peak efficiency was 97.7% under *BCM* and 98.1% under *RM*. For a *CLLC* configuration, the peak efficiency was 97.7% under *BCM* and 97.9% under *RM*.

Chapter 3 Modeling of the Power Stage

3.1 Introduction

The dynamics analysis of any converter is necessary to design the control loop. The bandwidth, phase margin and gain margin of the control loops should be properly designed to guarantee a robust system. In the PWM converters, the switching frequency of the converter is much higher than the output filter cut-off frequency. This allows methods like state-space averaging technique [51] and PWM switch model technique [52, 53] to be used to derive the average model of the converter over one switching period to evaluate the overall dynamic performance of the system. These methods cannot be used directly in the resonant converters to derive the transfer functions of the converter as the switching frequency in these converters is close to the resonant frequency of the resonant tank circuit. In the past, several methods were proposed to derive the small-signal model of the resonant converters. However, these methods are either very complex [54, 55] or not accurate enough [56-58]. Generalized State-Space Averaging (GSSA) [59, 60] is another tool for modeling the dynamics of resonant converters. But, this technique becomes very complex and less accurate for higher order converters. Another modeling technique based on combined time-domain analysis and frequency-domain analysis employing Extended Describing Functions (EDF) is proposed in the literature [61-64]. This method is not very complex and is accurate.

The equivalent circuit diagram for the bidirectional resonant converter that was derived in Section 3.1 is shown in Fig. 3.1. The equivalent circuit topology is similar to the equivalent circuit topology for the Series-Series compensated Induction Power Transfer (IPT) System [41-

45], which allows the dynamic analysis presented here to be valid there. The only difference is for a loosely coupled transformer in IPT, the turns ratio is equal to 1 however in the tightly coupled resonant converter, it is equal to the actual transformer turns ratio.

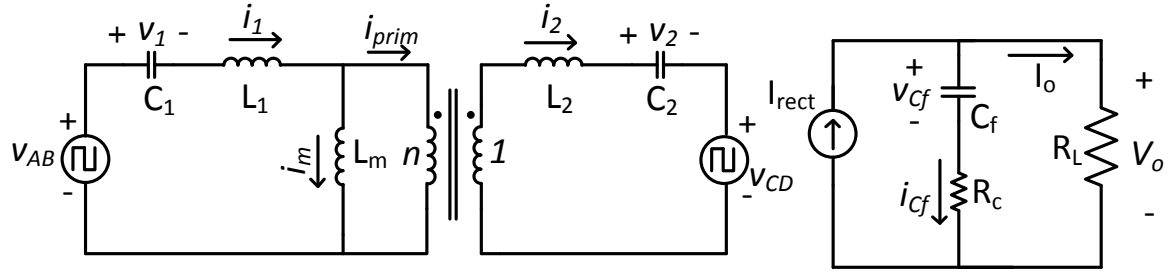

Fig. 3.1. The equivalent circuit diagram for the resonant converter and the IPT system operating in the BCM.

3.2 Dynamic Analysis of the Bidirectional DC-DC Converter

In this Section, the large-signal model, the steady-state model and the small-signal model for the IPT system are derived based on Extended Describing Functions with the following assumptions:

i) All the secondary diodes are ideal with no reverse recovery and no junction capacitance.

ii) Resonant capacitor currents, i_1 and i_2, are pure sinusoidal.

iii) Dead-time is neglected. So, the input voltage, v_{AB}, is a pure square wave.

iv) The input voltage, v_{AB}, is the reference voltage. The phase of all the currents and voltages in the converter are measured with respect to this voltage.

3.2.1 Nonlinear State-Space Equations

Applying KVL to the loops in the circuit in Fig. 3.2, the following is derived:

$$v_{AB}(t) = v_1(t) + L_1 \frac{d}{dt} i_1(t) + L_m \frac{d}{dt}\left(i_1(t) - i_{prim}(t)\right) \tag{3.1}$$

$$\frac{1}{n} v_m(t) = \frac{1}{n} L_m \frac{d}{dt} i_m(t) = v_2(t) + L_2 \frac{d}{dt} i_2(t) + v_{CD}(t) \tag{3.2}$$

Magnetizing current, i_m, can be written in terms of i_1 and i_2.

$$i_m(t) = i_1(t) - \frac{i_2(t)}{n} \tag{3.3}$$

These three equations are solved to get the following,

$$\frac{d}{dt} i_1 = \frac{1}{L_{eq2}}\, v_{AB} - \frac{1}{L_{eq2}}\, v_1 - \frac{1}{L_{eqm}}\, v_2 - \frac{1}{L_{eqm}} v_{CD} \tag{3.4}$$

$$\frac{d}{dt} i_2 = \frac{1}{L_{eqm}}\, v_{AB} - \frac{1}{L_{eqm}}\, v_1 - \frac{1}{L_{eq1}} v_2 - \frac{1}{L_{eq1}} v_{CD} \tag{3.5}$$

KCL is applied to nodes in Fig. 3.2 to get,

$$i_1(t) = C_1 \frac{d}{dt} v_1(t) \tag{3.6}$$

$$i_2(t) = C_2 \frac{d}{dt} v_2(t) \tag{3.7}$$

$$i_{rect}(t) = |i_2(t)| = n \cdot |i_{prim}(t)| = \left(1 + \frac{R_c}{R_L}\right) \cdot C_f \frac{d}{dt} v_{Cf}(t) + \frac{v_{Cf}(t)}{R_L} \tag{3.8}$$

The output equation is,

$$v_o(t) = \frac{R_c\, R_L}{R_L + R_c} \cdot i_{rect}(t) + \frac{R_L}{R_L + R_c} \cdot v_{Cf}(t) \tag{3.9}$$

where,

$$L_{eq1} = \frac{n^2 L_{11}\, L_{22} - {L_m}^2}{n^2\, L_{11}}$$

$$L_{eq2} = \frac{n^2 L_{11}\, L_{22} - {L_m}^2}{n^2\, L_{22}}$$

$$L_{eqm} = \frac{n^2 L_{11}\, L_{22} - {L_m}^2}{n\, L_m}$$

These equations represent the nonlinear IPT system shown in Fig. 3.1. This is the exact non-linear state-space model containing both linear and nonlinear terms.

3.2.2 Harmonic Approximation

Eqs. (1) – (9) contain both linear and non-linear terms. One of the assumption was that the resonant inductor currents (i_1 and i_2) and thus resonant capacitor voltages (v_1 and v_2) are almost sinusoidal during steady-state operation. So, these quantities can be decomposed into their sine terms and cosine terms. Following are the equations for these variables and their derivative.

Let,

$$x = x_s \cdot \sin(\omega_s t) + x_c \cdot \cos(\omega_s t) \tag{3.10}$$

Where, x refers to the variables i_1, i_2, v_1 and v_2. There are derivatives of these variables in the equations (3.1) – (3.9). The derivative of x is,

$$\frac{d}{dt}x = \left(\frac{d}{dt}x_s - \omega_s \cdot x_c\right).\sin(\omega_s t) + \left(\frac{d}{dt}x_c + \omega_s \cdot x_s\right).\cos(\omega_s t) \tag{3.11}$$

With this approximation, all the linear terms in (3.11) – (3.16) can be represented by some sine and cosine terms. This is called harmonic approximation.

3.2.3 Extended Describing Functions

Describing functions will approximate the non-linear terms and the dc terms in equations (3.1) - (3.9). Applying Fourier series expansion to these terms can derive these functions. The three non-linear terms in these equations are the inverter output voltage (v_{AB}), the rectifier input voltage (v_{CD}) and the rectifier output dc current (I_{rect}).

The inverter generates the quasi-square voltage, v_{AB}, across its output. This voltage has an infinite number of harmonics as shown in equation 2.1. The resonant network is tuned to the resonant frequency that allows only the fundamental frequency and suppresses all the higher harmonics. So, the higher order harmonics in v_{AB} can be neglected without introducing

considerable error. The phase angle of v_{AB} is assumed to be the reference. So, this voltage can be represented by a pure sine. So,

$$v_{AB} = v_{AB\_S} \cdot \sin(\omega_s t) + v_{AB_C} \cdot \cos(\omega_s t) = \frac{4\, m\, v_g}{\pi} \sin\left(\frac{\pi}{2}\, d\right) \cdot \sin(\omega_s t) = v_e \cdot \sin(\omega_s t) \tag{3.12}$$

Where,

$$m = \begin{cases} 1 & for\ Full - Bridge\ Converter \\ 0.5 & for\ Half - Bridge\ Converter \end{cases}$$

The voltage across the input of the rectifying diodes, v_{CD}, depends on the direction of the rectifier input current, i_2. If i_2 is positive, this voltage is $+v_o$, and if i_2 is negative, this voltage is $-v_o$. So, v_{CD} is a square wave like v_{AB}. However, unlike v_{AB}, this voltage has both the sine and the cosine terms as it has some phase difference with respect to v_{AB} as can be seen in Figs. 2.5, 2.14, 2.15. The Fourier series analysis of this square-shaped voltage shows that it has an infinite number of odd harmonic components. Because all the higher harmonics can be neglected as the resonant network is tuned to fundamental harmonic, this voltage can be represented by the following expression,

$$v_{CD} = sign(i_2) \cdot v_o$$

$$v_{CD} = \frac{4}{\pi} \frac{i_{2s} \cdot v_{Cf}}{i_{pk}} \cdot \sin(\omega_s t) + \frac{4}{\pi} \frac{i_{2c} \cdot v_{Cf}}{i_{pk}} \cdot \cos(\omega_s t) \tag{3.13}$$

The rectifier output dc current is a function of rectifier input ac current. The averaged output rectified dc current is given by the following expression,

$$i_{rect} = |i_2| = \frac{2}{\pi}\, i_{pk} \tag{3.14}$$

where,

$$i_{pk}{}^2 = (i_{2s})^2 + (i_{2c})^2 \tag{3.15}$$

Eqs. (3.12) - (3.15) can be substituted in (3.1) – (3.9) for the nonlinear terms.

3.2.4 Harmonic Balance

Eqs. (3.1) - (3.9) can be re-written by replacing the linear terms by their sinusoidal approximations and the non-linear terms by their describing functions. The resulting equations will only have sine terms, cosine terms and dc terms. These terms can be collected into a separate set of equations.

The sine terms are:

$$\frac{d}{dt} i_{1s} = \frac{v_e}{L_{eq2}} - \frac{v_{1s}}{L_{eq2}} - \frac{v_{2s}}{L_{eqm}} + \omega_s \cdot i_{1c} - \frac{4}{\pi L_{eqm}} \frac{i_{2s} \cdot v_{Cf}}{i_{pk}} \tag{3.16}$$

$$\frac{d}{dt} i_{2s} = \frac{v_e}{L_{eqm}} - \frac{v_{1s}}{L_{eqm}} - \frac{v_{2s}}{L_{eq1}} + \omega_s \cdot i_{2c} - \frac{4}{\pi L_{eq1}} \frac{i_{2s} \cdot v_{Cf}}{i_{pk}} \tag{3.17}$$

$$\frac{d}{dt} v_{1s} = \frac{i_{1s}}{C_1} + \omega_s \cdot v_{1c} \tag{3.18}$$

$$\frac{d}{dt} v_{2s} = \frac{i_{2s}}{C_2} + \omega_s \cdot v_{2c} \tag{3.19}$$

The cosine terms are:

$$\frac{d}{dt} i_{1c} = - \frac{v_{1c}}{L_{eq2}} - \frac{v_{2c}}{L_{eqm}} - \omega_s \cdot i_{1s} - \frac{4}{\pi L_{eqm}} \frac{i_{2c} \cdot v_{Cf}}{i_{pk}} \tag{3.20}$$

$$\frac{d}{dt} i_{2c} = - \frac{1}{L_{eqm}} v_{1c} - \frac{v_{2c}}{L_{eq1}} - \omega_s \cdot i_{2s} - \frac{4}{\pi L_{eq1}} \frac{i_{2c} \cdot v_{Cf}}{i_{pk}} \tag{3.21}$$

$$\frac{d}{dt} v_{1c} = \frac{i_{1c}}{C_1} - \omega_s \cdot v_{1s} \tag{3.22}$$

$$\frac{d}{dt} v_{2c} = \frac{i_{1c}}{C_2} - \omega_s \cdot v_{2s} \tag{3.23}$$

The dc terms are,

$$C_f \frac{d}{dt} v_{Cf} = \frac{2}{\pi} \cdot \frac{R_L}{R_L + R_c} i_{pk} - \frac{1}{R_L + R_c} \cdot v_{Cf} \tag{3.24}$$

$$v_o = \frac{2}{\pi} \cdot \frac{R_c\, R_L}{R_L + R_c} \cdot i_{pk} + \frac{R_L}{R_L + R_c} \cdot v_{Cf} \tag{3.25}$$

These non-linear equations represent the simplified model of the system shown in Fig. 3.1.

3.2.5 Large-Signal Model

Once the simplified model is derived, the averaged model can be derived by applying averaging operator on both sides of the equations in equations (3.16) - (3.25).

The equations become,

$$\frac{d}{dt}\overline{i_{1s}} = \frac{\overline{v_e}}{L_{eq2}} - \frac{\overline{v_{1s}}}{L_{eq2}} - \frac{\overline{v_{2s}}}{L_{eqm}} + \overline{\omega_s} \cdot \overline{i_{1c}} - \frac{4}{\pi\, L_{eqm}} \frac{\overline{i_{2s}} \cdot \overline{v_{Cf}}}{\overline{i_{pk}}} \tag{3.26}$$

$$\frac{d}{dt}\overline{i_{2s}} = \frac{\overline{v_e}}{L_{eqm}} - \frac{\overline{v_{1s}}}{L_{eqm}} - \frac{\overline{v_{2s}}}{L_{eq1}} + \overline{\omega_s} \cdot \overline{i_{2c}} - \frac{4}{\pi\, L_{eq1}} \frac{\overline{i_{2s}} \cdot \overline{v_{Cf}}}{\overline{i_{pk}}} \tag{3.27}$$

$$\frac{d}{dt}\overline{v_{1s}} = \frac{\overline{i_{1s}}}{C_1} + \omega_s \cdot \overline{v_{1c}} \tag{3.28}$$

$$\frac{d}{dt}\overline{v_{2s}} = \frac{\overline{i_{2s}}}{C_2} + \omega_s \cdot \overline{v_{2c}} \tag{3.29}$$

$$\frac{d}{dt}\overline{i_{1c}} = -\frac{\overline{v_{1c}}}{L_{eq2}} - \frac{\overline{v_{2c}}}{L_{eqm}} - \overline{\omega_s} \cdot \overline{i_{1s}} - \frac{4}{\pi\, L_{eqm}} \frac{\overline{i_{2c}} \cdot \overline{v_{Cf}}}{\overline{i_{pk}}} \tag{3.30}$$

$$\frac{d}{dt}\overline{i_{2c}} = -\frac{\overline{v_{1c}}}{L_{eqm}} - \frac{\overline{v_{2c}}}{L_{eq1}} - \overline{\omega_s} \cdot \overline{i_{2s}} - \frac{4}{\pi\, L_{eq1}} \frac{\overline{i_{2c}} \cdot \overline{v_{Cf}}}{\overline{i_{pk}}} \tag{3.31}$$

$$\frac{d}{dt}\overline{v_{1c}} = \frac{\overline{i_{1c}}}{C_1} - \overline{\omega_s} \cdot \overline{v_{1s}} \tag{3.32}$$

$$\frac{d}{dt}\overline{v_{2c}} = \frac{\overline{i_{2c}}}{C_2} - \overline{\omega_s} \cdot \overline{v_{2s}} \tag{3.33}$$

$$\frac{d}{dt}\overline{v_{Cf}} = \frac{2R_L}{\pi C_f (R_L + R_c)}\overline{i_{pk}} - \frac{1}{C_f (R_L + R_c)}\overline{v_{Cf}} \tag{3.34}$$

$$\overline{v_o} = \frac{2}{\pi} \cdot \frac{R_c\, R_L}{R_L + R_c} \cdot \overline{i_{pk}} + \frac{R_L}{R_L + R_c} \cdot \overline{v_{Cf}} \tag{3.35}$$

These equations, (3.26) – (3.35), represent the non-linear averaged model, also known as the large-signal model, of the converter in Fig. 3.1. This model represents the envelope of the currents and voltages in the converter under both steady-state and transient conditions.

3.2.6 Steady-State Model and Linearized Small-Signal Model

Equations (3.26) – (3.35) represent the large-signal model. Large-signal model contains both the steady-state operating point and the small-signal model. The steady-state solution can be obtained by equating the derivative terms in the large-signal model to zero since the variables do not change during the steady-state condition.

In this circuit, the steady-state operating point is determined by [V_{DC}, F_{sw}, D, I_o, R_L]. Perturbing the variables around the steady-state operating point can derive the small-signal model. Thus, each averaged term can be written as the sum of steady-state value and a small perturbation around it.

$$\bar{x} = X + \hat{x} \tag{3.36}$$

In the resonant converters, the poles and zeros are functions of normalized switching frequency. So, for w_o being the primary series resonant frequency:

$$\overline{\omega_s} = \Omega_s + \omega_o\, \widehat{\omega_n} \tag{3.37}$$

To obtain the linearized small-signal model, the non-linear terms in equations (3.26) - (3.35) should be linearized around some steady-state operating point. Taylor's series expansion can be used to linearize these terms.

$$\frac{\overline{i_{2s}} \cdot \overline{v_{Cf}}}{\overline{i_{pk}}} = \frac{I_{2s}\, V_{Cf}}{I_{pk}} + \frac{I_{2s}}{I_{pk}} \hat{v}_{cf} + \frac{{I_{2c}}^2 V_{Cf}}{{I_{pk}}^3} \hat{\imath}_{2s} - \frac{I_{2s}\, I_{2c} V_{Cf}}{{I_{pk}}^3} \hat{\imath}_{2c} \tag{3.38}$$

$$\frac{\overline{i_{2c}} \cdot \overline{v_{Cf}}}{\overline{i_{pk}}} = \frac{I_{2c}\, V_{Cf}}{I_{pk}} + \frac{I_{2c}}{I_{pk}} \hat{v}_{cf} - \frac{I_{2s}\, I_{2c} V_{Cf}}{{I_{pk}}^3} \hat{\imath}_{2s} + \frac{{I_{2c}}^2 V_{Cf}}{{I_{pk}}^3} \hat{\imath}_{2c} \tag{3.39}$$

And,

$$\overline{\widehat{\iota_{pk}}} = I_{pk} + \frac{I_{2s}}{I_{pk}}\widehat{\iota_{2s}} + \frac{I_{2c}}{I_{pk}}\widehat{\iota_{2c}} \tag{3.40}$$

$$\widehat{v_e} = \frac{4}{\pi} \cdot \sin\left(\frac{\pi}{2} D\right) \hat{v}_g + 2 \cdot V_g \cdot \cos\left(\frac{\pi}{2} D\right) \hat{d} \tag{3.41}$$

After substituting (3.37) – (3.41) in equations (3.26) – (3.35), the steady-state and the small-signal parts can be separated, and can be written in the matrix form. The steady-state equations in matrix form become:

$$B_{st} = A_{st} \cdot X_{st} \tag{3.42}$$

$$V_o = V_{Cf} = \frac{2}{\pi} I_{pk} R_L \tag{3.43}$$

Where,

$$B_{st} = [V_e \quad V_e \quad 0 \quad 0 \quad 0 \quad 0 \quad 0 \quad 0]^T$$

$$X_{st} = [V_{1s} \quad V_{2s} \quad I_{1s} \quad I_{2s} \quad V_{1c} \quad V_{2c} \quad I_{1c} \quad I_{2c}]^T$$

$$A_{st} = \begin{bmatrix} 1 & \frac{L_{eq2}}{L_{eqm}} & 0 & \frac{L_{eq2} R_e}{L_{eqm}} & 0 & 0 & -\Omega_s L_{eq2} & 0 \\ 1 & \frac{L_{eqm}}{L_{eq1}} & 0 & \frac{L_{eqm} R_e}{L_{eq1}} & 0 & 0 & 0 & -\Omega_s L_{eqm} \\ 0 & 0 & 1 & 0 & \Omega_s C_1 & 0 & 0 & 0 \\ 0 & 0 & 0 & 1 & 0 & \Omega_s C_2 & 0 & 0 \\ 0 & 0 & \Omega_s L_{eq2} & 0 & 1 & \frac{L_{eq2}}{L_{eqm}} & 0 & \frac{L_{eq2} R_e}{L_{eqm}} \\ 0 & 0 & 0 & \Omega_s L_{eqm} & 1 & \frac{L_{eqm}}{L_{eq1}} & 0 & \frac{L_{eqm} R_e}{L_{eq1}} \\ -\Omega_s C_1 & 0 & 0 & 0 & 0 & 0 & 1 & 0 \\ 0 & -\Omega_s C_2 & 0 & 0 & 0 & 0 & 0 & 1 \end{bmatrix}$$

And,

$$I_{pk}{}^2 = (I_{2s})^2 + (I_{2c})^2$$

$$V_e = \frac{4}{\pi} \cdot V_g \cdot \sin\left(\frac{\pi}{2} D\right)$$

$$R_e = \frac{8}{\pi^2} R_L$$

$$0 \leq D \leq 1$$

The output voltage versus operating switching frequency curve and the output current versus the operating switching frequency curve for IPT system can be plotted using (3.42) and (3.43).

The linearized small-signal model in matrix form can be described as:

$$\frac{d}{dt}\hat{x} = A \cdot \hat{x} + B \cdot \hat{u} \tag{3.44}$$

$$\hat{y} = C \cdot \hat{x} \tag{3.45}$$

where,

$$A = \begin{bmatrix} 0 & \Omega_s & -K_1 & K_2 & \frac{-1}{L_{eq2}} & 0 & \frac{-1}{L_{eqm}} & 0 & -K_3 \\ -\Omega_s & 0 & K_{11} & -K_{12} & 0 & \frac{-1}{L_{eq2}} & 0 & \frac{-1}{L_{eqm}} & -K_{13} \\ 0 & 0 & -K_6 & \Omega_s + K_7 & \frac{-1}{L_{eqm}} & 0 & \frac{-1}{L_{eq1}} & 0 & -K_8 \\ 0 & 0 & -\Omega_s + K_{14} & -K_{15} & 0 & \frac{-1}{L_{eqm}} & 0 & \frac{-1}{L_{eq1}} & -K_{16} \\ \frac{1}{C_1} & 0 & 0 & 0 & 0 & \Omega_s & 0 & 0 & 0 \\ 0 & \frac{1}{C_1} & 0 & 0 & -\Omega_s & 0 & 0 & 0 & 0 \\ 0 & 0 & \frac{1}{C_2} & 0 & 0 & 0 & 0 & \Omega_s & 0 \\ 0 & 0 & 0 & \frac{1}{C_2} & 0 & 0 & -\Omega_s & 0 & 0 \\ 0 & 0 & K_{17} & K_{18} & 0 & 0 & 0 & 0 & -K_{19} \end{bmatrix}$$

$$B = \begin{bmatrix} \omega_o I_{1c} & K_4 & K_5 \\ -\omega_o I_{1s} & 0 & 0 \\ \omega_o I_{2c} & K_9 & K_{10} \\ -\omega_o I_{2s} & 0 & 0 \\ \omega_o V_{1c} & 0 & 0 \\ -\omega_o V_{1s} & 0 & 0 \\ \omega_o V_{2c} & 0 & 0 \\ -\omega_o V_{2s} & 0 & 0 \\ 0 & 0 & 0 \end{bmatrix}$$

$$C = [0 \quad 0 \quad K_{20} \quad K_{21} \quad 0 \quad 0 \quad 0 \quad 0 \quad K_{22}]$$

$$\hat{x} = [\widehat{i_{1s}} \quad \widehat{i_{1c}} \quad \widehat{i_{2s}} \quad \widehat{i_{2c}} \quad \widehat{v_{1s}} \quad \widehat{v_{1c}} \quad \widehat{v_{2s}} \quad \widehat{v_{2c}} \quad \widehat{v_{Cf}}]^T$$

$$\hat{u} = \left[\widehat{\omega_n} \quad \widehat{v_g} \quad \hat{d}\right]^T$$

$$\hat{y} = \widehat{v_o}$$

The variables $K_1 \sim K_{22}$ are listed in appendix. Equations (3.44) and (3.45) can be used to find the plant transfer functions,

$$G_p(s) = C \cdot [sI - A]^{-1} \cdot B = [G_{vf}(s) \quad G_{vvg}(s) \quad G_{vd}(s)] \tag{3.46}$$

The small-signal model in (3.44) – (3.45) includes both the frequency control and the phase-shift control. With the phase-shift control, the ZVS range in the primary side switches depends on the series leakage inductance. In this topology, the series inductance is part of the resonant network, and thus with the phase-shift control, the ZVS cannot be ensured at all load and line conditions. With the frequency control approach, ZVS can be maintained at all load and line conditions as long as the primary-side current lags behind the primary-side bridge voltage.

3.3 Experimental Verification with an IPT system

In Section 3.2, the large-signal model, the steady-state operating point and the small-signal model for a CLLLC-type resonant converter and a Series-Series compensated IPT systems are derived. In this Section, these three models will be verified experimentally.

The designed loosely coupled transformer for the IPT system, with both sides identical, is shown in Fig. 3.1. Each side consists of 28 turns coil and a special ferrite core. In order to reduce the weight and cost of the core, 12 small ferrite bars are used as a core instead of one solid ferrite.

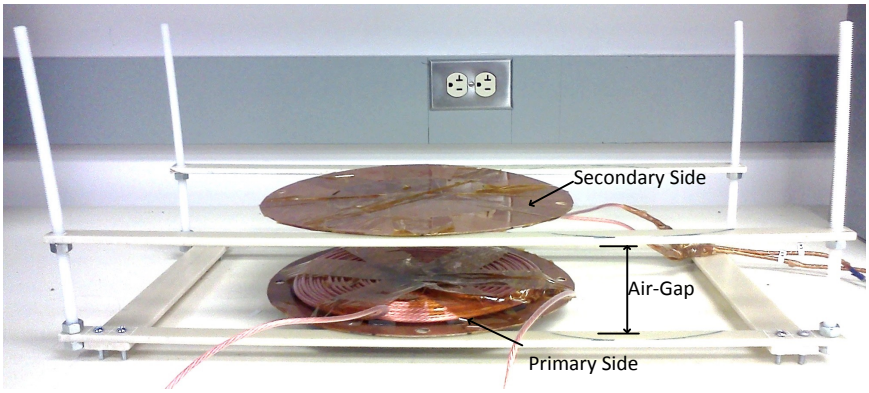

Fig. 3.2. Loosely coupled transformer built in lab.

The circuit parameters for the IPT system with air-gap of 7 cm are listed in Table 3.I.

Table 3.1 Circuit parameters for the IPT system

Quantity	Symbol	Value
DC bus voltage	V_{DC}	400 V
Battery voltage	V_{Batt}	250 V ~ 450 V
Battery charging current	I_{Batt}	8 A ~ 10 A
Equivalent load resistance	R_L	25Ω ~ 55Ω
Primary-side leakage inductance	L_1	84.31 µH
Secondary-side leakage inductance	L_2	89.55 µH
Magnetizing inductance	L_m	41.37 µH
Transformer turns ratio	n	1
Transformer air-gap	l_g	7 cm
Ferrite bar dimensions		7.9 cm x 2.35 cm x 0.4 cm
Primary-side resonant capacitance	C_1	10 nF
Secondary-side resonant capacitance	C_2	10 nF
Output filter capacitance	C_f	4.7 µF
ESR for output capacitance	Rc	1 mΩ

3.3.1 Verification of Steady-State Model

The steady-state model derived in Section 3.2 can predict the voltage gain of the IPT system for any load and line conditions. Gain curves are very important for resonant converters since the design of these converters can be verified using these curves. These curves give information about the operating frequency range and maximum gain of the converter. Either varying the operating switching frequency or the duty cycle of the active switches can change the output

current and the output voltage in resonant converters. For a frequency control, the duty cycle and the input voltage of the converter are kept constant while the operating switching frequency is varied to change the output current and the output voltage. Similarly, for a phase-shift control the operating switching frequency and the input voltage are kept constant, and the duty cycle of the switches is varied to change the output current and voltage. Eq. (3.42) and (3.43) can be used to plot the steady-state gain curves for IPT system versus either switching frequency or duty cycle.

To verify the steady-state model derived in Section 3.2, the predicted gain curves from the derived model are compared with the experimentally measured gain curves under different load conditions using an oscilloscope. Solid lines in Fig. 3.3 represent the curves from the derived model while the dashed lines represent the experimental gain curves. The predicted steady-state model is found to be in a very close agreement with the experimental data.

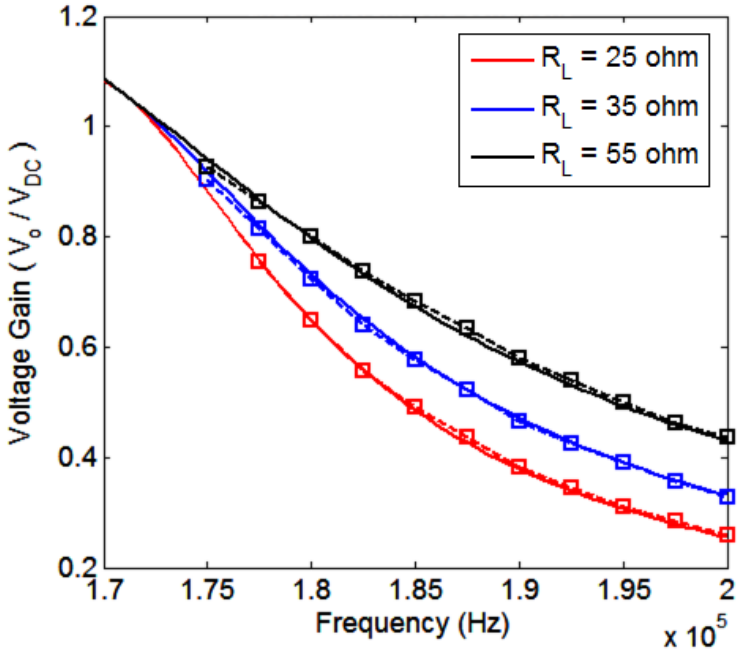

Fig. 3.3. Voltage gain curves for IPT system under different load conditions. Solid lines represent the derived model while the dashed lines represent the measured experimental data.

3.3.2 Verification of Large-Signal Model

The large-signal model derived in Section 3.2 can predict the envelope of the current and the voltage waveforms in the converter. To verify this model, a step change is applied in the switching frequency in the IPT system for a resistive load of 25Ω for converter operating in an open loop. Figs. 3.4 – 3.9 show the predicted large-signal models (envelopes) and the measured

waveforms for the transformer primary side current, secondary side current, and the converter output voltage under a step change of the frequency from 180 to 200 kHz and from 200 to 180 kHz. It can be seen that the model can predict the envelope very well during the steady-state conditions as well as during the transient conditions.

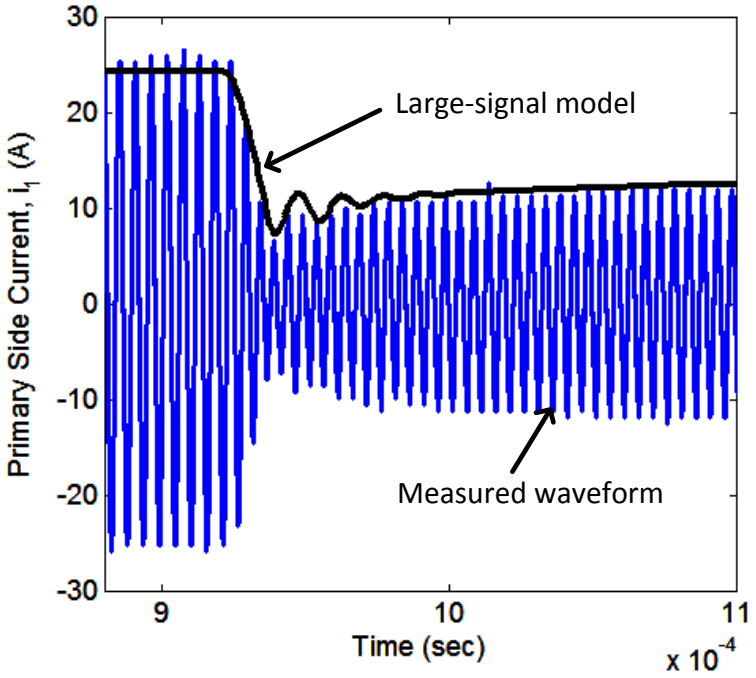

Fig. 3.4. Transformer primary side current when a step increase in switching frequency from 180 kHz to 200 kHz is applied.

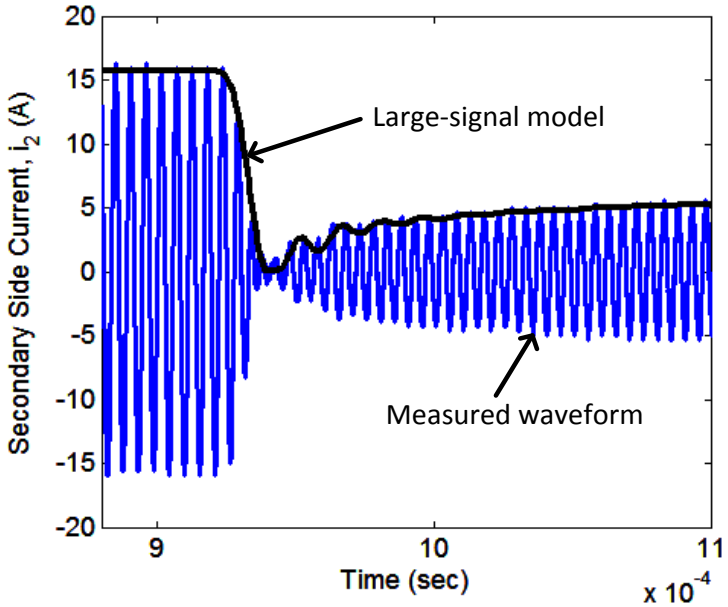

Fig. 3.5. Transformer secondary side current when a step increase in switching frequency from 180 kHz to 200 kHz is applied.

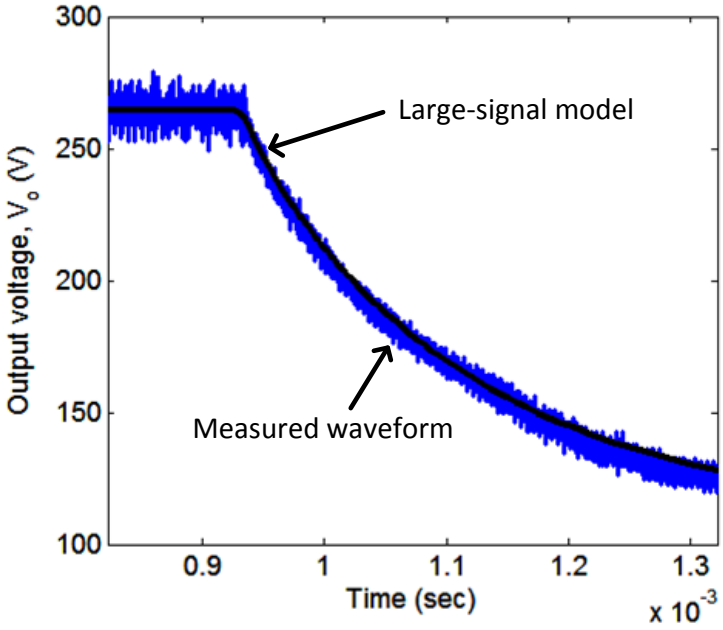

Fig. 3.6. Converter output voltage when a step increase in switching frequency from 180 kHz to 200 kHz is applied.

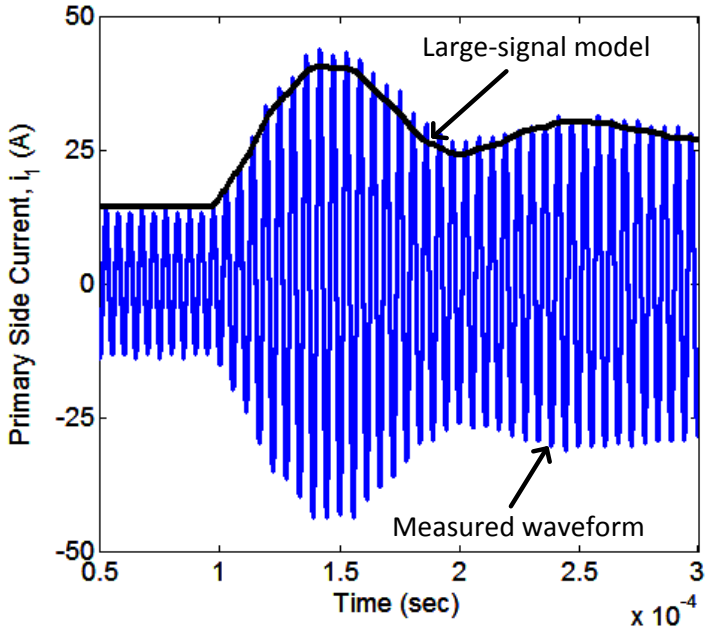

Fig. 3.7. Transformer primary side current when a step decrease in switching frequency from 200 kHz to 180 kHz is applied.

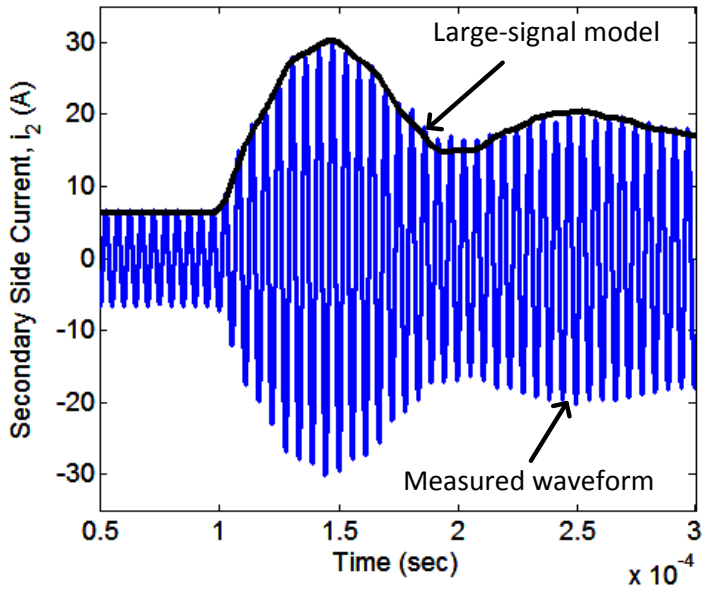

Fig. 3.8. Transformer secondary side current when a step decrease in switching frequency from 200 kHz to 180 kHz is applied.

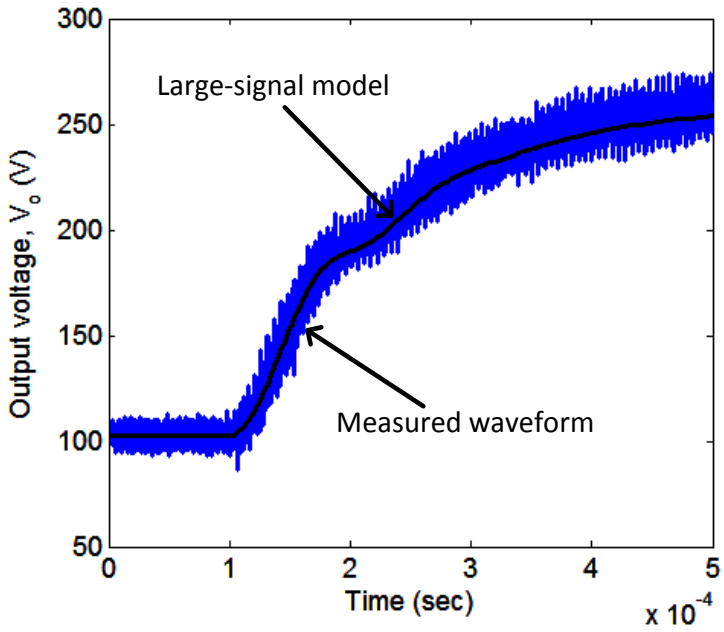

Fig. 3.9. Converter output voltage when a step decrease in switching frequency from 200 kHz to 180 kHz is applied.

3.3.3 Verification of Small-Signal Model

The small-signal model contains information about converter dynamics. Such a model can be used to find various transfer functions. These transfer functions can be used to close the loop for load and line regulations. In the battery charging application the converter should be able to

operate in both constant current mode and constant voltage mode. In this resonant converter, the control signal is the operating switching frequency, with the output voltage and current varied by adjusting this frequency. This makes it important that the derived small-signal model to be able to predict the control-to-output current transfer function, $G_{if}(s)$, and control-to-output voltage transfer function, $G_{vf}(s)$.

Some circuit simulation softwares, like SIMPLIS, can do ac analysis of resonant converters. SIMPLIS software can be used to plot the open loop control-to-output voltage transfer function for a Series-Series compensated IPT system. To validate the derived small-signal model, the open loop bode plot predicted by the small-signal model derived in Section 3.2 is compared with the open loop bode plot by SIMPLIS. Fig. 3.10 and Fig. 3.11 show the bode plots for control-to-output voltage transfer function under different load conditions. The derived small-signal model can predict the Bode plot by SIMPLIS very closely, which validates the derived model.

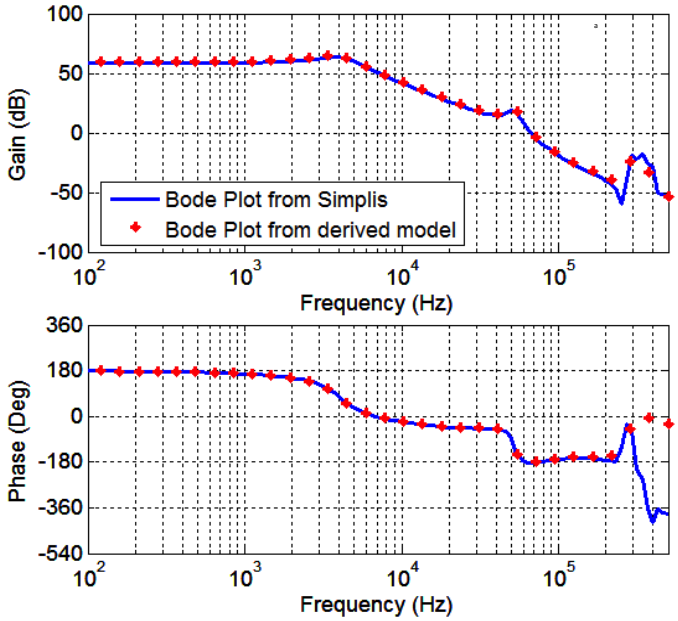

Fig. 3.10. IPT system control-to-output voltage transfer function at R_L = 55 Ω and f_s/f_o = 1.03.

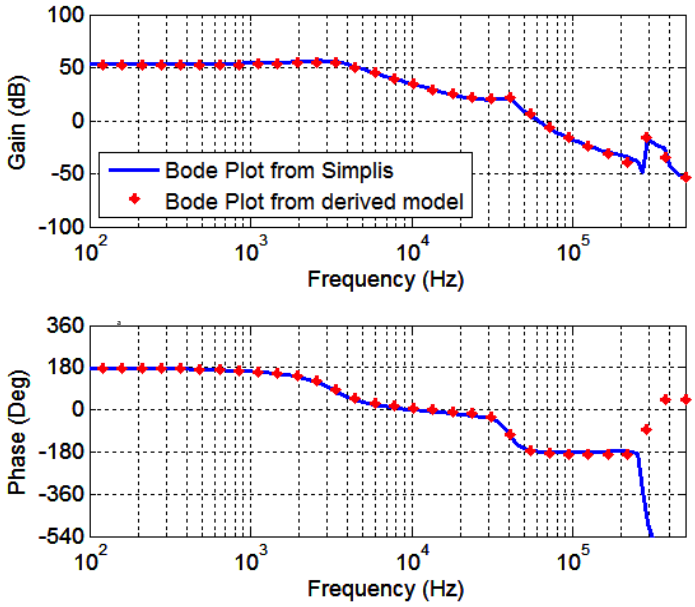

Fig. 3.11. IPT system control-to-output voltage transfer function at R_L = 55 Ω and f_s/f_o = 0.97.

3.3.4 Verification of the Small-Signal Model for the resonant converter

In Section 3.3.3, it was shown that the equations (3.44) and (3.45) can predict the open-loop bode for the IPT system. In this section, these equations will be used to predict the open-loop bode-plots in the CLLLC-type resonant converter.

Fig. 3.12 shows the voltage gain for the CLLLC-type resonant converter versus the operating switching frequency curve for the converter with the load resistance, R_L, equal to 45 Ω. The gain of the converter is unity at the primary side series resonant frequency, f_{ser}, of 100 kHz. The gain of the converter is more than unity for frequencies lower than f_{ser}, and the gain is less than unity for frequencies greater than f_{ser}. The rest of the circuit parameters are listed below,

Resonant Inductances (L_1, L_2)	Magnetizing Inductance (L_m)	Primary-Side Resonant Capacitor (C_1)	Secondary-Side Resonant Capacitor (C_2)	Transformer Turns Ratio (n)	Filter Capacitor (C_f)
20 µH	100 µH	136 nF	200 nF	1	30 µF

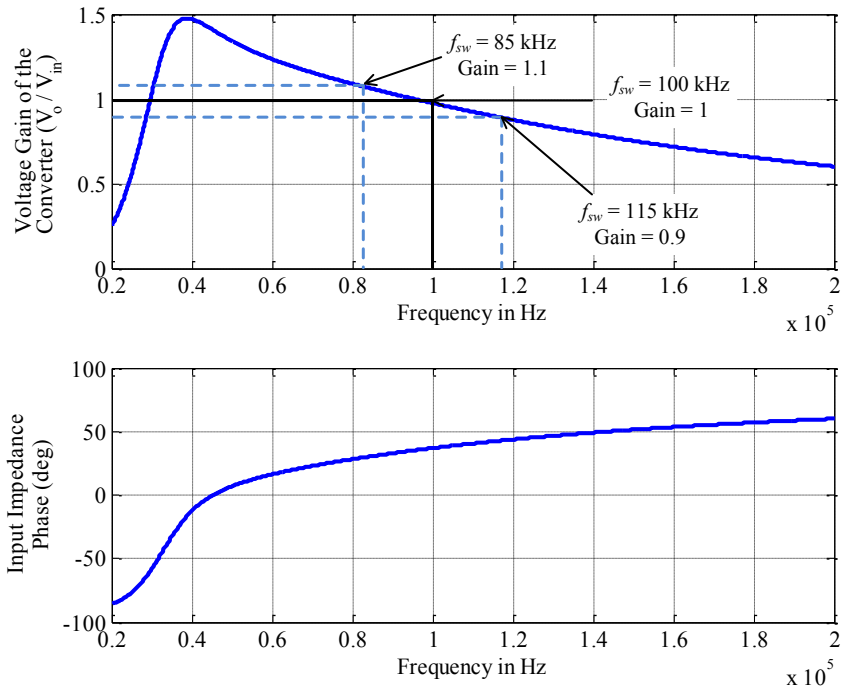

Fig. 3.12. The voltage gain versus the operating switching frequency curve for the resonant converter in Fig. 3.1.

To validate the model in (3.44) and (3.45), the open-loop bode-plot by SIMPLIS will be compared with the open-loop plot by the small-signal model in (3.44) and (3.45). Figs. 3.13-3.15 show the bode-plots for the control-to-output voltage transfer function at different operating points.

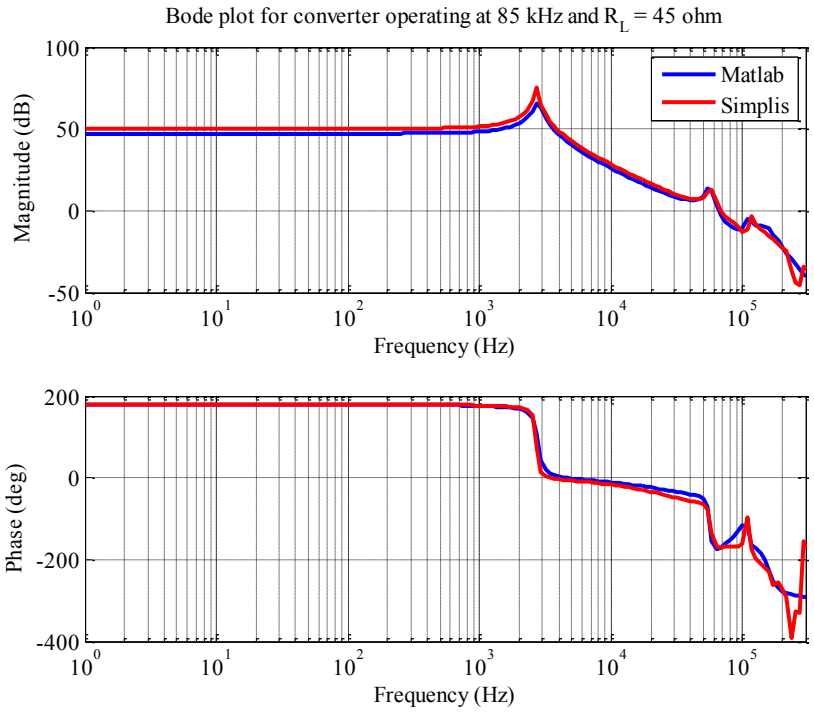

Fig. 3.13. Open-loop control-to-output voltage transfer function, $G_{vf}(s)$, for the converter operating in the boost mode at a switching frequency of 85 kHz.

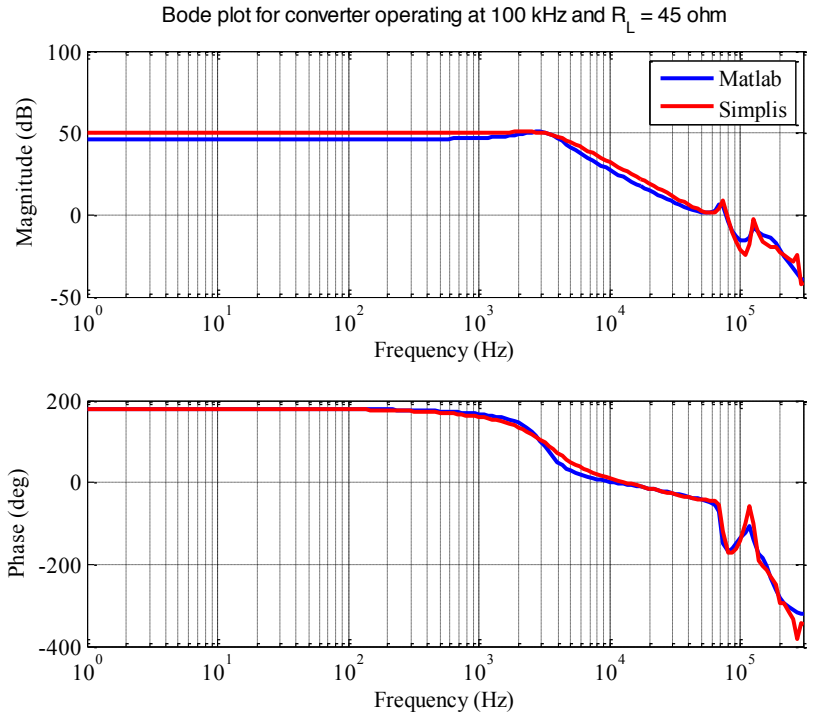

Fig. 3.14. Open-loop control-to-output voltage transfer function, $G_{vf}(s)$, for the converter operating at a unity gain at a switching frequency of 100 kHz.

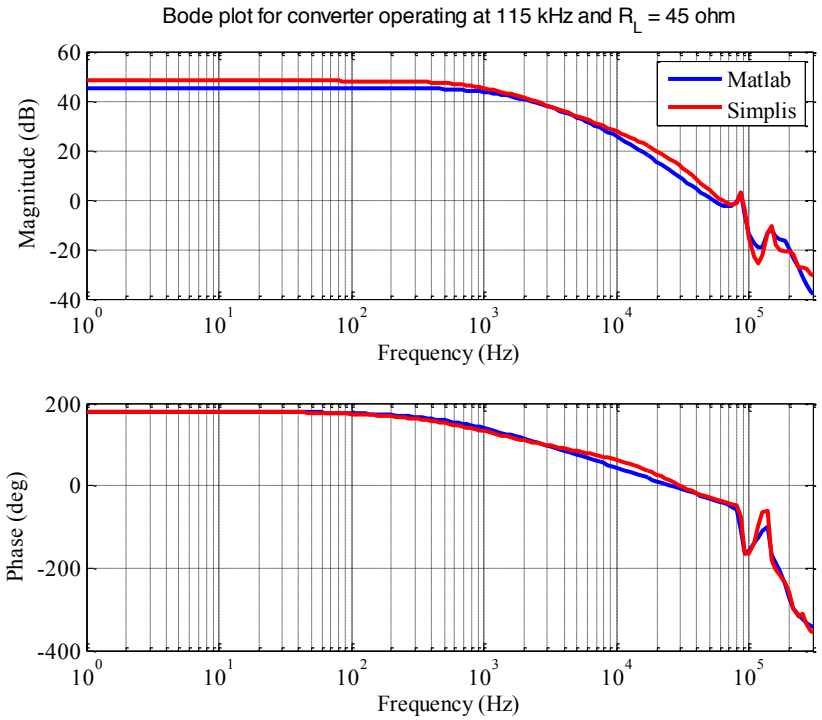

Fig. 3.15. Open-loop control-to-output voltage transfer function, $G_{vf}(s)$, for the converter operating in the buck mode at a switching frequency of 115 kHz.

Figs. 3.13-3.15 show that the small-signal model in (3.44) and (3.45) can predict the bode-plot by SIMPLIS very closely, which validates the model. It can be seen that the gain at low frequencies differs by few dBs. The reason is that the currents, i_1 and i_2, are assumed to be pure sinusoids, while in the actual circuit, they are not.

3.4 Conclusions

In this chapter, a detailed modeling procedure based on extended describing functions was presented for a CLLLC-type resonant converter and a Series-Series compensated IPT system. With a T-equivalent circuit utilized to model the loosely coupled transformer in the IPT system, the equivalent circuit diagram for the IPT system becomes the same as the equivalent circuit diagram of the CLLLC-type resonant converter. And, this modeling procedure is valid for any other resonant converter with the same topology.

First, the averaged large-signal model was derived. This model can predict the envelope of the switching waveforms during the steady-state operating point as well as during the transients. This model was verified experimentally by comparing the measured switching waveforms with the envelope predicted by the large-signaled model.

Then, the steady-state model was derived. This model can predict the voltage gain curve and the current gain curve for the converter for any load and line conditions. This model was verified experimentally by comparing the voltage gain curve from experimentally measured data with the predicted gain curves from the derived model.

And finally, the continuous-time small-signal model was derived in a closed form. This model includes both the frequency and the phase-shift control. This model can be used to derive all the transfer functions of the converter. This model was verified by comparing the predicted bode plot for control-to-output voltage transfer function with the bode plot for the same transfer function generated by SIMPLIS.

Chapter 4 Controller Design for the Bidirectional DC-DC Resonant Converter

4.1 Introduction

The dynamics analysis of any converter is necessary to design the control loop. The bandwidth, phase margin and gain margin of the control loops should be properly designed to guarantee a robust system. During battery charging and discharging, the battery voltage changes that move the converter operating point, and thus the plant dynamics change. If the controller is not properly designed, the closed-loop system might be unstable at some operating points. So, it is very important to find the worst-case operating conditions for the controller design. If the controller is designed for this worst-case, it will guarantee a stable operation of the converter for the entire mode of operation.

In the *BCM*, the converter should be able to operate in both constant current mode and constant voltage mode. In the constant current mode, the battery is charged with a constant current. Once, the battery voltage reaches the reference voltage, the converter operates in the constant voltage mode and keep the battery voltage at the reference voltage. In the *RM*, the

converter operates only in the constant voltage mode, and keeps the DC bus voltage constant for a wide range of battery voltage.

The purpose of this chapter is to propose a controller design methodology for a *CLLLC*-type resonant converter for a wide input and a wide output voltage range. This converter has the same equivalent model as the Series-Series compensated Induction Power Transfer (IPT) system. So, the design methodology proposed here is applicable there as well.

4.2 Step-by-Step Procedure to Find the Worst-case Conditions for Controller Design

In this section, the small-signal model derived in (3.44) – (3.45) will be used to design the current loop controller and the voltage loop controller for a 3.5 kW bidirectional resonant converter designed in Section 2.3. The circuit parameters are listed in Table (4.I).

Table 4.1 Circuit parameters for the bidirectional resonant converter

DC bus voltage	V_{DC}	400 V
DC bus capacitance	C_{DC}	1.8 mF
Resonant Inductances	L_1 and L_2	20 μH
Magnetizing Inductances	L_m	100 μH
DC bus side resonant capacitor	C_1	136 nF
Battery side resonant capacitor	C_2	200 nF
Battery side filter capacitor	C_f	30 μF
Battery voltage range	V_{Batt}	250 V ~ 450 V

The first step in designing a controller would be to find the equivalent load resistance. Then, the operating switching frequency range needs to be determined. With this information, the worst-case for the controller can be determined. And then, the controller can be designed for this worst-case operating condition.

4.2.1 Output load resistance range

The first step in designing a controller is to find the equivalent load resistance, R_L, during the entire mode. The range of equivalent output resistance, R_L, depends upon the battery charging and discharging profile.

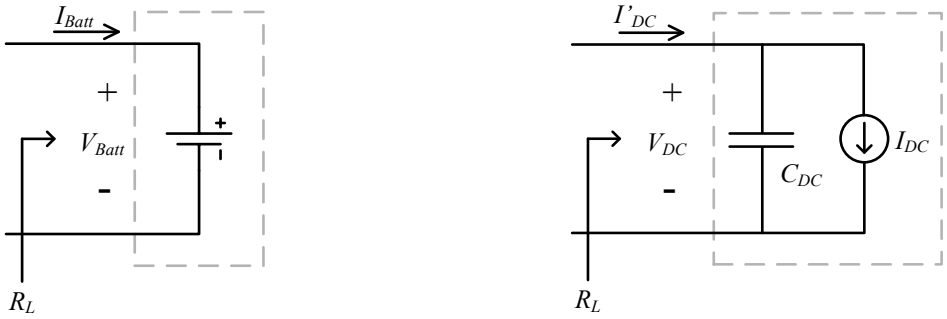

(a) R_L during the *BCM* (b) R_L during the *RM*

Fig. 4.1. Equivalent output load resistance for converter operating in the *BCM* and in the *RM*.

Fig. 4.1 shows the equivalent load resistance during the *BCM* and the *RM*. In the *BCM*,

$$R_L = \frac{V_{Batt}}{I_{Batt}} \tag{4.1}$$

In the *RM*,

$$R_L = \frac{{V_{DC}}^2}{P_o} = \frac{V_{DC}}{I_{DC}} \tag{4.2}$$

4.2.2 Operating Frequency range

To determine the operating frequency range, the output current and the output voltage at the steady-state are plotted against the converter operating switching frequency under different output load conditions using equations (3.42) – (3.43). One of the requirements for a PID controller is that the slope of the gain curves should not change sign under all load conditions. So, it is important to plot these gain curves under all load conditions, and check the slope of the curves. Plotting a 3-D plot (output current or voltage versus the operating switching frequency

versus R_L) over the entire operating switching frequency range and the output load resistance range can do this.

4.2.3 Determining the Worst-case Operating Conditions for Controller Design

As mentioned earlier, during the charging and discharging process, the battery voltage changes. This changes the converter operating point. The low-frequency gain and the zero-crossing of the open-loop bode-plot changes as the operating point changes. To find the worst-case, the open-loop bode-plot is plotted at all load resistances and operating switching frequencies.

4.3 Finding the Worst-Case Operating Conditions for the Current Loop Controller for Converter Operating in the BCM

The range of equivalent output resistance, R_L, depends upon the battery charging profile. The output charging current versus the battery voltage for the converter operating in the *BCM* is shown in Fig. 4.2. During the constant current mode, a constant current charges the output battery. The output current is limited to 10 A for the lower battery voltages. For higher battery voltages, the charging current is reduced to keep the output power at 3.5 kW.

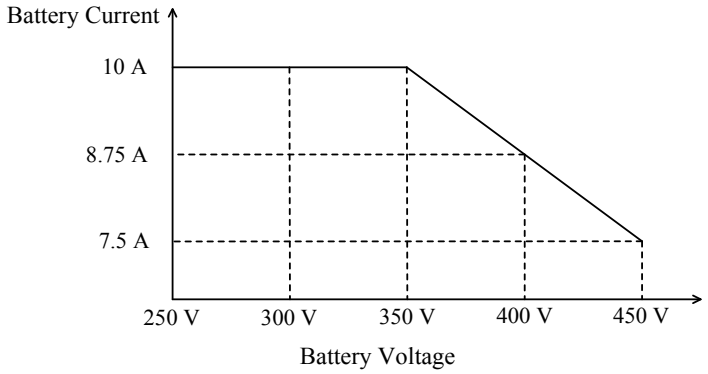

Fig. 4.2. Battery current versus the battery voltage for the converter operating in the *BCM*.

So, during the constant current mode,

$$R_{L\_I} = \frac{V_{Batt}}{I_{Batt}} = \frac{250\ V}{10\ A} \sim \frac{450\ V}{7.5\ A} = 25\ \Omega \sim 60\ \Omega \tag{4.3}$$

Under the nominal operating conditions, the battery voltage is 350 V and the charging current is 10 A. So, the equivalent output resistance under nominal operating condition is,

$$R_{L\_Inom} = \frac{V_{Batt\_nom}}{I_{Batt\_nom}} = \frac{350\ V}{10\ A} = 35\ \Omega \tag{4.4}$$

To get the operating frequency range, the output current under steady-state condition is plotted against the converter operating switching frequency under different load conditions. In Fig. 4.3, the steady-state output current versus the operating switching frequency is plotted for R_{L_Imin}, R_{L_Inom} and R_{L_Imax}. These curves give a good amount of information about the design of the converter, and the operating frequency range during the closed-loop operation. It can be seen that the operating switching frequency range for the converter operating in the *BCM* is,

$$f_{sw\_BCM} = 80\ kHz \sim 140\ kHz \tag{4.5}$$

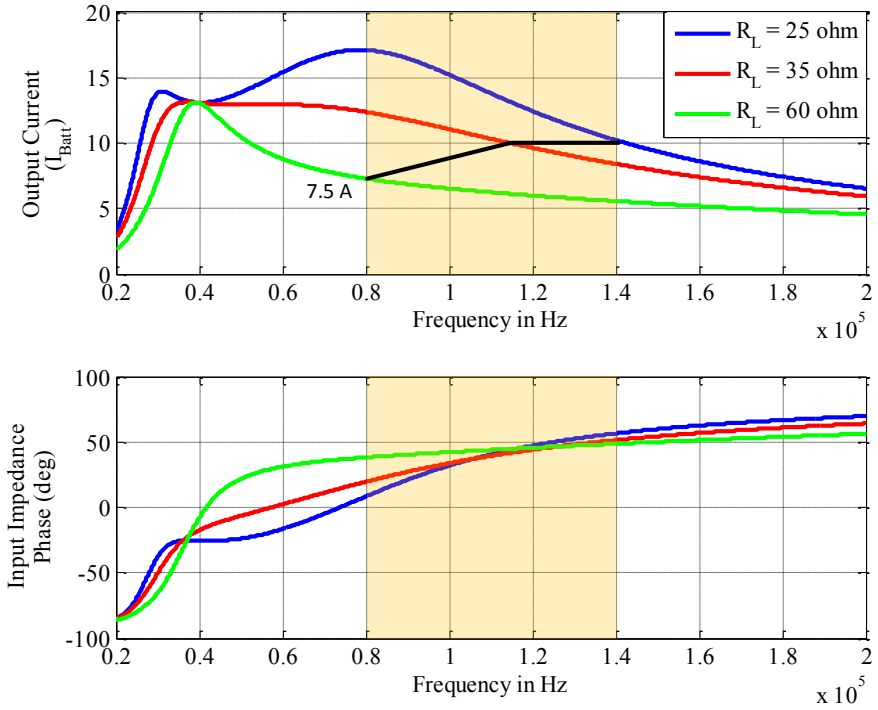

Fig. 4.3. Output current versus operating switching frequency under different load conditions for converter operating in the *BCM*.

The battery voltage versus the operating switching frequency for the whole range of load resistance is plotted in Fig. 4.4. The operating surface is enclosed by the yellow polygon. It can be seen that the enclosed surface is monotonically decreasing, so a PID controller can used to close the current loop.

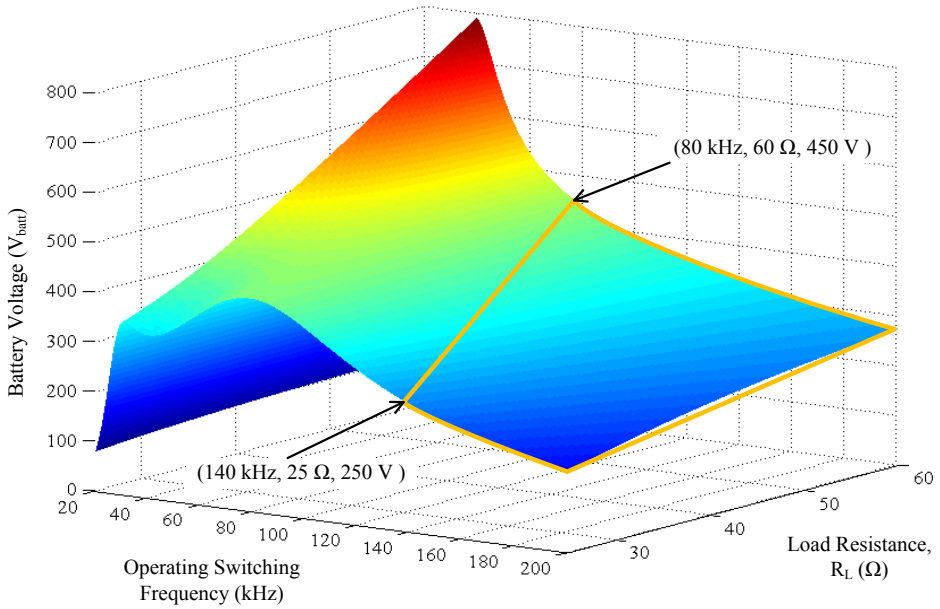

Fig. 4.4. Battery voltage versus the operating switching frequency under different load conditions for the converter operating in the *BCM*.

The next step is to find the worst-case conditions for the current loop controller design. Fig. 4.5 shows the open-loop control-to-output current, $G_{if}(s)$, for a load resistance of 60 Ω. The operating switching frequency is varied from 80 kHz to 200 kHz. It can be seen that the open-loop bode-plot zero-crossing frequency increases as the converter switching frequency decreases. For a switching frequency of 90 kHz, the open-loop bode-plot zero-crossing frequency is maximum. So, for a fixed load resistance, the worst-case occurs at 90 kHz.

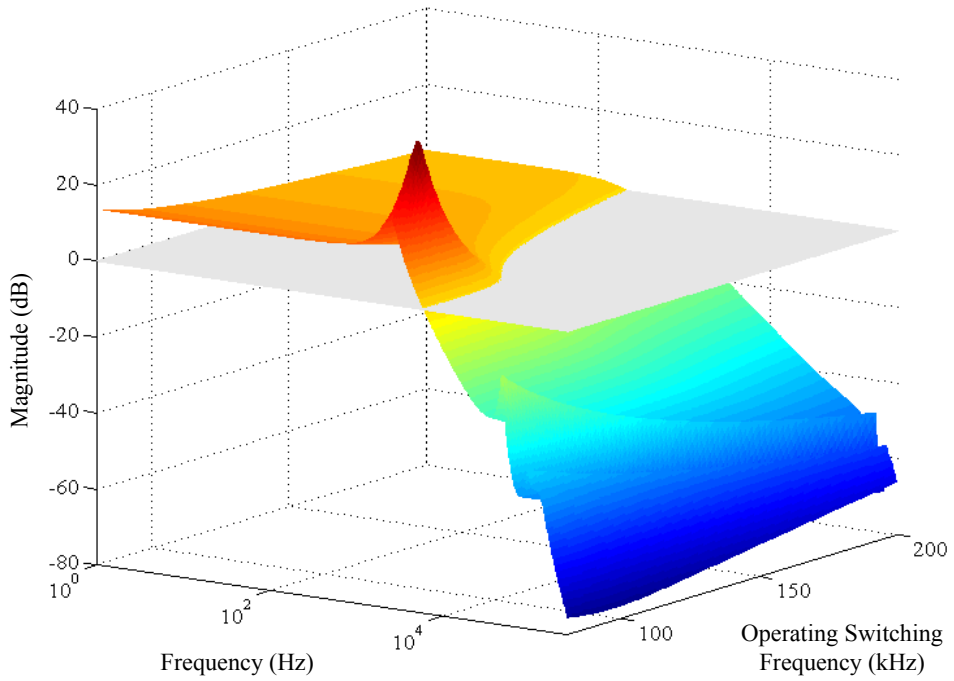

Fig. 4.5. Open-loop bode-plot for control-to-output current, $G_{if}(s)$, under different operating switching frequencies for the converter operating in the *BCM*.

Fig. 4.6 shows the open-loop control-to-output current, $G_{if}(s)$, for converter operating at a switching frequency of 90 kHz. The output load resistance is varied from 25 Ω to 60 Ω. It can be seen that the zero-crossing frequency of the open-loop bode-plot remains almost the same.

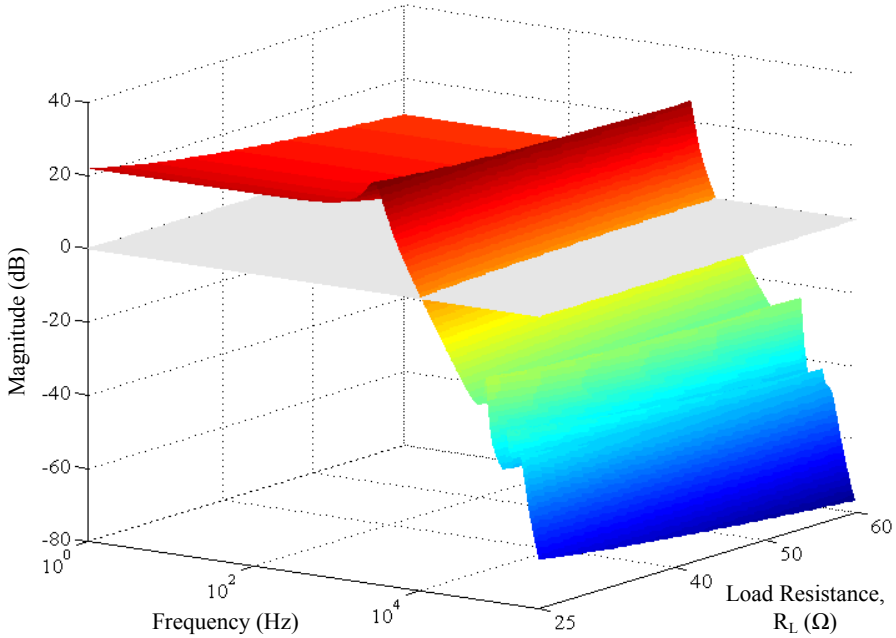

Fig. 4.6. Open-loop bode-plot for control-to-output current, $G_{if}(s)$, for the converter operating at switching frequency of 90 kHz under different load conditions.

Fig. 4.3 shows that the converter will operate at a switching frequency of 90 kHz only for an equivalent load resistance 35 Ω or more. So, the worst-case conditions for the current loop controller design are when the output load resistance is between 35 Ω and 60 Ω. This worst-case open-loop bode-plot for current loop controller is shown in Fig. 4.17.

4.4 Finding the Worst-Case Operating Conditions for the Voltage Loop Controller for Converter Operating in the BCM

In the constant voltage mode, the converter keeps the battery voltage constant at the reference voltage. In this mode, the charging current drops to a very small value. So, the equivalent output resistance, R_L, becomes very large.

In this example, the battery reference voltage is set to 450 V. So, if the minimum charging current is set to 100 mA, then during the constant voltage mode, the charging current drops from 7.5 A to 100 mA. So,

$$R_{L\_V} = \frac{V_{Batt}}{I_{Batt}} = 60\ \Omega \sim 4.5\ k\Omega \tag{4.6}$$

To determine the operating frequency range in the constant voltage mode, the steady-state output battery voltage versus the operating switching frequency curves are plotted for R_{L_Vmin} and at some larger load resistances using equations (3.42) – (3.43). Fig. 4.7 shows these curves.

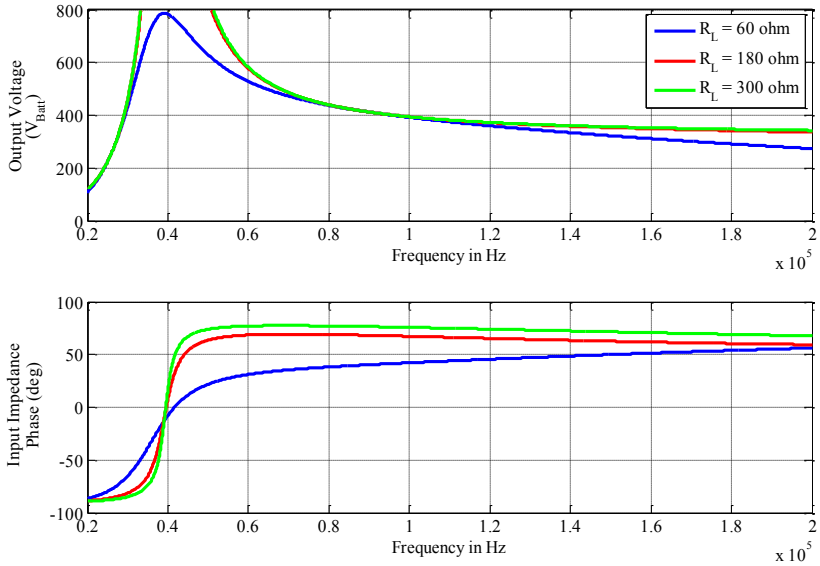

Fig. 4.7. Output voltage versus operating switching frequency under different load conditions for converter operating in the *BCM*.

It can be seen in Fig. 4.7 that the operating switching frequency range for converter operating in the constant voltage mode during the *BCM* is,

$$f_{sw\_CVM} = 78\,kHz \sim 82\,kHz \tag{4.7}$$

And, Fig. 4.7 also shows that all the curves are monotonically decreasing, so a PID controller can be used to close the voltage loop for converter operating in the *BCM*.

To find the worst-case operating conditions, the control-to-output voltage, $G_{vf}(s)$, bode-plot is plotted for a load resistance of 60 Ω ~ 300 Ω, and operating switching frequency of 80 kHz in Fig. 4.8. It can be seen that all the plots are exactly alike. The only difference is, the resonant peak gets high as R_L increases. However, the DCR of magnetics' winding and the controller will attenuate this resonant peak considerably if the closed loop bandwidth is less than the resonant peak frequency.

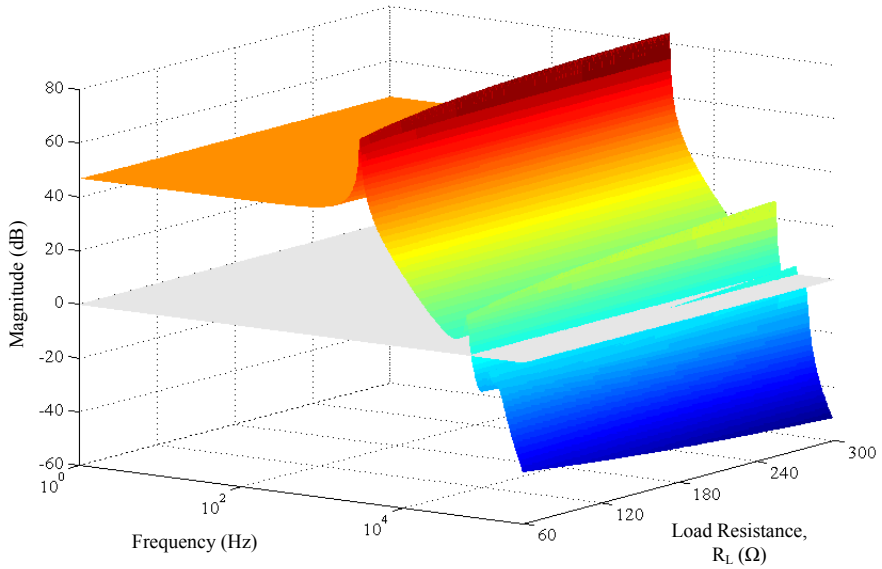

Fig. 4.8. Open-loop bode-plot for control-to-output voltage, $G_{vf}(s)$, for converter operating at switching frequency of 80 kHz under different load conditions.

So, in the constant voltage mode in the *BCM*, the worst-case operating conditions are when the output load resistance is 60 Ω, and the operating switching frequency is 80 kHz. This worst-case bode-plot is shown in Fig. 4.20.

4.5 Finding the Worst-Case Operating Conditions for the Voltage Loop Controller for Converter Operating in the RM

In the *RM*, the converter keeps the DC bus voltage constant for a wide range of battery voltages. In this mode, the converter primary-side rms current, i_2, can get very high for higher output power conditions. So, to limit this current, the output power is reduced at the lower battery voltages. Converter output power versus the battery voltage for converter operating in the *RM* is shown in Fig. 4.9.

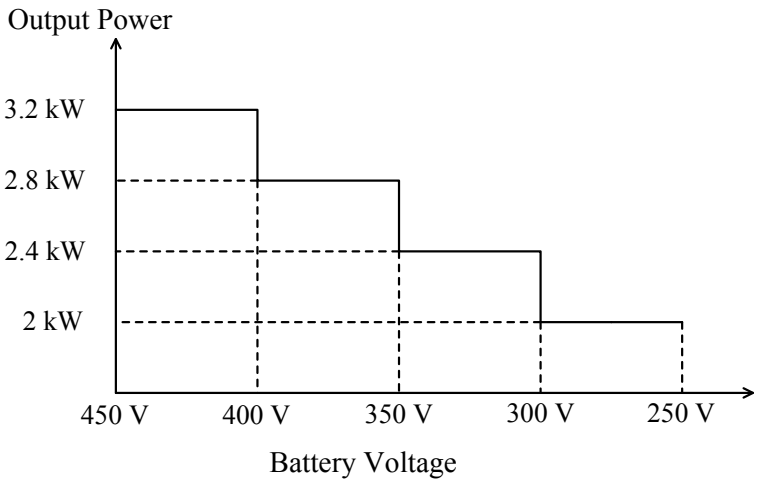

Fig. 4.9. Converter output power versus the battery voltage for converter operating in the *RM*.

For a dc bus voltage of 400 V, the equivalent load resistance in the *RM* is,

$$R_L = \frac{{V_{DC}}^2}{P_o} = \frac{400^2}{3200} \sim \frac{400^2}{2000} = 50\,\Omega \sim 80\,\Omega \tag{4.8}$$

To determine the operating frequency range in the *RM*, the steady-state voltage gain versus the operating switching frequency is plotted for different load resistances using equations (4.42) – (4.43). Fig. 4.10 shows these curves.

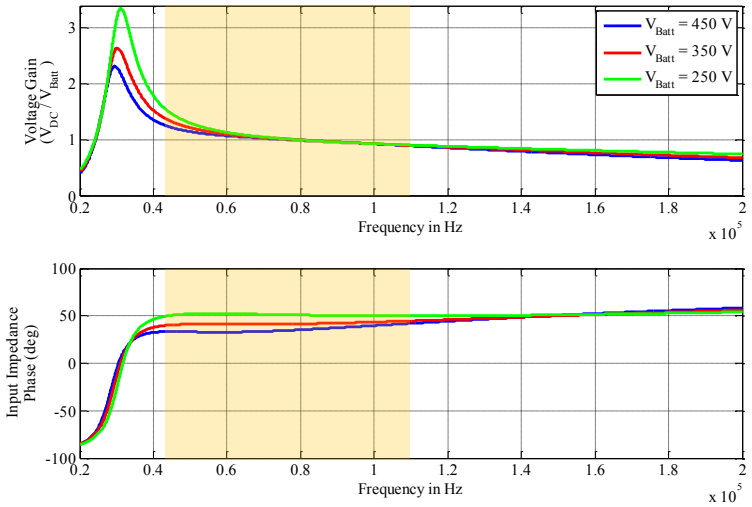

Fig. 4.10. Output voltage versus operating switching frequency under different load conditions for converter operating in the *BCM*.

It can be seen in Fig. 4.16 that the operating switching frequency range for converter operating in the *RM* is,

$$f_{sw\_CVM} = 45\ kHz \sim 110\ kHz \tag{4.9}$$

The voltage gain versus the operating switching frequency for the whole range of load resistance is plotted in Fig. 4.11. The operating surface is enclosed by the yellow polygon. It can be seen that the enclosed surface is monotonically decreasing, so a PID controller can used to close the voltage loop in the *RM*.

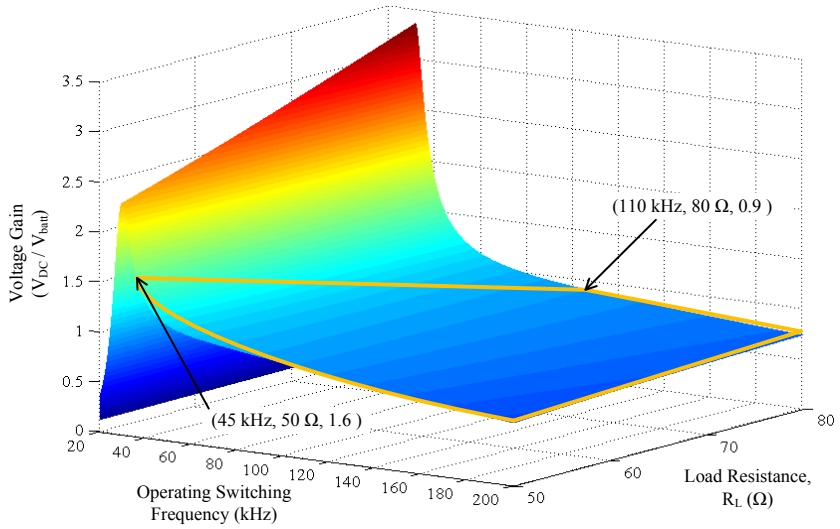

Fig. 4.11. Battery voltage versus operating switching frequency under different load conditions for converter operating in the *BCM*.

The next step is to find the worst-case conditions for the voltage loop controller design. Fig. 4.12 shows the open-loop control-to-output voltage, $G_{vf}(s)$, for a load resistance of 50 Ω. The operating switching frequency is varied from 45 kHz to 110 kHz. It can be seen that the open-loop bode-plot zero-crossing frequency does not change with the change in the converter switching frequency. However, for a converter operating switching frequency of 90 kHz, the open-loop bode-plot has high resonant peak making it the worst-case. So, for a fixed load resistance, the worst-case occurs at 90 kHz.

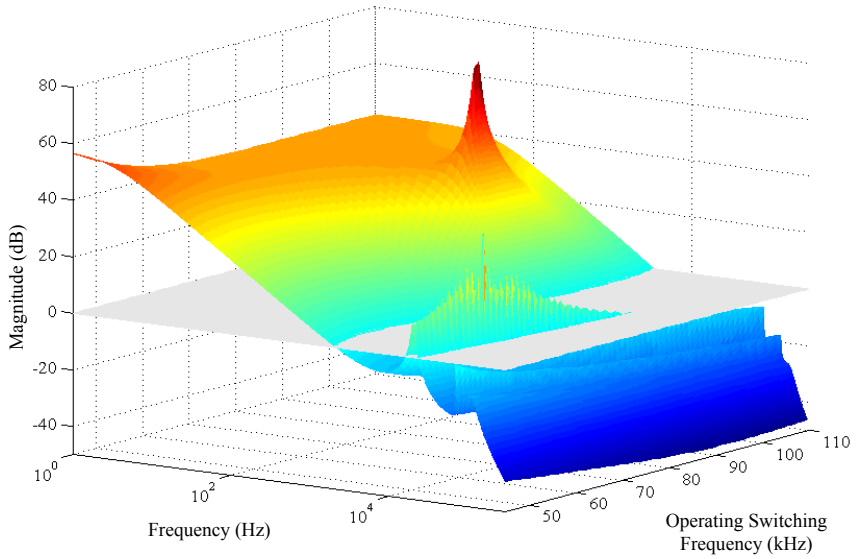

Fig. 4.12. Open-loop bode-plot for control-to-output voltage, $G_{vf}(s)$, under different operating switching frequencies for converter operating in the *RM*.

Fig. 4.13 shows the open-loop control-to-output voltage, $G_{vf}(s)$, for converter operating at a switching frequency of 90 kHz. The output load resistance is varied from 50 Ω to 500 Ω. It can be seen that the zero-crossing frequency of the open-loop bode remains almost the same, and all the plots are exactly alike. The only difference is, the resonant peak gets high as R_L increases. However, the DCR of magnetics' winding and the controller will attenuate this resonant peak considerably if the closed loop bandwidth is much less than the resonant peak frequency.

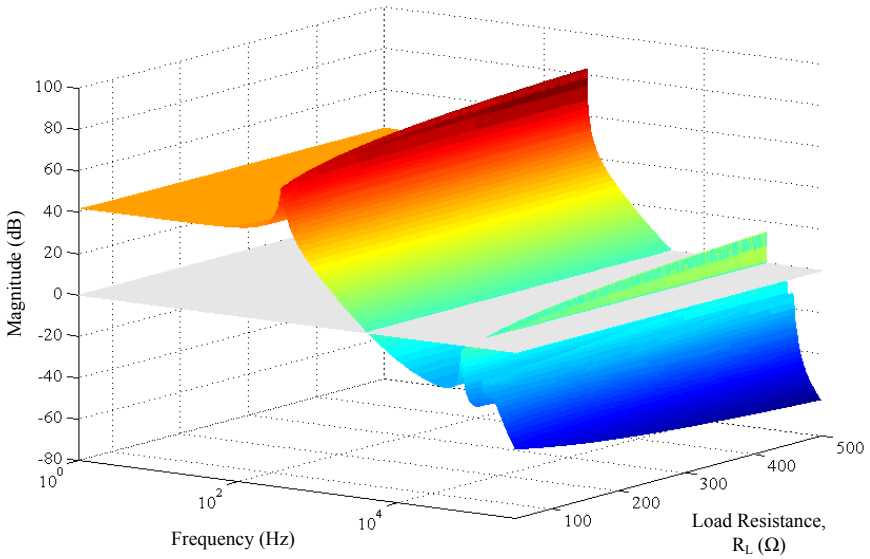

Fig. 4.13. Open-loop bode-plot for control-to-output voltage, $G_{vf}(s)$, for converter operating in the *RM* at switching frequency of 90 kHz under different load conditions.

So, in the constant voltage mode in the *RM*, the worst-case operating conditions are when the output load resistance is 50 Ω, and the operating switching frequency is 90 kHz. This worst-case bode-plot is shown in Fig. 4.23.

4.6 Operation of Converter Near the Series-Resonant Frequencies

The power stage efficiency of the converter is maximum at the primary-side series resonant frequency. The converter is designed to operate at this point under nominal operating conditions. However, in the last section, it was shown that the worst-case operating conditions for the current and voltage loop controller occur at this frequency because of the high quality-factor (Q) peak in the open-loop bode. To investigate this high Q peak in the bode-plots, the poles and the zeros in the converter transfer function must be observed when the converter is operating at a switching frequency close to the resonant frequencies. There are two series resonant frequencies in this converter. These are;

$$f_{ser1} = \frac{1}{2\pi\sqrt{L_1 C_1}} = 96.5\ kHz \tag{10}$$

$$f_{ser2} = \frac{1}{2\pi\sqrt{L_2 C_2}} = 79.58\ kHz \tag{11}$$

The small-signal model in equations (3.44) and (3.45) show that the resonant converter is a 9th order system. So there are nine poles in each transfer function. Most of the poles and zeros are at very high frequency. So, these high-frequency poles and zeros will be ignored, and only the low frequency dominant poles will be examined.

4.6.1 Operation of the Converter near Higher Series Resonant Frequency, f_{ser1}

Fig. 4.14 shows the dominant poles at different operating switching frequencies when the switching frequency is varied from 120 kHz to 80 kHz. At higher switching frequencies, the

dominant poles are on real axis, and there is no resonant peaking in the bode-plot. As the converter operating switching decreases, the two poles come close on the real axis until they reach the breakaway point. If the switching frequency is further reduced, the two poles break away from the real axis, and move towards the imaginary axis and the resonant peaking start to appear in the open-loop bode-plot. At the mid-point between the two resonant frequencies, the damping is minimum (and Q is maximum), and the magnitude of the resonant peak is maximum. A yellow cross in Fig. 4.14 represents this point.

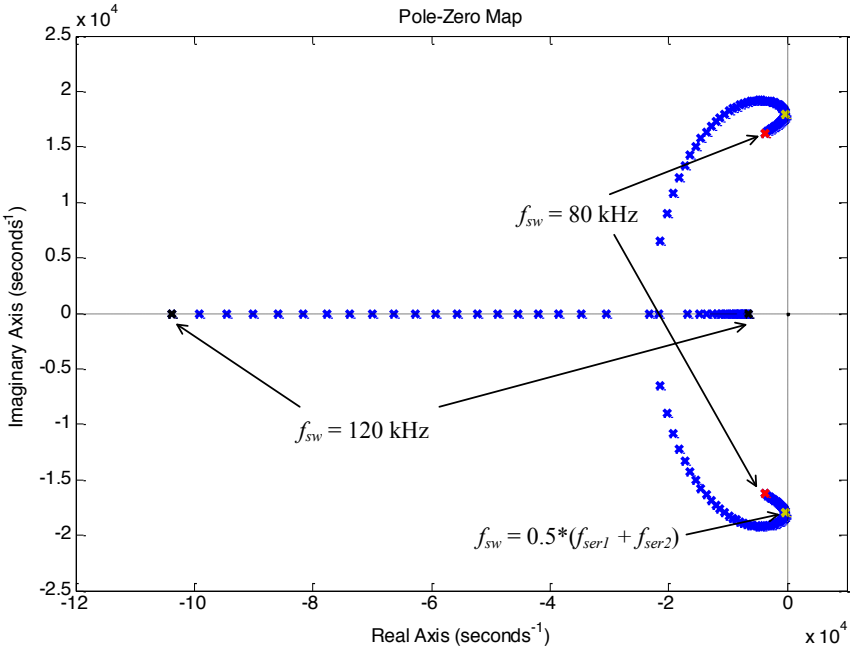

Fig. 4.14. Location of the low frequency poles when the operating switching frequency is varied from 120 kHz to 80 kHz.

4.6.2 Operation of the Converter near Lower Series Resonant Frequency, f_{ser2}

It can be seen in Fig. 4.15 that if the converter operating switching frequency is between the two resonant frequencies; the dominant poles are located close to the imaginary axis resulting in the resonant peaking in the open-loop bode-plot. However, if the converter switching frequency is reduced, the dominant poles start to move towards the real axis again until they reach the

break-in point. If the switching frequency is further reduced, the two dominant poles move away from each other on the real axis, and there is no resonant peaking in the open-loop bode-plots.

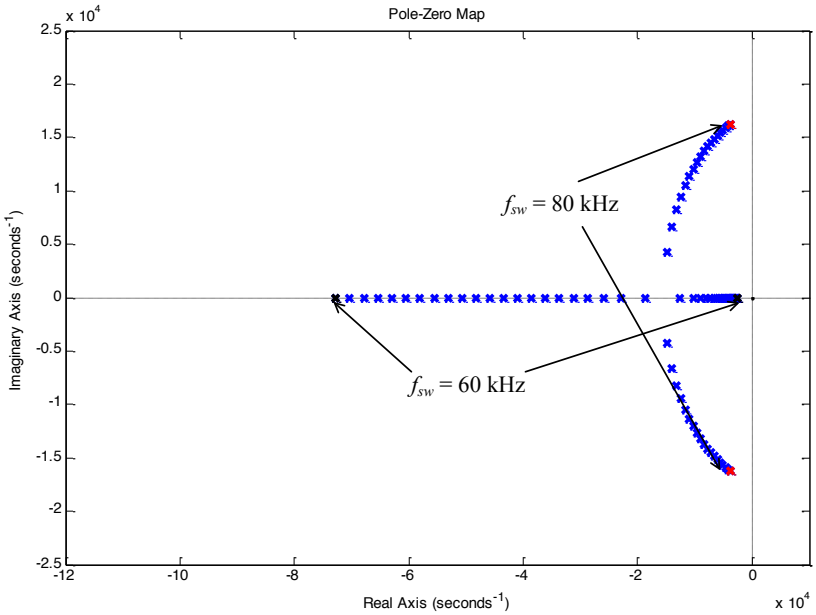

Fig. 4.15. Location of the low frequency poles when the operating switching frequency is varied from 80 kHz to 60 kHz.

From the above discussion, it can be concluded that there is no resonant peaking in the open-loop bode for the converter operating switching frequency higher than f_{ser1} and lower than f_{ser2}. However, if the converter operating switching frequency is between the two series resonant frequencies, then there will be peaking in the bode-plot because of lower damping and higher Q.

4.7 Controller Design and Experimental Results

In Section 4.2, the worst-case operating conditions were determined for the converter operating in both *BCM* and *RM*. In this section, controllers will be designed for these worst-case conditions. The block diagram for the closed loop system is shown in Fig. 4.16.

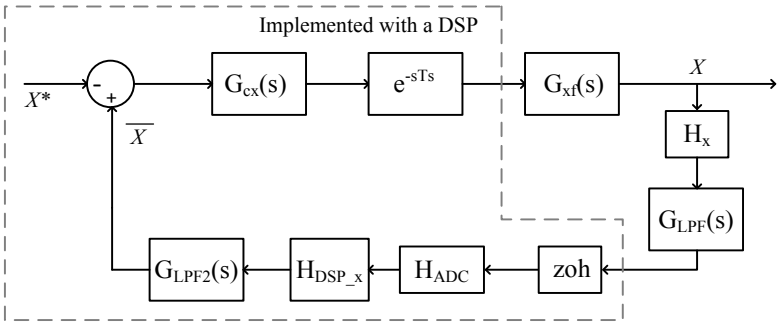

Fig. 4.16. Block diagram for the closed-loop system.

Where,

X = Output current or voltage to be regulated,

$\bar{X}$ = Averaged output current or voltage,

X^* = Output current or voltage reference,

H_x = Sensor gain,

$G_{LPF}(s)$ = Low-pass filter implemented with the hardware,

H_{ADC} = Analog-to-digital converter (ADC) gain,

H_{DSP_x} = Digital Signal Processor (DSP) gain,

$G_{LPF2}(s)$ = Low-pass filter implemented with the software in DSP,

$G_{cx}(s)$ = Designed controller,

e^{-sTs} = Single sampling period delay

The loop-gain of the closed-loop system is,

$$T_x(s) = G_{xf}(s) \cdot H_x \cdot G_{LPF}(s) \cdot H_{ADC} \cdot H_{DSP\_i} \cdot G_{LPF2}(s) \cdot G_{cx}(s) \cdot e^{-sTs} \quad (4.12)$$

The DSP gain is chosen such that the product of all gains is equal to unity, i-e

$$H_x \cdot H_{DSP\_x} \cdot H_{ADC} = 1 \tag{4.13}$$

So, the loop gain becomes,

$$T_x(s) = G_{xf}(s) \cdot G_{LPF}(s) \cdot G_{LPF2}(s) \cdot G_{cx}(s) \cdot e^{-sTs} \tag{4.14}$$

The low-pass filter implemented with hardware is a sallen-key 2nd order filter with a cut-off frequency of 10 kHz. The transfer function for it is,

$$G_{LPF}(s) = \frac{1}{1 + \frac{s}{2\pi\times10000} + (\frac{s}{2\pi\times10000})^2} \tag{4.15}$$

And, the low-pass filter implemented with a DSP is,

$$G_{LPF2}(s) = \frac{1}{1 + \frac{s}{2\pi\times1000}} \tag{4.16}$$

The controller will be implemented with a Texas Instruments TMS320F28335 DSP with a sampling frequency of 30 kHz, so a 33.33-µs delay is added in the loop.

$$e^{-sTs} = \frac{1 - \frac{T_s}{2}s + \frac{{T_s}^2}{12}s^2}{1 + \frac{T_s}{2}s + \frac{{T_s}^2}{12}s^2} \tag{4.17}$$

It can be seen in figures 4.3, 4.7 and 4.10 that the converter is designed to have a negative slope of the current and voltage curves. Because of this negative slope, the phase angle is -180° at the lower frequencies. So, instead of negative feedback there will be positive feedback in the closed loop as shown in Fig. 4.16.

For experiments, a programmable electronic load, BK Precision 8526 5000W, is used. In the BCM, the e-load is programmed as a battery load whose voltage is varied from 250V to 450V. In

the RM, the e-load is programmed as a current source whose current is varied from 0.1A to 8.5A to emulate the ac-dc stage.

4.7.1 Designing a Current Loop Controller for the Converter Operating in the BCM

The loop-gain of the converter operating in the constant current mode in the *BCM* is,

$$T_{i\_BCM}(s) = G_{if}(s) \cdot G_{LPF}(s) \cdot G_{LPF2}(s) \cdot G_{ci}(s) \cdot e^{-sTs} \tag{4.18}$$

The following controller is designed to have a bandwidth of 515 Hz, and a phase margin of 52.8° at the worst-case operating conditions.

$$G_{ci}(s) = \frac{10}{s} \tag{4.19}$$

The worst-case open-loop bode-plot and the closed-loop gain for the current loop with the designed controller are shown in Fig. 4.17.

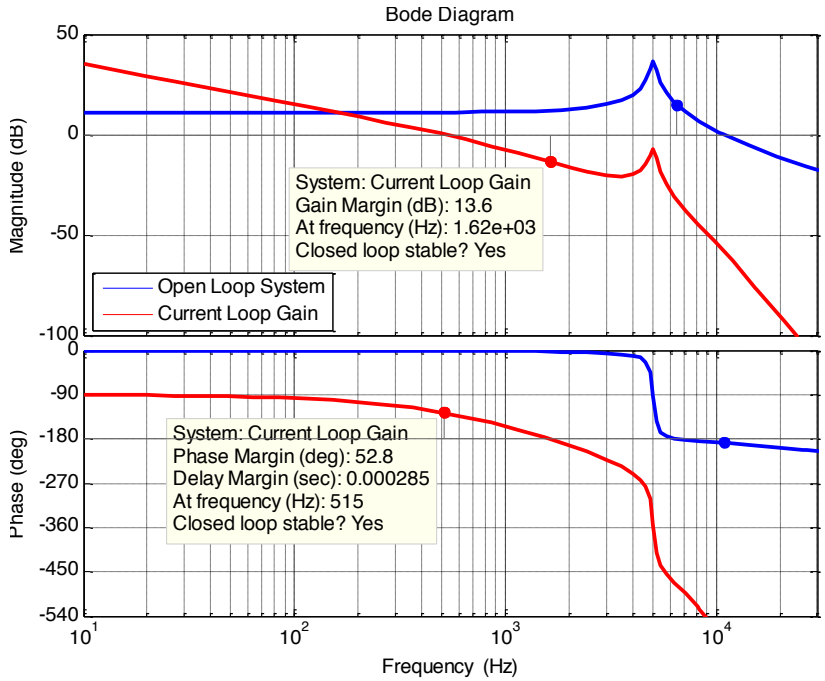

Fig. 4.17. The worst-case open-Loop bode-plot and loop gain for converter operating in the constant current mode in the *BCM*.

To check the stability of the closed-loop system, a step change was applied to the output battery voltage from 250 V to 325 V and back to 250 V. The system is found to be stable, with almost no overshoot or undershoot for both step increase and step decrease in the battery voltage. Fig. 4.18 and Fig. 4.19 show the system response to a step change in the battery voltage.

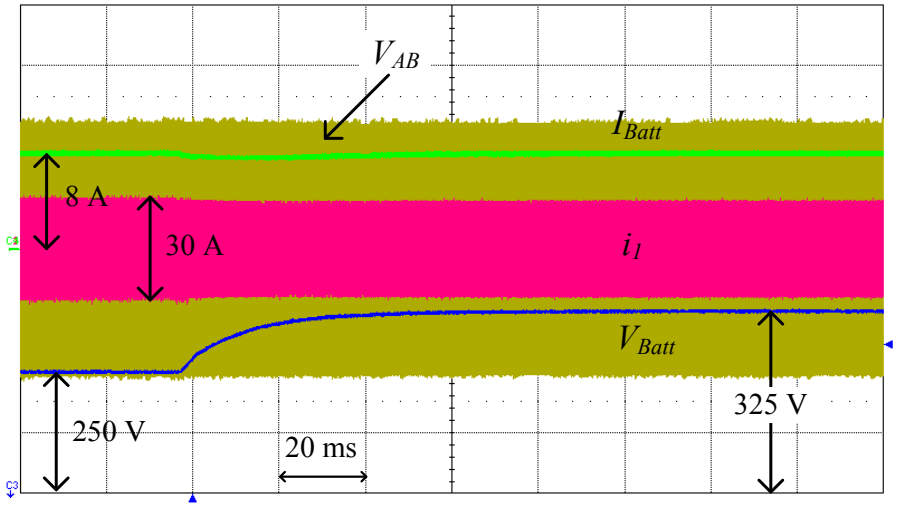

Fig. 4.18. Step change in the battery voltage from 250 V to 325 V for converter operating in the constant current mode in the *BCM*.

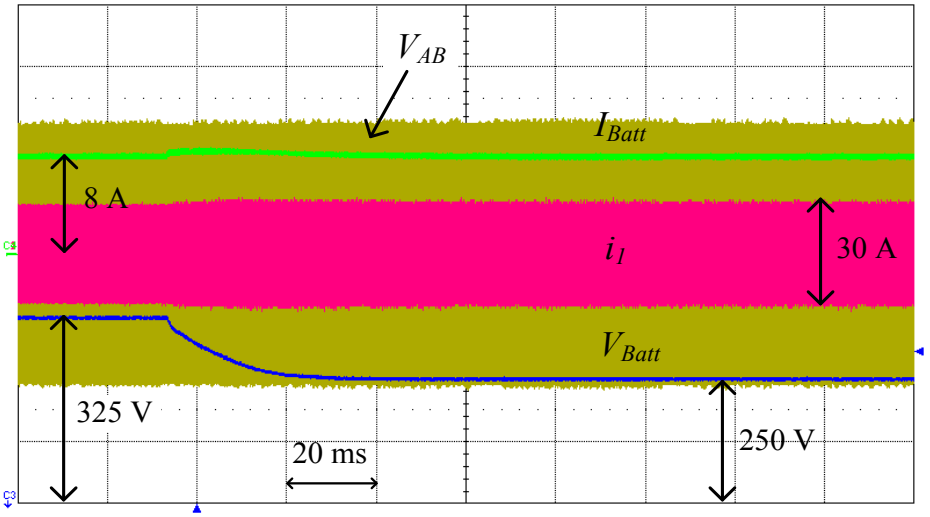

Fig. 4.19. Step change in the battery voltage from 325 V to 250 V for converter operating in the constant current mode in the *BCM*.

4.7.2 Designing a Voltage Loop Controller for Converter Operating in the BCM

The loop-gain of the converter operating in the constant voltage mode in the *BCM* is,

$$T_{v\_BCM}(s) = G_{vf}(s) \cdot G_{LPF}(s) \cdot G_{LPF2}(s) \cdot G_{cv}(s) \cdot e^{-sTs} \tag{4.20}$$

The following controller is designed to have a bandwidth of 103 Hz, and a phase margin of 82.2°.

$$G_{cv}(s) = \frac{0.3}{s} \tag{4.21}$$

The worst-case open-loop bode-plot and the closed-loop gain for the current loop with the designed controller are shown in Fig. 4.20.

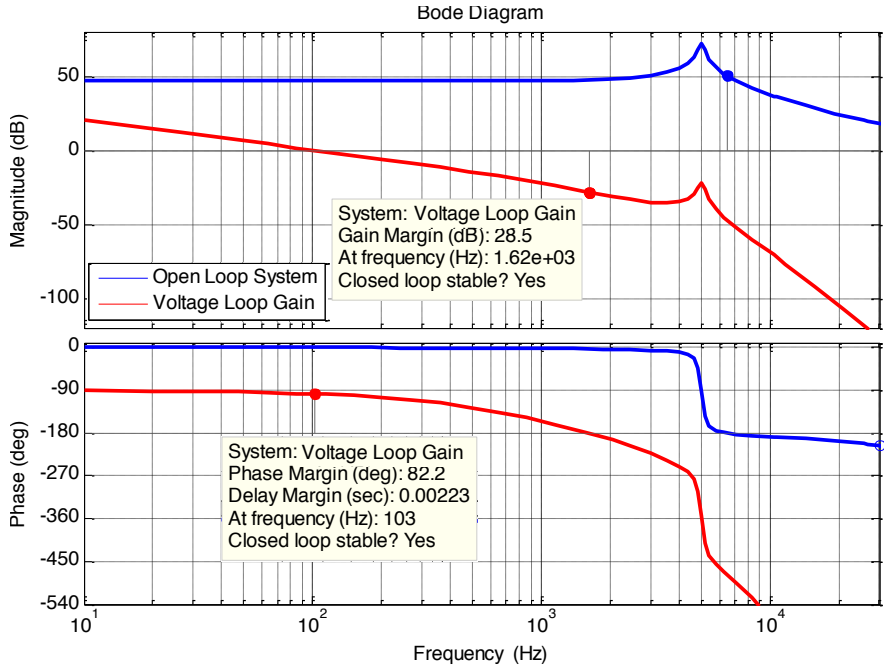

Fig. 4.20. The worst-case open-Loop bode-plot and loop gain for converter operating in the constant voltage mode in the *BCM*.

To check the stability of the closed-loop system, a step change was applied to the output voltage reference from 315 V to 420 V and back to 315 V for a resistive load of 57 Ω. The system is found to be stable, with no overshoot or undershoot for both step increase and step decrease in the reference voltage. Fig. 4.21 and Fig. 4.22 show the system response to a step change in the battery voltage.

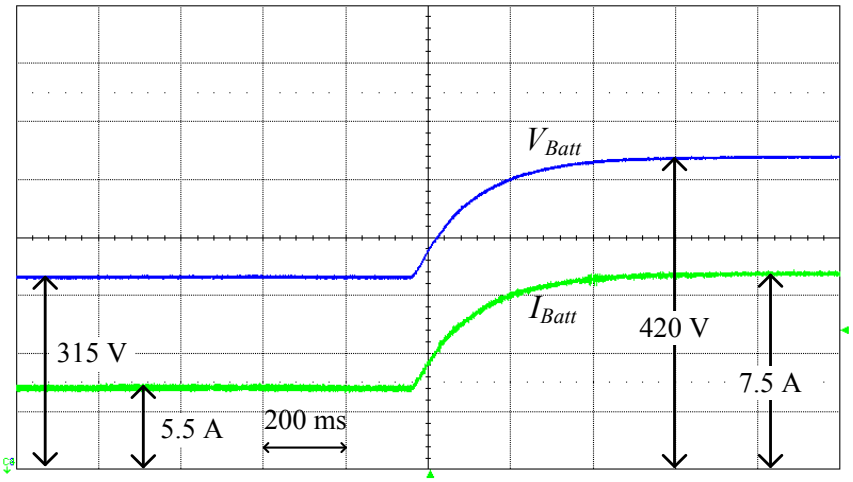

Fig. 4.21. Step change in the battery voltage from 315 V to 420 V for converter operating in the constant current mode at R_L = 57 Ω in the *BCM*.

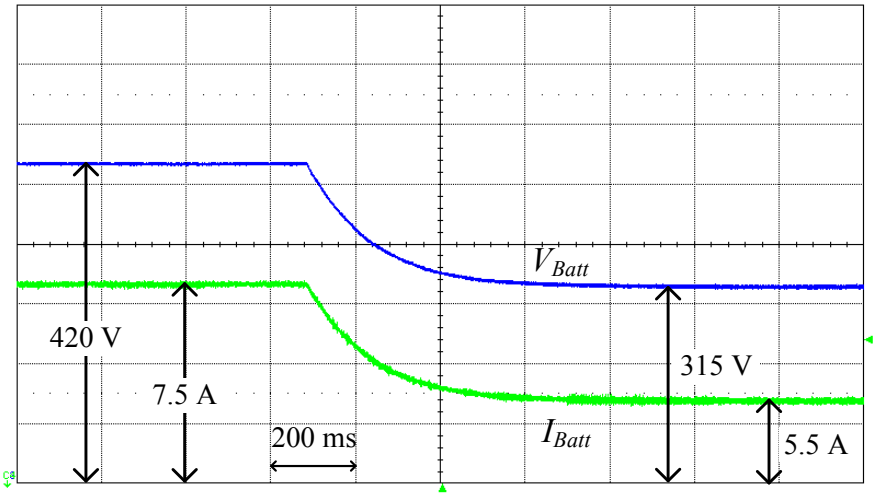

Fig. 4.22. Step change in the battery voltage from 420 V to 315 V for converter operating in the constant current mode at R_L = 57 Ω in the *BCM*.

4.7.3 Designing a Voltage Loop Controller for Converter Operating in the RM

The loop-gain of the converter operating in the constant voltage mode in the *RM* is,

$$T_{v\_RM}(s) = G_{vf}(s) \cdot G_{LPF}(s) \cdot G_{LPF2}(s) \cdot G_{cv}(s) \cdot e^{-sTs} \tag{4.22}$$

The following controller is designed to have a bandwidth of 516 Hz, and a phase margin of 52.7°.

$$G_{cv}(s) = \frac{2.5}{s} \tag{4.23}$$

The worst-case open-loop bode-plot and the closed-loop gain for the current loop with the designed controller are shown in Fig. 4.23.

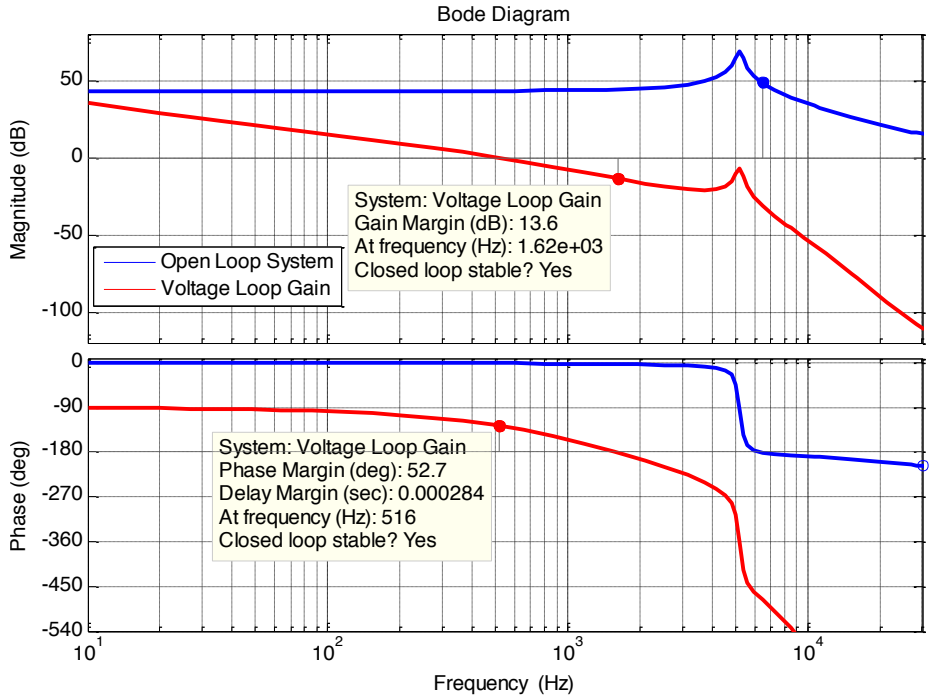

Fig. 4.23. The worst-case open-Loop bode-plot and loop gain for converter operating in the constant voltage mode in the *RM*.

To check the stability of the closed-loop system, a step change was applied to the output current reference from 4 A to 7 A and back to 4 A. The system is found to be stable, with almost no overshoot or undershoot for both step increase and step decrease in the reference voltage. Fig. 4.24 and Fig. 4.25 show the system response to a step change in the output current.

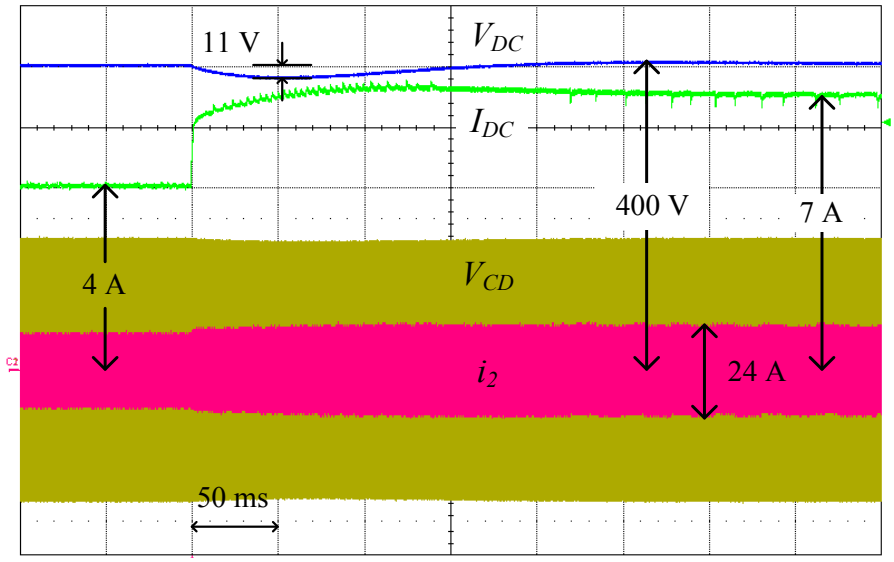

Fig. 4.24. Step change in the dc bus current from 4 A to 7 A for converter operating in the constant voltage mode in the *RM*.

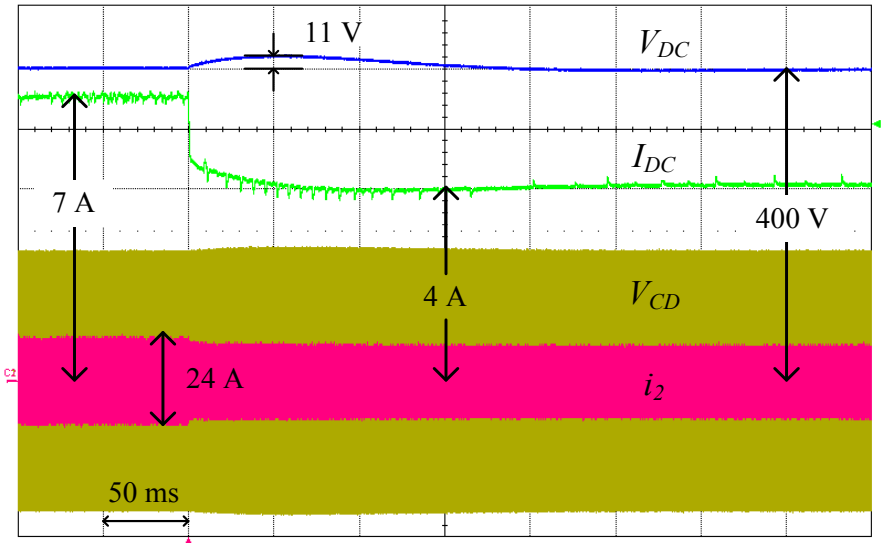

Fig. 4.25. Step change in the dc bus current from 7 A to 4 A for converter operating in the constant voltage mode in the *RM*.

4.8 Controller Design for a Series-Series Compensated IPT System

In this Section, the steady-state model and the small-signal model derived in Section 3.2 will be used to verify the design of the IPT system, and to close the voltage loop to regulate the output voltage for a resistive load.

The equivalent load resistance for the IPT system can be determined from the battery charging profile. Since the battery charging profile for the IPT system is the same as the

bidirectional resonant converter, the equivalent load resistance range is also the same.

$$R_{L\_IPT} = \frac{V_{Batt}}{I_{Batt}} = \frac{250\ V}{10\ A} \sim \frac{450\ V}{8\ A} = 25\ \Omega \sim 60\ \Omega \tag{4.24}$$

The steady-state model is used to plot the output voltage versus the switching frequency in Fig. 4.26 for three different load conditions.

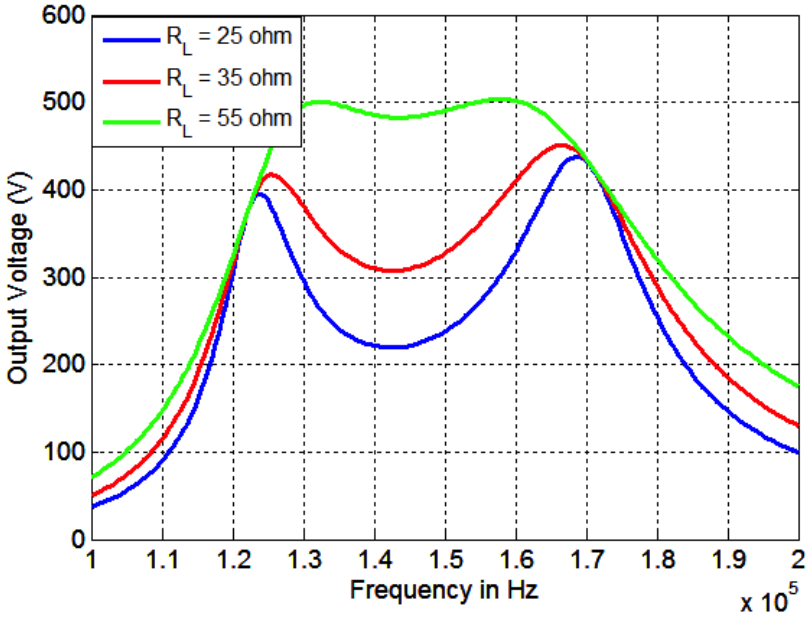

Fig. 4.26. IPT system output voltage versus operating switching frequency under different load conditions.

Steady-state voltage curves give a good amount of information about the design and the closed-loop operation of the converter. These curves can verify the design of the IPT system. These curves also give information about the operating frequency range of the converter. From the voltage curves in Fig. 4.26, the operating frequency range for this converter is from 165 to 180 kHz. The voltage curves are monotonically decreasing for all load conditions in the desired operating frequency range, which allows a simple PI or PID controller to be used to close the loop.

The small-signal model in equations (3.44) – (3.45) can be used to find different transfer functions in a converter. Fig. 4.27 shows the open loop control-to-output voltage transfer function under different load conditions for converter operating at 175 kHz.

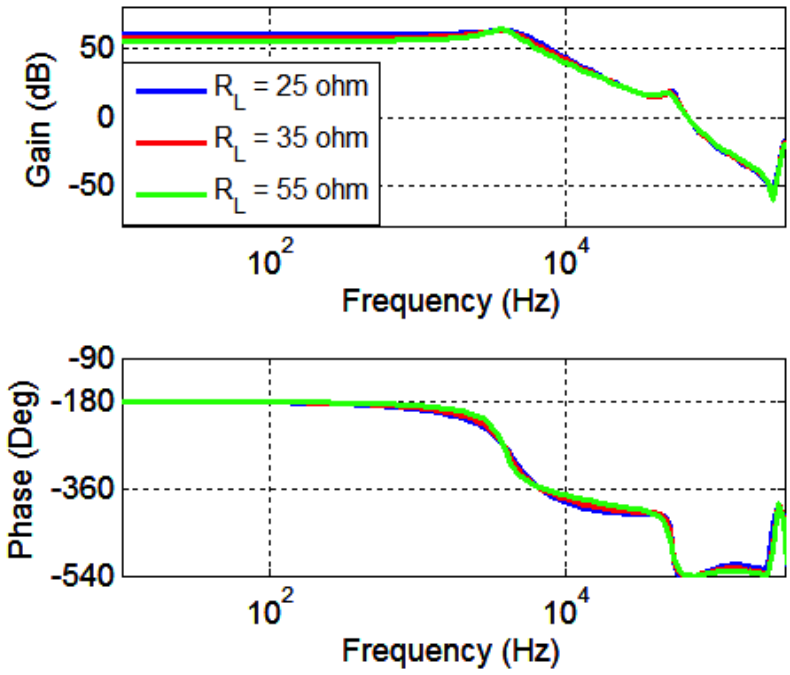

Fig. 4.27. Open Loop control-to-output voltage transfer for IPT system operating at 175 kHz under different load conditions.

Fig. 4.27 shows that the DC gain of the converter is almost the same for all load conditions. The phase angle is -180° at lower frequencies. This is because the slope of the voltage curves in Fig. 4.16 is negative in the desired range of frequencies. Because of this, instead of negative feedback there will be positive feedback in the closed loop as shown in Fig. 4.29.

The following controller was designed to have a bandwidth of 900 Hz and a phase margin of 60° for R_L = 25 Ω. The bandwidth is 520 Hz and the phase margin is 78° for R_L = 55 Ω.

$$G_{ci}(s) = \frac{5}{s} \tag{25}$$

The loop gains for the converter with the designed voltage loop controller under different load conditions are shown in Fig. 4.28. Because the control will be implemented with a digital signal processor (DSP), a 50-µs delay is added in the plot.

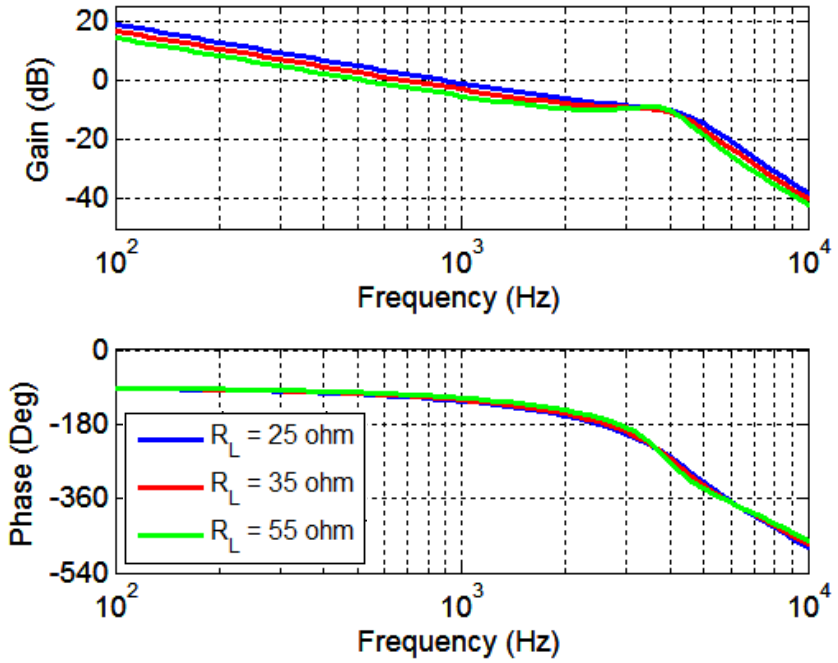

Fig. 4.28. Voltage loop gain of the closed loop system under different load conditions. A 50-µs delay is added to the loop.

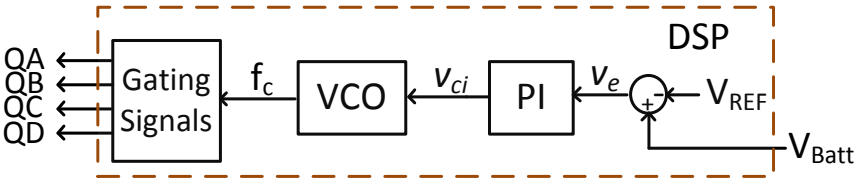

Fig. 4.29. Block diagram for output voltage loop.

The voltage loop controller was implemented with a Texas Instruments TMS320F28335 DSP. The circuit parameters are listed in Table 2.I. To check the stability of the closed-loop system a step change was applied to the voltage reference. The system is found to be stable, with a settling time of 6 ms for both step increase and step decrease in the voltage reference. Fig. 4.30 and Fig. 4.31 show the system response to a step change in the voltage reference.

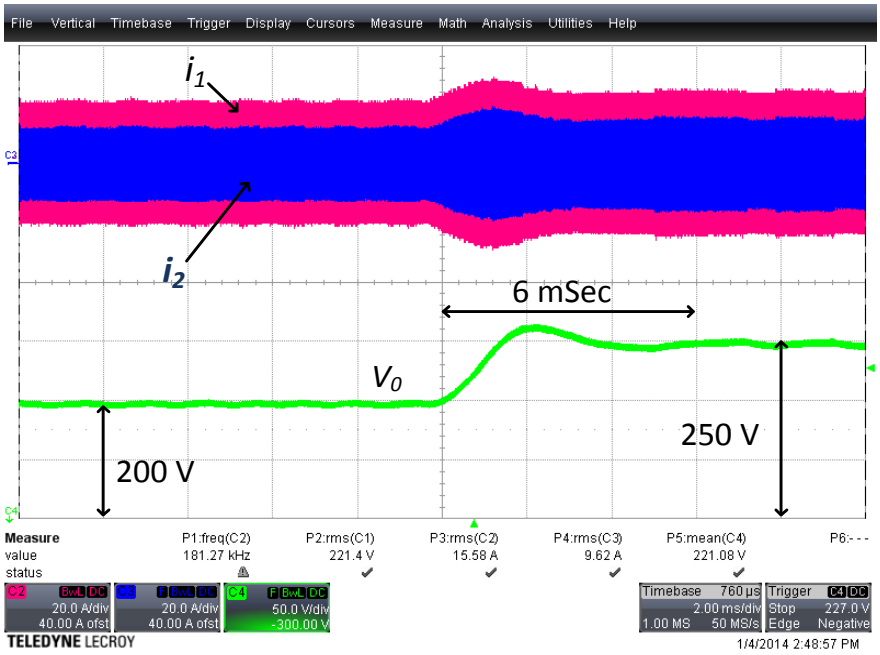

Fig. 4.30. Closed loop system response to step change in voltage reference voltage from 200 V to 250 V for R_L = 25Ω.

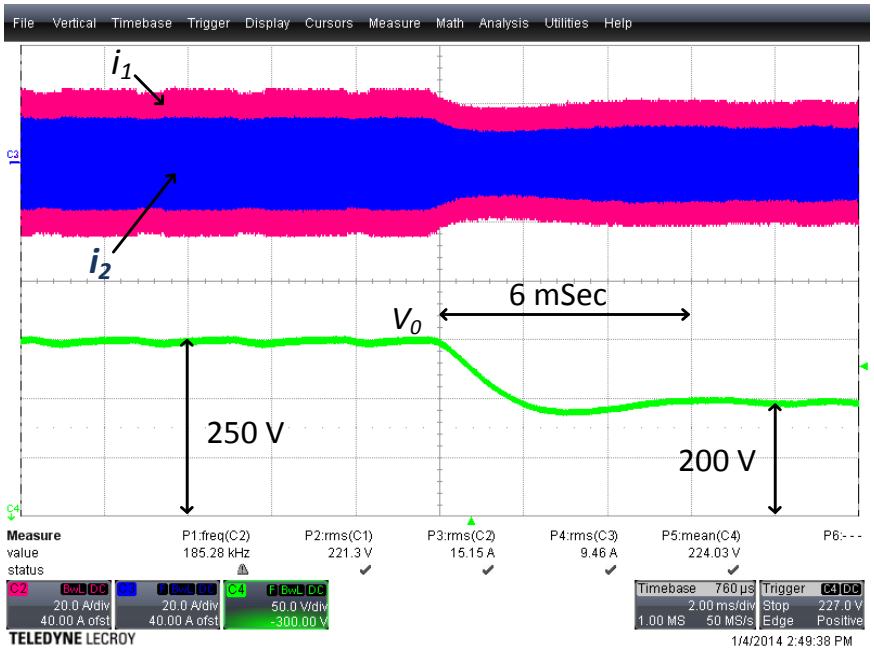

Fig. 4.31. Closed loop system response to step change in voltage reference voltage from 250 V to 200 V for R_L = 25Ω.

4.9 Conclusions

The *CLLLC*-type resonant converter is similar to an *LLC*-type resonant converter with an extra inductor and capacitor in the secondary side. This converter offers a number of advantages, including soft-switching in all switches, and very high power-stage efficiency. However, the dynamic characteristics of this converter change significantly as the battery charges or discharges. So, if the controller is not properly designed, the closed-loop system might become unstable at some operating points. In this paper, a controller design methodology is proposed that can guarantee a stable operation during the entire operating frequency range in both *BCM* and *RM*.

First, the worst-case operating conditions are found for the controller design. If the controller is designed for this worst-case, it will ensure stable operation at all other operating conditions. It was shown that the worst-case operating conditions occur at the operating switching frequency close to the primary-side series resonant frequency. However, it was found out that the open-loop bode-plot for any transfer functions in this converter has a high-Q resonant peaking when the operating switching frequency is close to the series resonant frequency, f_{res1}. To investigate it, the locations of the dominant poles were observed when the operating switching frequency was close to f_{res1}. It was shown that the dominant poles move towards the imaginary axis when the switching frequency approaches f_{res1}, resulting in the resonant peaking in the bode-plot. However, if the switching frequency is further decreased, these poles start to move towards the real axis again, and the peaking in the bode-plot also vanishes. So, the worst-case operating conditions occur when the dominant poles are close to the imaginary axis.

Then, the current and the voltage loop controllers were designed for the worst-case conditions. In the BCM, the e-load was used as a battery load. A step increase and step decrease

was applied to the battery voltage with the current loop closed. The system was found to be stable with almost no overshoot or undershoot. In the RM, the e-load was used as a current source to emulate the dc-ac stage. A step increase and step decrease in the load current was applied with the voltage loop closed. The closed-loop system was found to be stable with a very small overshoot and undershoot. These experiments validated the proposed controller design methodology.

Chapter 5 Conclusions and Future Work

5.1 Conclusions

EVs and PHEVs have battery packs that can be charged by the battery chargers. These battery chargers convert the ac power from the grid to the dc power, and charge the batteries inside these vehicles. In vehicle-to-grid (V2G) applications, these battery chargers are bidirectional, capable of transferring power back to the grid. The focus of this dissertation was to design and implement a resonant-type DC-DC converter that manages the energy flow between the dc bus and the high-voltage battery in EVs and PHEVs.

In this dissertation, first the design methodology for a bidirectional *CLLLC*-type resonant converter for battery charging application is presented in chapter 2. A *CLLC*-type resonant converter was derived from the *CLLLC*-type resonant converter. Then in chapter 3, the steady-state model, the large-signal model and the small-signal model for the bidirectional resonant converter were derived. And, the output voltage and output current loop controllers were

designed for the converter operating in the battery charging mode and in the regeneration mode. The main contributions of this dissertation are as follow,

- To propose the design methodology for a *CLLLC*-type bidirectional resonant converter for a battery charging applications. The charging process for a battery usually contains several stages, and the output voltage and the load power change significantly during the whole charging process. The design methodology proposed in Chapter 2 takes these processes into account. This design methodology will ensure that the voltage gain curves are always monotonically decreasing for all load and line conditions in both *BCM* and *RM* so that a linear controller can be designed to regulate the output current and voltage. The proposed design methodology is verified experimentally.
- The derivation of the *CLLC*-type resonant equivalent network from a *CLLLC*-type resonant network. Usually, in a resonant converter, the heaviest and bulky component is the inductor and/or a transformer. In this paper, a *CLLC*-type resonant network is derived from the *CLLLC*-type network. This resonant network has one less inductor. So, the weight and size of the converter can be reduced. The advantage is more significant for very high-power applications.
- The derivation of averaged large-signal model, the steady-state model and the small-signal model for the bidirectional resonant converter. The steady-state model gives a good amount of information about the power-stage design and the closed-loop operation of the converter. This model can provide the operating switching frequency range of the designed converter. The small-signal model can be used to derive any transfer function in the converter.

- To find the worst-case operating conditions for the output current and output voltage loop controller design. If the controller is designed for this worst-case, it will ensure stable operation at all other operating conditions. The output current and the output voltage loop controllers converter operating in both battery charging mode and regeneration mode were designed for the worst-case conditions.

To validate the design procedure, a 3.5 kW converter was designed, and built in lab following the guidelines in the proposed methodology as a design example. Experimental results verified both the designs. It was found that the *CLLC*-type network was more compact and lighter in weight as compared to the *CLLLC*-type network. The total volume and weight of the magnetics in *CLLLC*-type network were 415 cm^3 and 1300 g respectively, whereas in the *CLLC*-type network, the volume and the weight of the magnetics are 315 cm^3 and 1050 g respectively.

The power-stage efficiency of the bidirectional dc-dc resonant converter was high in both the battery charging mode (BCM) and the regeneration mode (RM). Under different load conditions, the power-stage efficiency with a *CLLC* configuration is generally higher than the efficiency with a *CLLLC* configuration in the *BCM*. On the other hand, the efficiency with a *CLLLC* configuration is generally higher than the efficiency with *CLLC* configuration in the *RM*. For a *CLLLC* configuration, the peak efficiency was 97.7% under *BCM* and 98.1% under *RM*. For a *CLLC* configuration, the peak efficiency was 97.7% under *BCM* and 97.9% under *RM*.

Bidirectional dc-dc converters are the integral part of the battery chargers in EVs with V2G capability. The above results showed that *CLLLC*-type and *CLLC*-type are two dc-dc resonant converters that can be used in the battery chargers with V2G capability.

5.2 Future Work

The research work in this dissertation demonstrates promising results. However, there are other areas where further investigations will be required to increase the overall performance of the bidirectional resonant converter. The following topics are recommended for future work.

a) To reduce the conduction losses in the switches, SiC mosfets can be used. This, however, will increase the overall cost of the converter.
b) Implement synchronous rectification in the secondary-side to reduce the conduction losses in the rectifying diodes.
c) Integrate the resonant inductor and transformer in a single magnetic structure to further reduce the size of the converter.
d) To design the state-space controller like LQR and LQG controller for the output current and output voltage loops for improved transient performance.

Publications

[P.1] Zahid, Zaka Ullah.; Dalala, Z.; Chen, R.; Chen, B.; Lai, J., "Design of Bidirectional DC-DC Resonant Converter for Vehicle-to-Grid (V2G) Applications," in *Transportation Electrification, IEEE Transactions on* , vol.PP, no.99, pp.1-1. doi: 10.1109/TTE.2015.2476035.

[P.2] Zaka Ullah Zahid, Z. M. Dalala, Z. Cong, C. Rui, W. E. Faraci, J. S. J. Lai, et al., "Modeling and Control of Series-Series Compensated Inductive Power Transfer System," Emerging and Selected Topics in Power Electronics, IEEE Journal of, vol. 3, pp. 111-123, 2015.

[P.3] Z. Cong, L. Jih-Sheng, C. Rui, W. E. Faraci, Zaka Ullah Zahid, G. Bin, et al., "High-Efficiency Contactless Power Transfer System for Electric Vehicle Battery Charging Application," Emerging and Selected Topics in Power Electronics, IEEE Journal of, vol. 3, pp. 65-74, 2015.

[P.4] Zaka Ullah Zahid, Z. Dalala, and L. Jih-Sheng, "Small-signal modeling of series-series compensated induction power transfer system," in Applied Power Electronics Conference and Exposition (APEC), 2014 Twenty-Ninth Annual IEEE, 2014, pp. 2847-2853.

[P.5] Zaka Ullah Zahid, Z. Dalala, and L. Jih-Sheng, "Design and control of bidirectional resonant converter for Vehicle-to-Grid (V2G) applications," in Industrial Electronics Society, IECON 2014 - 40th Annual Conference of the IEEE, 2014, pp. 1370-1376.

[P.6] Zaka Ullah Zahid, Z. Cong, C. Rui, W. E. Faraci, L. Jih-Sheng, M. Senesky, et al., "Design and control of a single-stage large air-gapped transformer isolated battery charger for wide-range output voltage for EV applications," in Energy Conversion Congress and Exposition (ECCE), 2013 IEEE, 2013, pp. 5481-5487.

[P.7] Zaka Ullah Zahid, J. S. J. Lai, X. K. Huang, S. Madiwale, and J. Hou, "Damping impact on dynamic analysis of LLC resonant converter," in Applied Power Electronics Conference and Exposition (APEC), 2014 Twenty-Ninth Annual IEEE, 2014, pp. 2834-2841.

[P.8] C. Rui, Z. Cong, Zaka Ullah Zahid, E. Faraci, Y. Wengsong, L. Jih-Sheng, et al., "Analysis and parameters optimization of a contactless IPT system for EV charger," in Applied Power Electronics Conference and Exposition (APEC), 2014 Twenty-Ninth Annual IEEE, 2014, pp. 1654-1661.

[P.9] Z. M. Dalala, Zaka Ullah Zahid, Y. Wensong, C. Younghoon, and L. Jih-Sheng, "Design and Analysis of an MPPT Technique for Small-Scale Wind Energy Conversion Systems," Energy Conversion, IEEE Transactions on, vol. 28, pp. 756-767, 2013.

[P.10] Z. M. Dalala, Zaka Ullah Zahid, and L. Jih-Sheng, "New Overall Control Strategy for Small-Scale WECS in MPPT and Stall Regions With Mode Transfer Control," Energy Conversion, IEEE Transactions on, vol. 28, pp. 1082-1092, 2013.

[P.11] Z. Dalala, Zaka Ullah Zahid, and L. Jih-Sheng, "New overall control strategy for wind energy conversion systems in MPPT and stall regions," in Energy Conversion Congress and Exposition (ECCE), 2013 IEEE, 2013, pp. 2412-2419.

[P.12] C. Baifeng, G. Bin, Z. Lanhua, Zaka Ullah Zahid, J. S. J. Lai, L. Zhiling, et al., "A High-Efficiency MOSFET Transformerless Inverter for Nonisolated Microinverter Applications," Power Electronics, IEEE Transactions on, vol. 30, pp. 3610-3622, 2015.

References

[1] I. E. Outlook. Available: http://www.eia.gov/forecasts/aeo/pdf/0383(2012).pdf

[2] International Energy Outlook. Available: http://www.eia.gov/forecasts/aeo/pdf/0383(2015).pdf

[3] A. Emadi, L. Young Joo, and K. Rajashekara, "Power Electronics and Motor Drives in Electric, Hybrid Electric, and Plug-In Hybrid Electric Vehicles," *Industrial Electronics, IEEE Transactions on,* vol. 55, pp. 2237-2245, 2008.

[4] N. USA. (Aug 17). Available: http://www.nissanusa.com/electric-cars/leaf/

[5] T. Motors. (Aug 17). Available: http://www.teslamotors.com/models

[6] Chevrolet. (Aug 17). Available: http://www.chevrolet.com/volt-electric-car.html

[7] B. USA. (Aug 17). Available: http://www.bmwusa.com/bmw/BMWi

[8] V. Cars. (Aug 17). Available: http://esd.volvocars.com/site/owners-information/MY12/C30_PEV/SUPPL_1146/C30_Electric_MY12_EN_tp14621.pdf

[9] M.-B. USA. (Aug 17). Available: http://www.mbusa.com/mercedes/vehicles/class/class-B/bodystyle-EDV

[10] T. Instruments. (Aug 17). Available: http://www.ti.com/lit/ml/szza058c/szza058c.pdf

[11] W. Kramer, S. Chakraborty, B. Kroposki, A. Hoke, G. Martin, and T. Markel, "Grid Interconnection and Performance Testing Procedures for Vehicle-To-Grid (V2G) Power Electronics," National Renewable Energy Laboratory (NREL), Golden, CO.2012.

[12] L. Chiao-Ting, A. Changsun, P. Huei, and S. Jing, "Synergistic control of plug-in vehicle charging and wind power scheduling," *Power Systems, IEEE Transactions on,* vol. 28, pp. 1113-1121, 2013.

[13] C. Kuei-Hsiang and H. Chun-Hao, "Bidirectional DC-DC soft-switching converter for stand-alone photovoltaic power generation systems," *Power Electronics, IET,* vol. 7, pp. 1557-1565, 2014.

[14] R. Redl, "Batteries for Beginners," *Proc. in APEC,* Feb 5-9 2012.

[15] M. C. Kisacikoglu, B. Ozpineci, and L. M. Tolbert, "Reactive power operation analysis of a single-phase EV/PHEV bidirectional battery charger," in *Power Electronics and ECCE Asia (ICPE & ECCE), 2011 IEEE 8th International Conference on*, 2011, pp. 585-592.

[16] G. Glanzer, T. Sivaraman, J. I. Buffalo, M. Kohl, and H. Berger, "Cost-efficient integration of electric vehicles with the power grid by means of smart charging strategies and integrated on-board chargers," in *Environment and Electrical Engineering (EEEIC), 2011 10th International Conference on*, 2011, pp. 1-4.

[17] J. Francfort. (2010, Aug 17). *Electric Vehicle Charging Levels and Requirements Overview*. Available: http://avt.inel.gov/pdf/CleanCitiesWedinarCharging12-15-10.pdf

[18] A. INGRAM. (22010, Aug 17). *Charging your electric car at home: What you need to know*. Available: http://venturebeat.com/2010/08/13/charging-your-electric-car-at-home-what-you-need-to-know/

[19] P. G. Electric. (Aug 05, 2010, Aug 17). *Portland General Electric Opens North America's First Public-Use Quick-Charge Station*. Available: http://investors.portlandgeneral.com/releasedetail.cfm?ReleaseID=496964

[20] C. C. Chan and K. T. Chau, "An overview of power electronics in electric vehicles," *Industrial Electronics, IEEE Transactions on,* vol. 44, pp. 3-13, 1997.

[21] J. G. Hayes. (May 1998, Aug 17). *Battery Charging Systems for Electric Vehicles*.

[22] I. A. Khan, "Battery chargers for electric and hybrid vehicles," in *Power Electronics in Transportation, 1994. [Proceedings]*, 1994, pp. 103-112.

[23] C. Gyu-Yeong, K. Jong-Soo, L. Byoung-kuk, W. Chung-Yuen, and L. Tea-Won, "A Bi-directional battery charger for electric vehicles using photovoltaic PCS systems," in *Vehicle Power and Propulsion Conference (VPPC), 2010 IEEE*, 2010, pp. 1-6.

[24] J. Ke, R. Xinbo, Y. Mengxiong, and X. Min, "A Hybrid Fuel Cell Power System," *Industrial Electronics, IEEE Transactions on,* vol. 56, pp. 1212-1222, 2009.

[25] C. C. Lin, L.-S. Yang, and G. W. Wu, "Study of a non-isolated bidirectional DC-DC converter," *Power Electronics, IET,* vol. 6, pp. 30-37, 2013.

[26] M. C. Kisacikoglu, M. Kesler, and L. M. Tolbert, "Single-Phase On-Board Bidirectional PEV Charger for V2G Reactive Power Operation," *Smart Grid, IEEE Transactions on,* vol. 6, pp. 767-775, 2015.

[27] B. L. Narasimharaju, S. P. Dubey, and S. P. Singh, "Design and analysis of coupled inductor bidirectional DC-DC convertor for high-voltage diversity applications," *Power Electronics, IET,* vol. 5, pp. 998-1007, 2012.

[28] P. Junsung and C. Sewan, "Design and Control of a Bidirectional Resonant DC–DC Converter for Automotive Engine/Battery Hybrid Power Generators," *Power Electronics, IEEE Transactions on,* vol. 29, pp. 3748-3757, 2014.

[29] F. Martin Ibanez, J. Martin Echeverria, J. Vadillo, and L. Fontan, "A Step-Up Bidirectional Series Resonant DC/DC Converter Using a Continuous Current Mode," *Power Electronics, IEEE Transactions on,* vol. 30, pp. 1393-1402, 2015.

[30] D. Yu, S. Lukic, B. Jacobson, and A. Huang, "Review of high power isolated bi-directional DC-DC converters for PHEV/EV DC charging infrastructure," in *Energy Conversion Congress and Exposition (ECCE), 2011 IEEE*, 2011, pp. 553-560.

[31] J. Tianyang, Z. Junming, W. Xinke, S. Kuang, and W. Yousheng, "A Bidirectional LLC Resonant Converter With Automatic Forward and Backward Mode Transition," *Power Electronics, IEEE Transactions on,* vol. 30, pp. 757-770, 2015.

[32] L. Corradini, D. Seltzer, D. Bloomquist, R. Zane, D. Maksimovic, and B. Jacobson, "Zero Voltage Switching Technique for Bidirectional DC/DC Converters," *Power Electronics, IEEE Transactions on,* vol. 29, pp. 1585-1594, 2014.

[33] Y. Wensong, Q. Hao, and L. Jih-Sheng, "Design of high-efficiency bidirectional DC-DC converter and high-precision efficiency measurement," in *Industrial Electronics, 2008. IECON 2008. 34th Annual Conference of IEEE*, 2008, pp. 685-690.

[34] Z. Junhong, L. Jih-Sheng, K. Rae-young, and Y. Wensong, "High-Power Density Design of a Soft-Switching High-Power Bidirectional dc–dc Converter," *Power Electronics, IEEE Transactions on,* vol. 22, pp. 1145-1153, 2007.

[35] Y. Miura, M. Kaga, Y. Horita, and T. Ise, "Bidirectional isolated dual full-bridge dc-dc converter with active clamp for EDLC," in *Energy Conversion Congress and Exposition (ECCE), 2010 IEEE*, 2010, pp. 1136-1143.

[36] B. R. Lin, J. J. Chen, Y. E. Lee, and H. K. Chiang, "Analysis and implementation of a bidirectional ZVS dc-dc converter with active clamp," in *Industrial Electronics and Applications, 2008. ICIEA 2008. 3rd IEEE Conference on*, 2008, pp. 382-387.

[37] M. Hallworth, A. B. Potter, and S. A. Shirsavar, "Analytical calculation of resonant inductance for zero voltage switching in phase-shifted full-bridge converters," *IET Power Electronics,* vol. 6, pp. 523-534, 2013.

[38] J. E. Baggio, H. L. Hey, H. A. Grundling, H. Pinheiro, and J. R. Pinheiro, "Isolated interleaved-phase-shift-PWM DC-DC ZVS converter," *Industry Applications, IEEE Transactions on,* vol. 39, pp. 1795-1802, 2003.

[39] V. Vlatkovic, J. A. Sabate, R. B. Ridley, F. C. Lee, and B. H. Cho, "Small-signal analysis of the phase-shifted PWM converter," *Power Electronics, IEEE Transactions on,* vol. 7, pp. 128-135, 1992.

[40] K. Eun-Soo and K. Yoon-Ho, "A ZVZCS PWM FB DC/DC converter using a modified energy-recovery snubber," *Industrial Electronics, IEEE Transactions on,* vol. 49, pp. 1120-1127, 2002.

[41] Z. U. Zahid, Z. M. Dalala, C. Zheng, R. Chen, W. E. Faraci, J. S. Lai*, et al.*, "Modeling and Control of Series-Series Compensated Inductive Power Transfer (IPT) System," *Emerging and Selected Topics in Power Electronics, IEEE Journal of,* vol. PP, pp. 1-1, 2014.

[42] Z. U. Zahid, Z. M. Dalala, Z. Cong, C. Rui, W. E. Faraci, J. S. J. Lai*, et al.*, "Modeling and Control of Series–Series Compensated Inductive Power Transfer System," *Emerging and Selected Topics in Power Electronics, IEEE Journal of,* vol. 3, pp. 111-123, 2015.

[43] Z. U. Zahid, Z. Dalala, and L. Jih-Sheng, "Small-signal modeling of series-series compensated induction power transfer system," in *Applied Power Electronics Conference and Exposition (APEC), 2014 Twenty-Ninth Annual IEEE*, 2014, pp. 2847-2853.

[44] Z. U. Zahid, Z. Cong, C. Rui, W. E. Faraci, L. Jih-Sheng, M. Senesky*, et al.*, "Design and control of a single-stage large air-gapped transformer isolated battery charger for wide-range output voltage for EV applications," in *Energy Conversion Congress and Exposition (ECCE), 2013 IEEE*, 2013, pp. 5481-5487.

[45] Z. Cong, C. Rui, E. Faraci, Z. U. Zahid, M. Senesky, D. Anderson*, et al.*, "High efficiency contactless power transfer system for electric vehicle battery charging," in *Energy Conversion Congress and Exposition (ECCE), 2013 IEEE*, 2013, pp. 3243-3249.

[46] Z. U. Zahid, Z. Dalala, and L. Jih-Sheng, "Design and control of bidirectional resonant converter for Vehicle-to-Grid (V2G) applications," in *Industrial Electronics Society, IECON 2014 - 40th Annual Conference of the IEEE*, 2014, pp. 1370-1376.

[47] C. Wei, S. Wang, H. Xiaoyuan, L. Zhengyu, and Y. Shaoshi, "Fully soft-switched bidirectional resonant dc-dc converter with a new CLLC tank," in *Applied Power Electronics Conference and Exposition (APEC), 2010 Twenty-Fifth Annual IEEE*, 2010, pp. 1238-1242.

[48] C. Wei, R. Ping, and L. Zhengyu, "Snubberless Bidirectional DC–DC Converter With New CLLC Resonant Tank Featuring Minimized Switching Loss," *Industrial Electronics, IEEE Transactions on,* vol. 57, pp. 3075-3086, 2010.

[49] J. H. Jung, H. S. Kim, M. H. Ryu, and J. W. Baek, "Design Methodology of Bidirectional CLLC Resonant Converter for High-Frequency Isolation of DC Distribution Systems," *Power Electronics, IEEE Transactions on,* vol. 28, pp. 1741-1755, 2013.

[50] B. Yang, "Topology investigation for front end DC/DC power conversion for distributed power system," Virginia Polytechnic Institute and State University, 2003.

[51] S. Cuk and R. D. Middlebrook, "A general unified approach to modelling switching DC-tO-DC converters in discontinuous conduction mode," in *Power Electronics Specialists Conference, 1977 IEEE*, 1977, pp. 36-57.

[52] V. Vorperian, "Simplified analysis of PWM converters using model of PWM switch. Continuous conduction mode," *Aerospace and Electronic Systems, IEEE Transactions on,* vol. 26, pp. 490-496, 1990.

[53] V. Vorperian, "Simplified analysis of PWM converters using model of PWM switch. II. Discontinuous conduction mode," *Aerospace and Electronic Systems, IEEE Transactions on,* vol. 26, pp. 497-505, 1990.

[54] A. F. Witulski, A. F. Hernandez, and R. W. Erickson, "Small signal equivalent circuit modeling of resonant converters," *Power Electronics, IEEE Transactions on,* vol. 6, pp. 11-27, 1991.

[55] G. J. J. van Zyl, "A novel frequency-domain small-signal analysis of resonant power converters," *Circuits and Systems I: Regular Papers, IEEE Transactions on,* vol. 51, pp. 1379-1384, 2004.

[56] V. Vorperian, "Approximate small-signal analysis of the series and the parallel resonant converters," *Power Electronics, IEEE Transactions on,* vol. 4, pp. 15-24, 1989.

[57] R. J. King and T. A. Stuart, "Small-Signal Model for the Series Resonant Converter," *Aerospace and Electronic Systems, IEEE Transactions on,* vol. AES-21, pp. 301-319, 1985.

[58] Y. Yan, R. Zane, R. Erickson, and J. Glaser, "Direct modeling of envelope dynamics in resonant inverters," in *Power Electronics Specialist Conference, 2003. PESC '03. 2003 IEEE 34th Annual*, 2003, pp. 1313-1318 vol.3.

[59] S. R. Sanders, J. M. Noworolski, X. Z. Liu, and G. C. Verghese, "Generalized averaging method for power conversion circuits," *Power Electronics, IEEE Transactions on,* vol. 6, pp. 251-259, 1991.

[60] A. P. Hu, "Modeling a contactless power supply using GSSA method," in *Industrial Technology, 2009. ICIT 2009. IEEE International Conference on*, 2009, pp. 1-6.

[61] E. X. Yang, F. C. Lee, and M. M. Jovanovic, "Small-signal modeling of LCC resonant converter," in *Power Electronics Specialists Conference, 1992. PESC '92 Record., 23rd Annual IEEE*, 1992, pp. 941-948 vol.2.

[62] E. X. Yang, F. C. Lee, and M. M. Jovanovic, "Small-signal modeling of series and parallel resonant converters," in *Applied Power Electronics Conference and Exposition, 1992. APEC '92. Conference Proceedings 1992., Seventh Annual*, 1992, pp. 785-792.

[63] B. Yang, F. C. Lee, A. J. Zhang, and H. Guisong, "LLC resonant converter for front end DC/DC conversion," in *Applied Power Electronics Conference and Exposition, 2002. APEC 2002. Seventeenth Annual IEEE*, 2002, pp. 1108-1112 vol.2.

[64] B. Yang, F. C. Lee, and M. Jovanovic, "Small-signal analysis for LLC resonant converter," in *CPES Seminar*, 2003, pp. 144-149.